STUDY OF MIXED BOUNDARY SECTORAL MICROSTRIP ANTENNAS

A Thesis Submitted
In Partial Fulfilment of the Requirements
for the Degree of

MASTER OF TECHNOLOGY

By

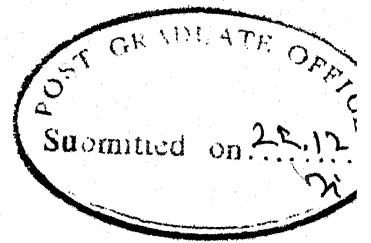## ESWARAPPA

to the

DEPARTMENT OF ELECTRICAL ENGINEERING

INDIAN INSTITUTE OF TECHNOLOGY, KANPUR

DECEMBER, 1982

EE-1982-M-ESW-STU

CERTIFICATE

This is to certify that the work reported in this
thesis entitled 'STUDY OF MIXED BOUNDARY SECTORAL MICROSTRIP
ANTENNAS' by Eswarappa has been carried out under my
supervision and has not been submitted elsewhere for a
degree.

(R. Raghuram)
Assistant Professor
Department of Electrical Engineering
Indian Institute of Technology
Kanpur 208016,India.

ACKNOWLEDGEMENTS

ABSTRACT

Semicircular microstrip antennas with straight edge shorted, circular periphery shorted; open boundary semi-circular and 120°-sectoral microstrip antennas are studied. Green's function approach with segmentation method is used for analyzing these antennas. Green's functions for mixed boundary sectoral segments are developed using the method of expansion in series of eigenfunctions. The Green's functions for 30°-60° mixed boundary right-angled triangles, shorted boundary equilateral triangle are developed using the method of images. A comparative study of mixed boundary semicircular antennas and 120°-sectoral open boundary antenna with circular and semicircular open boundary antennas is done. Study of mutual coupling between two semicircular antennas (with circular peripheries shorted) and two open boundary semicircular antennas is also done.

LIST OF CONTENTS

Chapter One

INTRODUCTION

This chapter is a brief review of the 2-dimensional
(2-d) components used in microwave integrated circuits
(MICs) and 2-d microstrip antennas. An outline of the rest
of the chapters is also given.

1.1 TWO-DIMENSIONAL COMPONENTS

Two-dimensional components have been proposed for
use in microwave integrated circuits [1] - [3]. These
components have dimensions comparable to or greater than
the wavelength in two directions but have the third
dimension much smaller than the wavelength. The three
types of possible configurations of 2-d components are :
(i) triplate or stripline-type as shown in Fig. 1.1(a);
(ii) open or microstrip-type as shown in Fig. 1.1(b) and
1.1(c); (iii) waveguide or cavity-type as shown in
Fig. 1.1(d).

1.1.1 Methods of analysis of 2-d components

The method of analysis of a 2-d component depends upon
its geometry (i.e., shape of the central conducting patch
in a triplate structure or the upper conductor patch in
microstrip type circuit).

(a) Stripline type

(b) Microstrip type

(c) Plan view of (a) and (b)

2-D CIRCUIT ELEMENT

(d) Waveguide type

2-D CIRCUIT ELEMENT

CONNECTING WAVEGUIDE
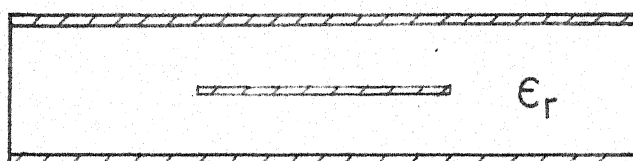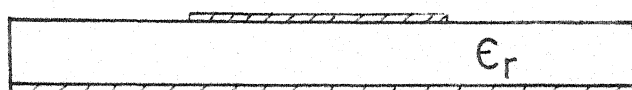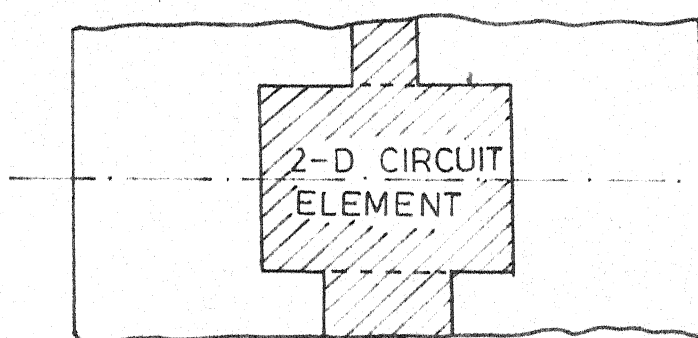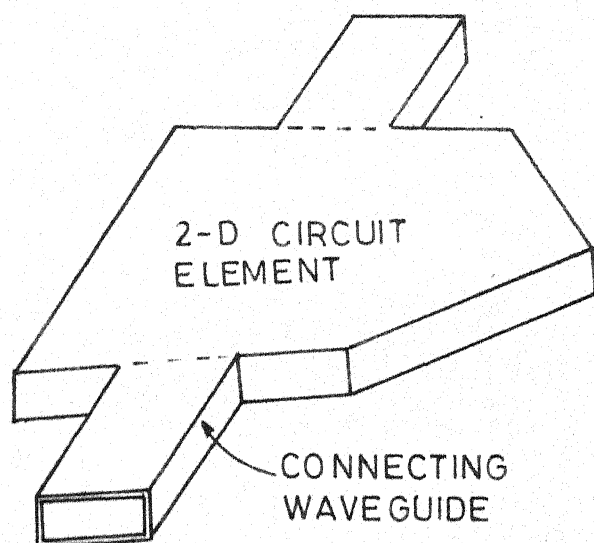
Fig. 1·1 Three types of 2-d microwave circuits

When the 2-d component is of simple shape, impedance Green's functions [1] are used for its analysis. These Green's functions have been known for only rectangular [2], circular [4], sectoral [6], and some triangular [5] (isosceles, equilateral and 30°-60° right angled) shapes, with open boundaries (or magnetic walls). Using Green's functions, the impedance matrix of a component can be obtained for specified port-locations.

When the geometrical shape of a 2-d circuit can be considered to be made up of simpler shapes for which the Green's functions are available, the segmentation method [2],[3] can be used for evaluating the characteristics of the overall circuit from those of various components of simple shapes.

For the analysis of arbitrary shaped 2-d components, numerical methods such as finite element approach [7] and contour integral approach   [1] are used.

1.1.2 Applications

The 2-d components have found several applications in microwave integrated circuits, waveguide circuits, ferrite components and microstrip antennas. Some of the areas where the 2-d approach has found applications are listed below.

i) Resonators : 2-d components can be used for the design of high-Q resonators used at microwave frequencies. The

rectangular, circular, and triangular elements have been used for resonators. The triangular shaped 2-d components have been used for realizing band-pass and band-stop filters [8],[9]. And the triangular resonators have been used in the design of three-port circulators [9].

ii) Analysis of Discontinuities : The 2-d approach can be employed to analyze accurately the discontinuities in strip-lines, microstrip lines [10] and waveguides.

iii) Design of Non-reciprocal Elements : 2-d circuits, fabricated on ferrite substrates, may also be analyzed by the 2-d approach using the extension of analysis techniques for circuits on dielectric substrates. This method has been used for obtaining optimum shape of a wideband circulator.

iv) Microstrip Antennas : 2-d approach can be employed to find the voltage distribution along the periphery of the planar circuit. The far fields can be calculated from the voltage distribution. The details are given in Chapter Three.

1.2 MICROSTRIP ANTENNAS

The microstrip devices have widely been used as micro-wave circuit elements, such as resonators, filters, trans-mission lines, etc. The successful operation of the high-Q microstrip resonators seems to suggest that basically they are poor radiators. Despite this weakness, microstrip antennas have received much attention because of their many unique and attractive properties – low in profile, light in

weight, compact and conformable in structure , and easier
to fabricate and to be integrated with solid state devices.
The main shortcoming is its narrow bandwidth (because the
Q-factor is high). The shortcomings may be compensated
for with more efficient solid-state sources, amplifiers, and
adaptive impedance-matching networks.

The simplest configuration of microstrip antenna is
shown in Fig. 1.2. It consists of a conducting patch on the
top of the dielectric substrate, backed by a ground plane
on the other side. However, a large variety of microstrip
antennas is available. These are patch antennas, travelling
wave antennas, slot antennas, and dipole antennas [11], as
shown in Fig. 1.3. Investigations in this thesis are con-
fined to microstrip patch antennas which could be called as
2-d microstrip antennas also. The shape of the patch can
be of any shape, but conventional shapes are generally used
to simplify analysis and performance prediction. Generally,
the dielectric constant of the substrate is kept low
($\varepsilon_r \leqslant 10$), so as to enhance the fringing fields which
account for radiation.

1.2.1 Special features of microstrip antennas

Microstrip antennas have several advantages, compared
to conventional microwave antennas. They are used in the
frequency range of 100 MHz to 50 GHz.
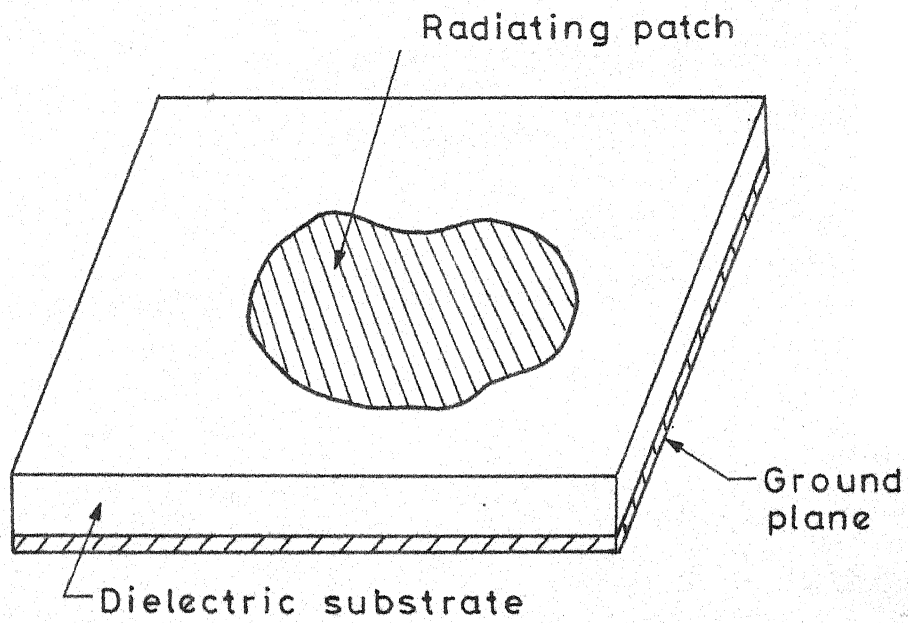
Fig.1·2 Microstrip antenna configuration

(a) Patch antenna

FEED

(b) Travelling wave antenna

Slot

Stripline on backside of the substrate
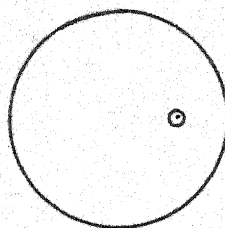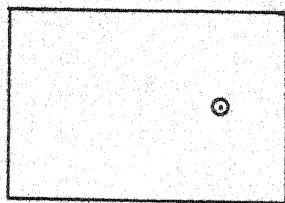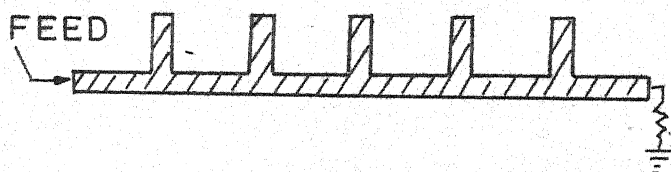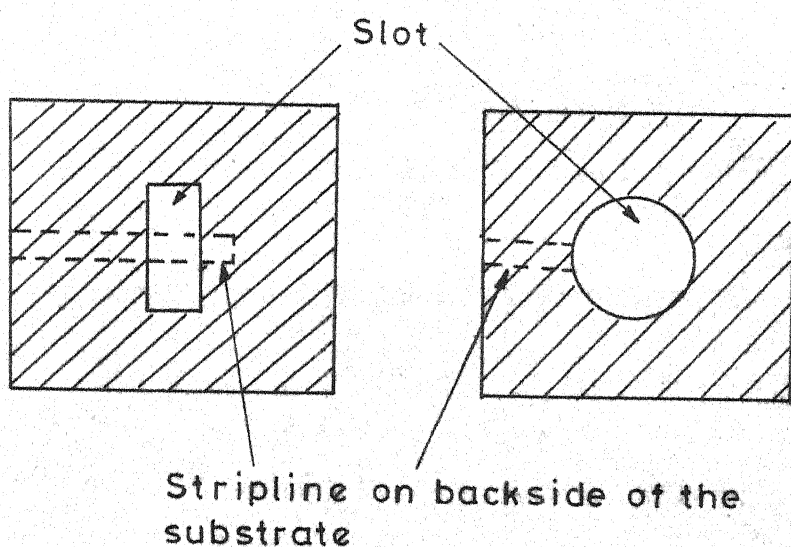
(c) Slot antenna
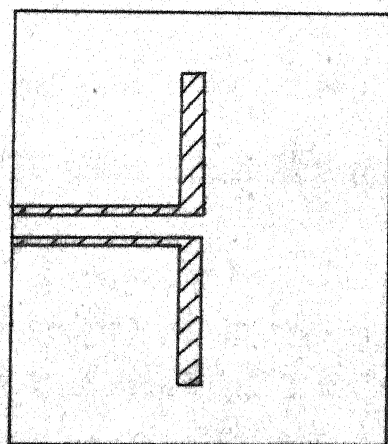
(d) Dipole antenna

Fig.13 Various types of microstrip antennas

Advantages of microstrip antennas

The main advantages of microstrip antennas are :

i) light weight, low volume, low profile planar configurations which can be made conformal,

ii) the fabrication cost is less,

iii) they can be made paper thin, such that they do not perturb the aerodynamics of host aerospace vehicles,

iv) the antennas can be easily mounted on missiles, rockets and satellites without major alterations,

v) linear, circular polarizations are possible with simple changes in feed position,

vi) no cavity backing is required,

vii) solid state devices such as oscillators, amplifiers, switches, modulators, phase shifters, etc. can be added directly to the antenna substrate board,

viii) feed lines and matching networks are fabricated simultaneously with the antenna structure.

Disadvantages of microstrip antennas

The disadvantages of microstrip antennas are :

i) narrow bandwidth. Typical microstrip antenna bandwidths are of the order of 1 to 5 percent,

ii) the poor isolation between the feed and the radiating element, which degrades antenna performance,

iii)   the surface waves may be excited along the antenna

surface, resulting in radiation in undesired

directions,

iv)   they cannot operate at high power levels of waveguides

and coaxial lines.

Applications of microstrip antennas

Some notable applications for which microstrip

antennas have been developed are :

i)   Satellite communications

ii)   Doppler radars

iii)   Altimeters

iv)   Command and control

v)   Missile telemetry

vi)   Phased array radars

vii)   Feed elements for various applications

viii) Satellite navigation receivers

ix)   Biomedical radiators.

1.2.2 Methods for analyzing microstrip antennas

Various methods for analyzing microstrip antennas have

been reported in the literature. These are : i) Equivalent

transmission-line method, ii) Modal-expansion method, iii)

Green's function method, iv) Finite element method, v) Method

of moments. A brief review of these methods is given below.

i)   Equivalent transmission-line method

Only rectangular antennas can be analyzed using this

method. In this method, the antenna excited in the dominant mode is modelled as a transmission line, with no transverse field variation [11],[12]. The edges along which the field is uniform are considered as radiating slots, and others as non-radiating slots. The effective length of the non-radiating edge after taking into account the fringing fields by extending the physical boundary outwards is taken equal to half a wavelength. The input impedance and resonant frequency are evaluated from the effective dimensions of the antenna.

ii) Modal-Expansion method

Here, the radiating patch is modelled as a resonator with magnetic walls [11],[13],[14]. The field in the cavity is expanded in series of corresponding eigen functions. The effect of radiation and other losses is represented in terms of either increased effective loss-tangent [13] or by employing impedance boundary conditions. This method can be used for analyzing the shapes for which the eigen functions are available.

iii) Green's function method

When a patch antenna is of simple shape, the impedance Green's functions [15],[16] are used for analysis. In this approach, the antenna structure is modelled as a multiport network. The ports of this network are terminated by resistances to account for the radiation from the antenna.

By knowing the Green's function of the planar element, the antenna can be analysed. Details of the Green's function method are described in Chapter Three.

iv) Finite element method

This method [12],[17] is used for the analysis of arbitrary shaped planar antennas. In this method, the interior and exterior regions of the microstrip antenna are mathematically decoupled through the use of an equivalent aperture admittance as boundary conditions. The interior electric field satisfies the inhomogeneous wave equation alongwith the impedance boundary conditions on the perimeter walls, and these equations are solved as variational problem. For analysis, the antenna geometry is divided into several segments. Certain basis functions are used for each segment to solve the variational problem and the boundary conditions are imposed locally along the edges of the segment. The solution is obtained numerically.

v) Method of moments

This method [18,[19] is also used for the analysis of arbitrary shaped planar antennas. Here, the electric surface currents flowing over the microstrip patch and ground planes, and the magnetic surface currents flowing over the magnetic walls are obtained from the Richmond's reaction method. Using boundary conditions for the surface currents, the reaction integral equation is solved by the method of moments. By

selecting suitable expansion functions for electric surface currents, and electric test sources for magnetic currents, the reaction integral equation reduces to simultaneous linear equations. The coefficients of these equations give the elements of the impedance matrix.

1.3 PRESENT INVESTIGATIONS

Green's functions have hitherto been developed for only rectangular, circular, sectoral (both circular and annular) and some triangular segments with open boundaries (i.e. the segments surrounded by magnetic walls. The tangential component of $\underline{H}$ is zero along a magnetic wall). In circuits, which are symmetrical about an axis, even and odd mode symmetry can be used for complete analysis of the circuit. The even and odd mode circuits are obtained by placing a magnetic wall and electric wall respectively along the axis of symmetry. For example, the even and odd mode circuits of an equilateral triangular segment with shorted boundary (i.e. the segment surrounded by electric walls, along which the tangential component of $\underline{E}$ is zero) are 30°-60° right-angled triangular segment with the side opposite to 60° as magnetic wall and other two sides as electric walls and 30°-60° right-angled triangular segment with shorted boundary respectively. Thus, there is a need to obtain the Green's functions for mixed boundary planar segments. Moreover, for the analysis of mixed

boundary planar antennas (which can be used in arrays to reduce mutual coupling) using Green's function approach, the Green's functions for these mixed boundary planar segments are needed. And a high-Q resonator is expected from a shorted boundary planar segment : as the radiation loss is negligible. A chapterwise description of the present work is given below.

In Chapter Two, Green's functions are developed for mixed boundary $30^{\circ}-60^{\circ}$ right-angled triangular and shorted boundary equilateral triangular segments using the method of images. The Green's functions are also developed for mixed boundary sectoral segments by expansion in series of eigen functions.

In Chapter Three, semicircular microstrip antennas with straight edge shorted, circular periphery shorted; open boundary semicircular and 120°-sectoral microstrip antennas are investigated. Mutual coupling between two semicircular antennas with circular peripheries shorted and mutual coupling between two open boundary semicircular microstrip antennas are also studied.

In the Fourth chapter, the significant results reported in this thesis are discussed and also suggestions for further work in this area are given.

CHAPTER   TWO

ANALYSIS OF TWO-DIMENSIONAL COMPONENTS AND GREEN'S
FUNCTIONS FOR MIXED BOUNDARY PLANAR
SEGMENTS

This chapter presents a review of the 2-d components
used in microwave integrated circuits and their analysis
using Green's functions. Green's functions for 30°-60°
right-angled triangular and circular sectoral segments with
all the possible boundaries are developed.

2.1 BASIC CONCEPTS

Consider a stripline type 2-d planar circuit shown in
Fig. 2.1. Basic equations for obtaining the circuit para-
meters for the equivalent multiport network are discussed
in this section.

In the circuit of Fig. 2.1, an arbitrary shaped thin
conductor is sandwiched midway between two ground condu-
ctors spaced 2d apart. The circuit is excited symmetrically
with respect to the upper and lower ground conductors.
There are several ports along the periphery. Widths of
these ports are denoted by W_i, W_j, ... The rest of the
periphery is open circuited. The co-ordinate axes are
shown in the Fig. 2.1. The z-axis is perpendicular to the
central conducting patch. The thickness of the planar
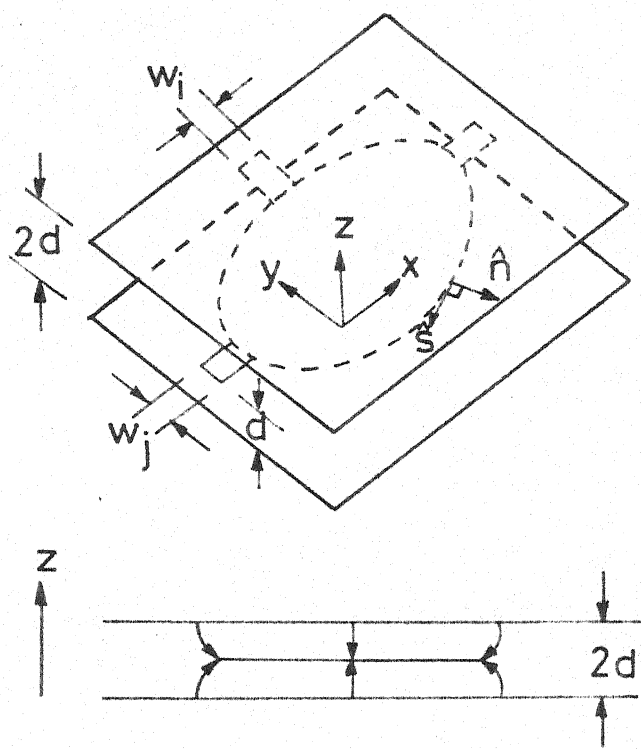
Fig. 2·1 Configuration of a stripline type planar circuit
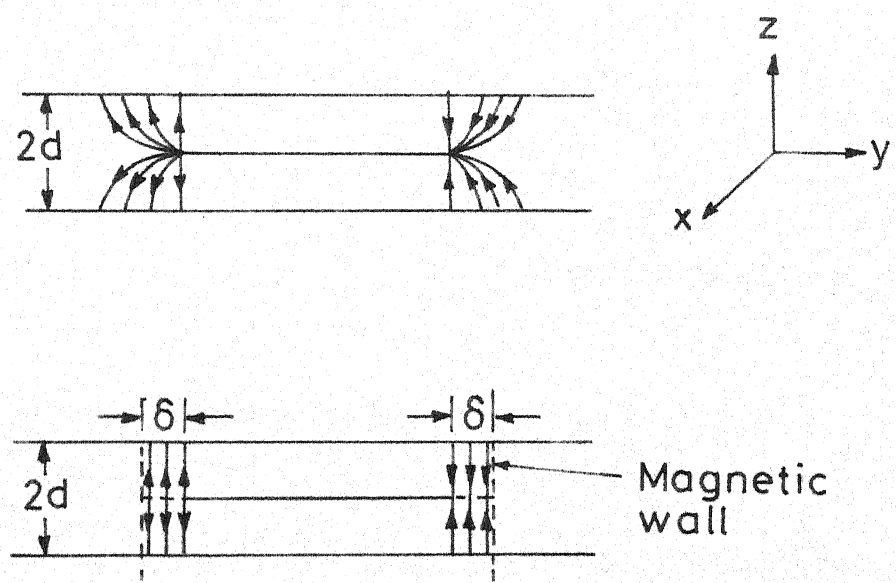
Fig. 2·2 Shift in the magnetic wall to account for the fringing field

circuit along the z-direction is very small when compared
to wavelength λ, while the other two dimensions along x
and y directions are comparable to the wavelength. The
fields can be assumed to be constant along the z-direction
because the dimension along this direction is negligible
when compared to λ.

The general Helmholtz equation, valid for a source
free region, is given as

$$(\nabla^2 + K^2)\underline{E} = 0, \qquad K^2 = \omega^2 \mu\varepsilon \qquad (2.1)$$

where μ and ε denote the permeability and permittivity of
the dielectric material and ω is the angular frequency. The
above relation holds good for describing the field within
the dielectric. At the center conductor and at the ground
planes the tangential components of the electric field
are zero. A magnetic wall is assumed to exist at the
periphery of the 2-d component (where there are no ports)
and since the fields do not vary along z-direction, both
E_x and E_y are equal to zero within the dielectric region.
The fringing field at the periphery is taken into account
by shifting the magnetic wall by a certain distance from
the physical periphery [10] as shown in Fig. 2.2.

It may be noted that the fields above and below the
central patch must be oppositely directed. In the

discussions below, the $\underline{E}$ and $\underline{H}$ can be taken to be the fields on one side of the central patch, say the lower side.

Since E_x and E_y are zero, the E-field in 2-d components may be written as

$$\underline{E} = \hat{a}_z \, E_z(x,y) \tag{2.2}$$

where $\hat{a}_z$ is a unit vector along z-direction. Substituting (2.2) in (2.1) and making $\dfrac{\partial E_z}{\partial z}$ equal to zero, one obtains

$$(\nabla_T^2 + K^2)E_z = 0 \tag{2.3}$$

where $\nabla_T^2 = \dfrac{\partial^2}{\partial x^2} + \dfrac{\partial^2}{\partial y^2}$. Using Maxwell's equation, the magnetic field can be written as

$$\underline{H} = - \frac{1}{j\omega\mu} \nabla \times \underline{E} \tag{2.4}$$

which, using (2.2), reduces to

$$\underline{H} = \frac{1}{j\omega\mu} \left(- \frac{\partial E_z}{\partial y} \, \hat{a}_x + \frac{\partial E_z}{\partial x} \, \hat{a}_y \right) \tag{2.5}$$

Surface current on a conducting sheet can be obtained from the boundary condition

$$\underline{J}_s = \hat{n} \times (\underline{H}_1 - \underline{H}_2) \tag{2.6}$$

where $\hat{n}$ is unit vector normal to the boundary and H_1 and H_2 are magnetic fields on two sides of a conducting sheet. For the central conductor of a strip line type 2-d circuits,

$\underline{H}_1 = -\underline{H}_2$ and thus

$$\underline{J}_s = \frac{2}{j\omega\mu} \left(\frac{\partial E_z}{\partial x} \hat{a}_y - \frac{\partial E_z}{\partial y} \hat{a}_x \right) \text{ amps/m} \qquad (2.7)$$

For the microstrip type planar circuit shown in Figs. 1.1(b) and 1.1(c), there is no magnetic field above the upper conducting plane and so the factor of 2 in (2.7) will not appear for obtaining surface current on the conducting sheet (assuming TEM mode of operation).

The expression for $\underline{J}_s$ in (2.7) is valid at all points on the central patch including the periphery. For points on the periphery, $\underline{J}_s$ can be written in terms of components which are normal and tangential to the periphery as

$$\underline{J}_s = \frac{2}{j\omega\mu} \left(\frac{\partial E_z}{\partial s} \hat{s} + \frac{\partial E_z}{\partial n} \hat{n} \right) \text{ amps/m} \qquad (2.8)$$

where $\hat{s}$ and $\hat{n}$ are unit vectors tangential and normal to the periphery as shown in Fig. 2.1. For points on the periphery where there are no coupling ports, the normal component of the surface current must be zero, i.e.

$$\frac{\partial E_z}{\partial n} = 0. \qquad (2.9)$$

The planar circuit can be excited either by microstrip lines (or strip lines) connected to the coupling ports or by coaxial lines. When excited by a coaxial line, the current flow at the excitation point is along the z-direction. When

excited by a strip line (or microstrip line), the current flow is normal to the periphery. The current flowing in at a coupling port is obtained using (2.7) as

$$i = - \int_W \left(\frac{2}{j\omega\mu} \frac{\partial E_z}{\partial n}\right) \, ds \qquad (2.10)$$

where W is the width of the coupling port and ds is the incremental distance along the periphery. The negative sign in (2.10) implies that the current i flows inwards whereas $\hat{n}$ in (2.8) points outwards.

The characterization of the planar components can be carried out in terms of an RF voltage V on the center conductor. Since $\frac{\partial E_z}{\partial z} = 0$, we have from (2.2),

$$V = -E_z d \qquad (2.11)$$

Equations (2.3), (2.9) and (2.10) can now be written as follows :

$$(\nabla_T^2 + K^2)V = 0 \qquad (2.12)$$

with

$$\frac{\partial V}{\partial n} = 0 \qquad (2.13)$$

for points on the periphery where there is no coupling port. The current flowing in at a coupling port is expressed as

$$i = \frac{2}{j\omega\mu \, d} \int_W \frac{\partial V}{\partial n} \, ds \qquad (2.14)$$

Solution to (2.12), with (2.13) and (2.14) as the boundary
conditions leads to the characterization of stripline type
planar components. Governing equations for other types of
planar circuits can also be obtained using similar procedure.

Various methods for obtaining the characterization of a
planar component using the above approach depend upon the
geometry of the central patch. When the planar circuit is
of a simple geometrical shape, the Green's function approach
discussed in Sections 2.2 and 2.3 is most convenient.
Green's functions are presently available for rectangles,
circles, annular rings, some types of triangles, and some
circular and annular sectors. Using the Green's functions,
the impedance matrix characterization of the circuit can be
obtained for the specified port locations. When the geome-
trical shape of the planar circuit can be considered to be
made up of simpler shapes for which the Green's functions
are available, the segmentation method can be used for
finding the characteristics of the overall circuit from
those of the various segments. In a complementary analysis
technique called Desegmentation method, some simple shapes
(whose Green's functions are available) are added to the
configuration to be analyzed such that the resulting shape
is also simple. In such a case the characterization for
the circuit can be obtained from those of the shapes added
and that of the resultant shape.Segmentation method is

discussed in Chapter Three. For the analysis of an arbitrary
shaped planar circuit numerical methods are used.

2.2 GREEN'S FUNCTION APPROACH

This approach is employed when the shape of the 2-d
patch is relatively simple. The Green's function, which
gives voltage at any point for a unit source current
excitation elsewhere, is obtained analytically. When the
locations of the ports are specified, the impedance matrix
of the component can be easily derived using the Green's
function.

2.2.1 Source currents

If a planar component is excited by a current density
J_z in z-direction at any arbitrary point (x_o, y_o) inside the
periphery (as shown in Fig. 2.3), the wave equation can be
written as

$$(\nabla_T^2 + K^2)V = -j\omega\mu d\, J_z \tag{2.15}$$

when the circuit is excited by a stripline., J_z denotes a
fictitious RF current density injected normally into the
circuit. It may be noted that the line current density
$(i_n = \frac{2}{j\omega\mu d}\, \frac{\partial V}{\partial n})$, being injected into the circuit at coupling
ports located on the periphery, can equivalently be considered
as fed normal to the circuit along Z-direction with the
magnetic wall condition $\frac{\partial V}{\partial n} = 0$, imposed all along the periphery.
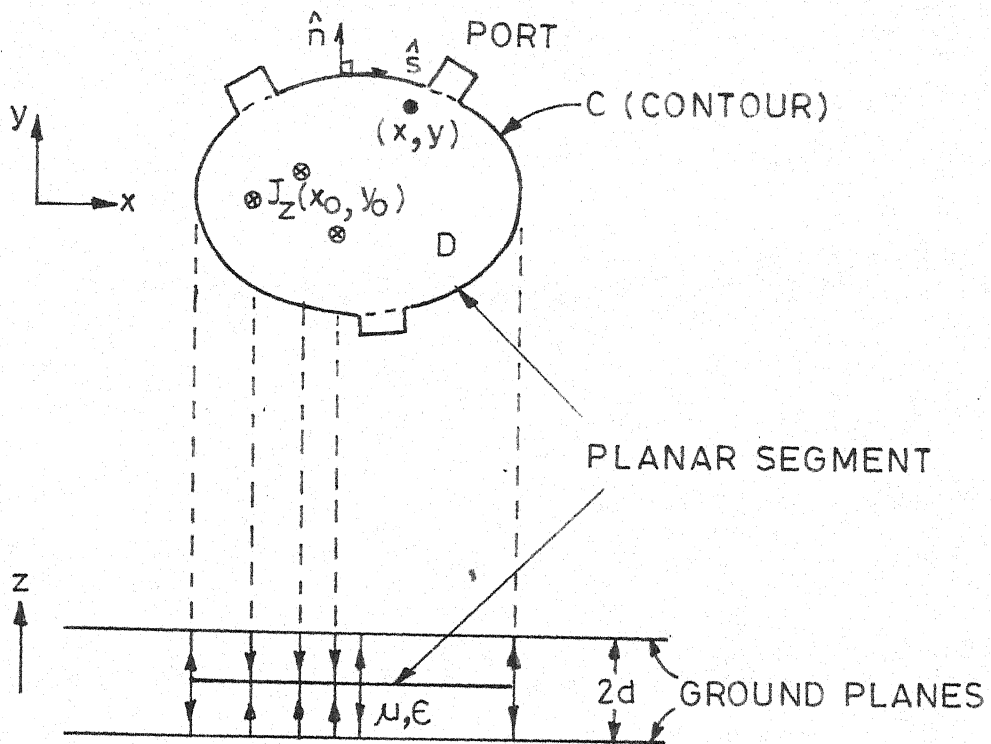
2·3 Current sources $J_z(x_0, y_0)$ and field point (x, y)

SS-SECTIONAL VIEW   SIDE VIEW
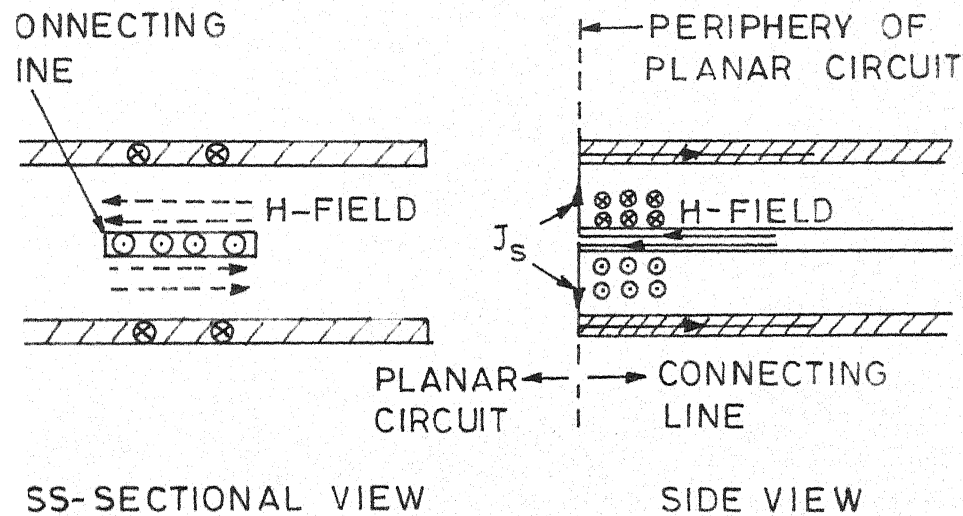
2·4 Representation of H_{tan} by an equivalent current density J_s

This can be explained as follows. For the stripline connected to a coupling port there is certain current in the central strip which flows into the planar component. One half of this current flows in the opposite direction in each of the two ground planes. At the boundary where the strip is connected to the planar component, it may be considered that the current loops close by equivalent currents along z-axis as shown in Fig. 2.4. These equivalent currents may be evaluated as given below. At the periphery, the magnetic field can be written from (2.5) and (2.11) as

$$ \underline{H} = \frac{1}{j\,\omega\,\mu d} \left(\frac{\partial V}{\partial n}\,\hat{s} - \frac{\partial V}{\partial s}\,\hat{n} \right) \tag{2.16} $$

This must be equal to the magnetic field on the other side of the interface between the planar segment and the feeding line. If the magnetic wall condition is imposed all along the periphery of the planar component, the tangential magnetic field at the periphery is modelled to be zero. In the present model, there is a change in magnetic field at the periphery (where coupling ports are located) and the equivalent fictitious surface current J_s in z-direction, obtained from the boundary condition (2.6), may be written as

$$ \underline{J}_s = - \frac{1}{j\,\omega\,\mu d}\ \frac{\partial V}{\partial n}\,\hat{a}_z \quad \text{amps/m} \tag{2.17} $$

$\underline{J}_s$ is in the negative z-direction for the region below the conducting patch as shown in Fig. 2.4. The planar component

may now be considered to be excited by line currents along the z-direction at the coupling ports with $\frac{\partial V}{\partial n} = 0$ all along the periphery.

2.2.2 Green's functions and impedance matrix

The Green's function G, for (2.15), is obtained by applying a unit line current source of $\delta(\underline{r}-\underline{r}_o)$ flowing along z-direction in the region below the central patch and located at $\underline{r} = \underline{r}_o$. The Green's function $G(r/r_o)$ is a solution of

$$(\nabla_T^2 + K^2)G = -j\omega\mu d\ \delta(\underline{r}-\underline{r}_o) \tag{2.18}$$

with the boundary condition

$$\frac{\partial G}{\partial n} = 0 \text{ (at the periphery)} \tag{2.19}$$

(For shorted boundaries G = 0 is the boundary condition).

The voltage at any point on the planar element may now be written as

$$V(x,y) = \iint_D G(x,y/x_o,y_o)\ J_z(x_o,y_o)\ dx_o\ dy_o \tag{2.20}$$

where $J_z(x_o, y_o)$ denotes a fictitious source current density injected normally and D denotes the region of the planar component enclosed by magnetic walls. In (2.20) other terms arising out of boundary conditions do not appear since both $\frac{\partial V}{\partial n}$ and $\frac{\partial G}{\partial n}$ equal zero all along the periphery of the planar component.

When the source current is fed only at ports on the periphery, the voltage V at the periphery can be written in terms of line current J, in z-direction, given by (2.17), as

$$V(s) = - \int_c G(s/s_o) \, J_s(s_o) \, ds_o \qquad (2.21)$$

where s and s_o are the distances measured along the periphery and the integral is over the entire periphery. Since the line current $J_s(s_o)$ is present only at the coupling ports, we may write (2.21) as

$$V(s) = - \sum_j \int_{W_j} G(s/s_o) \, J_s(s_o) \, ds_o \qquad (2.22)$$

where the summation on the right hand side is overall the coupling ports and W_j indicates the width of the jth coupling port. From (2.14) and (2.17), the current i_j fed in at the jth port can be written in terms of the equivalent line current in the z-direction as

$$i_j = -2 \int_{W_j} J_s(s_o) \, ds_o \qquad (2.23)$$

If the widths of the coupling ports are assumed to be small so that the line current density J_s is distributed uniformly over the width of the port, using (2.23) one gets

$$J_s(s_o) \Big|_{\text{for jth port}} = - \frac{i_j}{2W_j} \qquad (2.24)$$

Substituting (2.24) in (2.22), V(s) is obtained as

$$V(s) = \sum_j \frac{i_j}{2W_j} \int_{W_j} G(s/s_0) \, ds_0 \qquad (2.25)$$

The above equation gives voltage at any point on the periphery. To obtain the voltage V_i at the ith coupling port, average voltage over the width of the port is taken, i.e.,

$$V_i = \frac{1}{W_i} \int_{W_j} V(s) \, ds$$

$$= \sum_j \frac{i_j}{2W_i W_j} \int_{W_i} \int_{W_j} G(s/s_0) \, ds_0 \, ds \qquad (2.26)$$

From (2.26), the elements of the impedance matrix of the planar component can be written as

$$Z_{ij} = \frac{1}{2W_i W_j} \int_{W_i} \int_{W_j} G(s/s_0) \, ds_0 \, ds \qquad (2.27)$$

One can thus determine the impedance matrix of the component.

2.3 EVALUATION OF GREEN'S FUNCTIONS

The evaluation of Green's function, for a given shape of 2-d component, requires solution of (2.18) with the boundary condition $\frac{\partial G}{\partial n} = 0$ for magnetic wall boundaries and $G = 0$ for electric wall boundaries. There are basically two methods for obtaining the Green's function : i) the

method of images, and ii) the expansion of Green's function in terms of eigen functions.

2.3.1 Method of images

An analytical solution of the differential equation (2.18) can be obtained if the right hand side is a periodic function. For this purpose, additional current sources of the type $\delta(\underline{r}-\underline{r}_s)$ are placed at points $\underline{r}_s$ outside the region of the planar component. These additional sources can be thought of as obtained by taking multiple images of the line source at $\underline{r}_0$ with respect to the various magnetic walls of the planar component. In case of electric walls (shorted boundaries), the images of the line source at $\underline{r}_0$ will be negative (i.e. $-\delta(\underline{r}-\underline{r}_s)$). The source term in (2.18) gets modified and the boundary conditions are satisfied by the voltage V produced by the source and its images. It should be noted that the additional sources are all outside the region of the planar component and therefore, the solution G still represents the Green's function for the geometrical shape of the planar component.

The source pattern used in (2.18) is now periodic and, therefore, its Fourier series expansion can be obtained. The Green's function can then be expressed as an infinite series summation of the functions obtained in the Fourier series expansion. These are the Eigen

functions. The coefficients, in the series summation for Green's function, can then be obtained by substituting it in (2.18).

The method of images, discussed above, is restricted to the shapes enclosed by boundaries which are straight lines. This is because, the only mirror which gives point image for a point source is a plane mirror. Even for polygonal shapes with all magnetic walls or all electric walls the images can be uniquely specified in the two-dimensional space only if the internal angle at each vertex of the polygon is a submultiple of π. For polygons with mixed boundary conditions (i.e. some sides as electric walls and rest magnetic walls), the angles at all vertices where one side is electric wall and the other magnetic wall should be 90° or a submultiple of 90°. Other vertices should have angles which are submultiples of 180°. Thus, the method of images is restricted to rectangular and the triangular shapes.

2.3.2 Expansion of Green's function in eigen functions

The Green's function $G(r/r_0)$ is given by the solution of (2.18) with the boundary condition $\frac{\partial G}{\partial n} = 0$ for magnetic wall and $G = 0$ for electric wall. In this method, the G is expanded in terms of known eigen functions of the corresponding Helmholtz's equation given by (2.12) with the boundary conditions $\frac{\partial V}{\partial n} = 0$ for magnetic boundary (wall) and $V = 0$ for electric walls.

Let $\psi_n(\underline{r})$ represent the normalized eigen functions of (2.12) and K_n^2 be the corresponding eigen values so that

$$\nabla_T^2 \psi_n + K_n^2 \psi_n = 0 \tag{2.28}$$

where each eigen function ψ_n is assumed to satisfy the boundary conditions imposed on G. The Green's function $G(\underline{r}/\underline{r}_0)$ can be expanded in a series of eigen functions if the normalized eigen functions ψ_n form an orthonormal set, i.e.

$$G(\underline{r}/\underline{r}_0) = \sum_m A_m \psi_m(\underline{r}) \quad \text{if} \quad \int\int_D \psi_n^* \psi_m \, dr = \begin{cases} 1, & \text{if } n = m \\ 0, & \text{otherwise} \end{cases} \tag{2.29}$$

where the superscript $*$ denotes complex conjugate, and the region of integration D is bounded by the periphery of the planar component, at which ψ_n satisfy the boundary conditions. Substituting (2.29) into (2.18), and using (2.28), one gets

$$\sum_m A_m(K^2 - K_m^2) \psi_m(\underline{r}) = -j\omega\mu d \, \delta(\underline{r} - \underline{r}_0) \tag{2.30}$$

Multiplying both sides of the above equation by $\psi_n^*(\underline{r})$ and integrating over the region D, one obtains

$$\sum_m A_m(K^2 - K_m^2) \int\int_D \psi_m(\underline{r}) \psi_n^*(\underline{r}) \, dx \, dy = -j\omega\mu d \, \psi_n^*(\underline{r}_0) \tag{2.31}$$

which, by virtue of the orthonormal property, reduces to

$$A_n(K^2 - K_n^2) = -j\,\omega\mu d\;\psi_n^*(\underline{r}_o) \tag{2.32}$$

Thus,

$$A_n = \frac{j\,\omega\mu d\,\psi_n^*(\underline{r}_o)}{K_n^2 - K^2} \tag{2.33}$$

so that

$$G(\underline{r}/\underline{r}_o) = j\,\omega\mu d\sum_n \frac{\psi_n(\underline{r})\,\psi_n^*(\underline{r}_o)}{K_n^2 - K^2} \tag{2.34}$$

is the required Green's function expansion. For a lossless circuit, ψ_n are real and the complex conjugate is not needed in (2.34). This method is restricted to cases where the eigen functions are known.

2.4 GREEN'S FUNCTIONS FOR MIXED BOUNDARY 30°-60° RIGHT ANGLED TRIANGLES

In this section, the Green's functions are developed for mixed boundary 30°-60° right-angled triangles. The Green's functions for triangular shapes are obtained using the method of images. The Green's function for the triangle with open boundary shown in Fig. 2.5 is given as [5]

$$G(x, y/x_o, y_o)$$

$$= 8j\,\omega\mu d\sum_{m=-\infty}^{\infty}\sum_{n=-\infty}^{\infty} \frac{T_1(x_o, y_o)\,T_1(x, y)}{16\sqrt{3}\pi^2(m^2 + mn + n^2) - 9\sqrt{3}a^2K^2} \tag{2.35}$$

where

$$T_1(x,y) = (-1)^l \cos(\frac{2\pi lx}{\sqrt{3}a}) \cos[\frac{2\pi(m-n)y}{3a}]$$

$$+ (-1)^m \cos(\frac{2\pi mx}{\sqrt{3}a}) \cos[\frac{2\pi(n-l)y}{3a}]$$

$$+ (-1)^n \cos(\frac{2\pi nx}{\sqrt{3}a}) \cos[\frac{2\pi(l-m)y}{3a}] \qquad (2.36)$$

with the condition that the integers l,m and n satisfy

$$l+m+n = 0 \qquad (2.37)$$

2.4.1 Green's function for 30°-60° right-angled triangle when the side opposite to angle 60° is electric wall and other two sides are magnetic walls

As explained in the Section 2.3.1, the images of the line source at (x_o, y_o) with respect to the three sides of the triangle shown in Fig. 2.6(a) which are two magnetic walls and one electric wall can be assumed as the additional line sources outside the triangle. The locations of these multiple images are shown in Fig. 2.6(b).

It can be seen that the periodicity of the pattern is 3a along the y-axis and $\sqrt{3}a$ along the x-axis. Hence, ABCDEF is chosen as a basic cell which contains 24 line sources in 24 triangular regions as shown in Fig. 2.6(b). It may be noted that a solution for G with this set of multiple sources, will satisfy (2.18) in the original region of
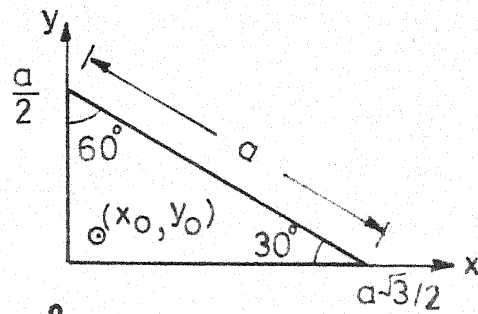
Fig.2·5 A 30°-60° right-angled triangle with open
boundary

(a)

○ POSITIVE SOURCE
● NEGATIVE SOURCE
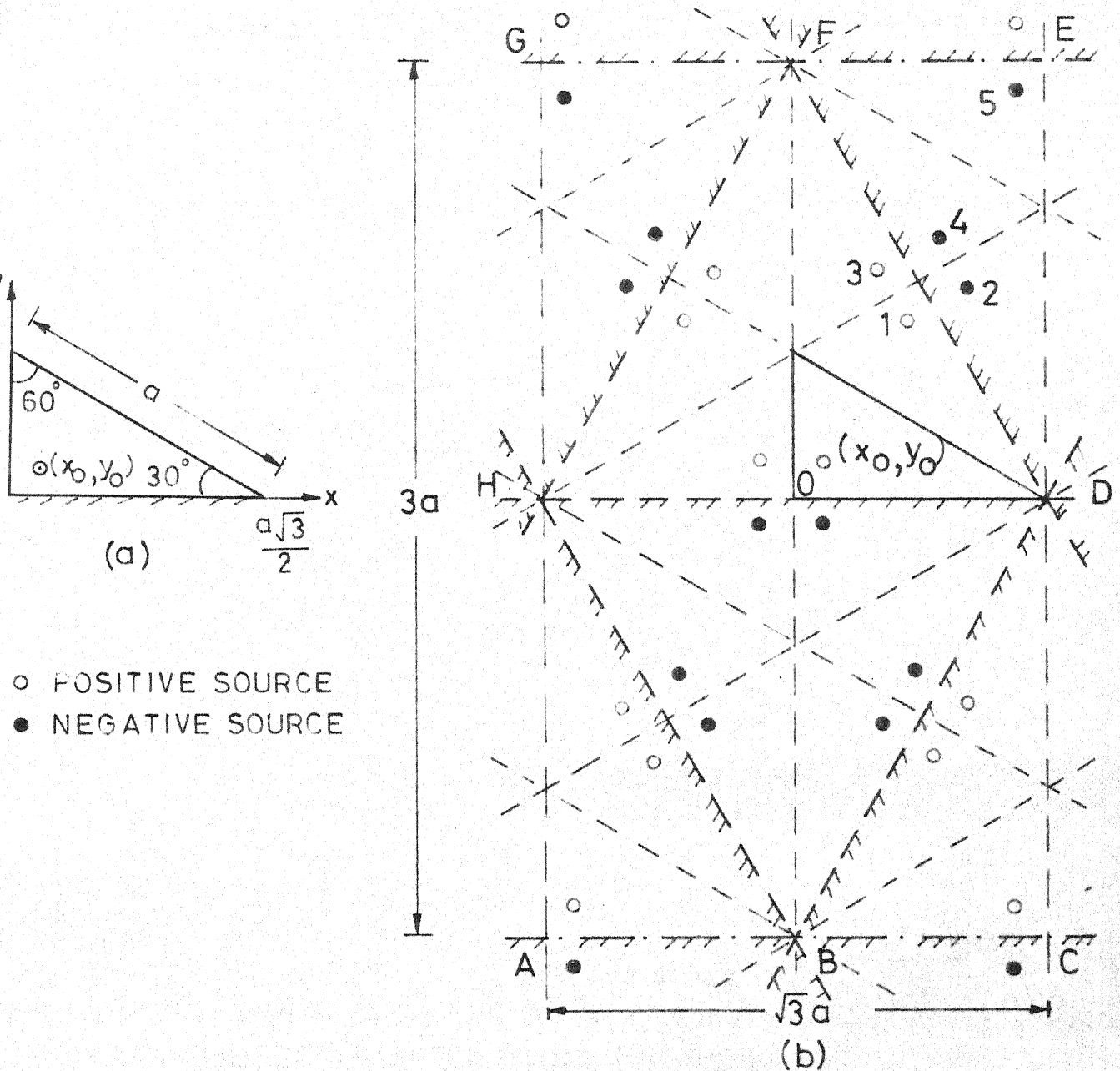
Fig.2·6 (a) A 30°-60° right-angled triangle with the
side opposite to 60° as an electric wall
(b) location of image sources

interest, since the boundary conditions $\frac{\partial G}{\partial n} = 0$ for magnetic walls and $G = 0$ for electric walls is satisfied for all the 24 triangles in the basic cell.

For the line source at (x_o, y_o) in Fig. 2.6(b), the coordinates of the image line sources in ODEF can be expressed in terms of (x_o, y_o) as

$$x_1 = \frac{x_o}{2} - \frac{\sqrt{3}}{2} y_o + \frac{a\sqrt{3}}{4}$$

$$y_1 = -\frac{\sqrt{3}}{2} x_o - \frac{y_o}{2} + \frac{3a}{4}$$

for image (1)

$$x_2 = \frac{x_o}{2} + \frac{\sqrt{3}}{2} y_o + \frac{a\sqrt{3}}{4}$$

$$y_2 = -\frac{\sqrt{3}}{2} x_o + \frac{y_o}{2} + \frac{3a}{4}$$

for image (2)

$$x_3 = -\frac{x_o}{2} - \frac{\sqrt{3}}{2} y_o + \frac{a\sqrt{3}}{4}$$

$$y_3 = \frac{\sqrt{3}}{2} x_o - \frac{y_o}{2} + \frac{3a}{4}$$

for image (3)

$$x_4 = -\frac{x_o}{2} + \frac{\sqrt{3}}{2} y_o + \frac{a\sqrt{3}}{4}$$

$$y_4 = \frac{\sqrt{3}}{2} x_o + \frac{y_o}{2} + \frac{3a}{4}$$

for image (4)

$$x_5 = -x_o + \frac{a\sqrt{3}}{2}$$

$$y_5 = -y_o + \frac{3a}{2}$$

for image (5)

The Fourier series expansions for each of the 24-line sources, which repeat periodically in two-dimensional space, are obtained. The corresponding terms of these 24 expressions are added together and the resulting expression identical to the right-hand side of (2.18) in the original triangular region can be expressed as

$$
-\frac{8j\omega\mu d}{3\sqrt{3}a^2} \sum_{m=-\infty}^{\infty} \sum_{n=-\infty}^{\infty} \cos(\frac{2\pi mx}{\sqrt{3}a}) \sin[\frac{2\pi(m+2n)y}{3a}] \{(-1)^n \cdot
$$

$$
\cos[\frac{2\pi(m+n)x_o}{\sqrt{3}a}] \sin[\frac{2\pi(m-n)y_o}{3a}] + \cos(\frac{2\pi mx_o}{\sqrt{3}a}) \sin[\frac{2\pi y_o(m+2n)}{3a}]
$$

$$
-(-1)^{m+n} \cos(\frac{2\pi nx_o}{\sqrt{3}a}) \sin[\frac{2\pi y_o}{3a}(2m+n)] \} \tag{2.38}
$$

By substituting $l = -(m+n)$, this reduces to

$$
-\frac{8j\omega\mu d}{3\sqrt{3}a^2} \sum_{-\infty}^{\infty} \sum_{-\infty}^{\infty} (-1)^m \cos(\frac{2\pi mx}{\sqrt{3}a}) \sin[\frac{2\pi(n-1)y}{3a}] T_1(x_o, y_o) \tag{2.39}
$$

where $T_1(x,y)$ is defined as

$$
T_1(x,y) = (-1)^l \cos(\frac{2\pi lx}{\sqrt{3}a}) \sin[\frac{2\pi(m-n)y}{3a}] + (-1)^m \cdot
$$

$$
\cos(\frac{2\pi mx}{\sqrt{3}a}) \sin[\frac{2\pi(n-1)y}{3a}] -(1)^n \cos(\frac{2\pi nx}{\sqrt{3}a}) \sin[\frac{2\pi(1-m)y}{3a}] \tag{2.40}
$$

with the condition that the integers l, m and n satisfy

$$
l+m+n = 0
$$

It can be seen that

$$\sum \sum (-1)^l \cos(\frac{2\pi l x}{\sqrt{3}a}) \sin[\frac{2\pi(m-n)y}{3a}] \, T_1(x_o, y_o) =$$

$$\sum \sum (-1)^m \cos(\frac{2\pi m x}{\sqrt{3}a}) \sin[\frac{2\pi(n-1)y}{3a}] \, T_1(x_o, y_o) =$$

$$\sum \sum (-1)^n \cos(\frac{2\pi n x}{\sqrt{3}a}) \sin[\frac{2\pi(1-m)y}{3a}] \, T_1(x_o, y_o) \qquad (2.41)$$

Using (2.41), expression (2.39) can be rewritten as

$$- \frac{8j\,\omega\mu d}{9\sqrt{3}a^2} \, \sum \sum T_1(x_o, y_o) \, T_1(x, y) \qquad (2.42)$$

It can be verified that the functions $T_1(x,y)$ satisfy the boundary conditions ($\frac{\partial G}{\partial n} = 0$ for magnetic walls and $G = 0$ for electric walls), for the triangle shown in Fig. 2.6(a). The functions $T_1(x,y)$ are the eigen functions for this triangle. The Green's function G can now be written in terms of these eigen functions $T_1(x,y)$ as

$$G = \sum_{m=-\infty}^{\infty} \sum_{n=-\infty}^{\infty} A_{mn} \, T_1(x,y) \qquad (2.43)$$

Substituting (2.43) in the left hand side of (2.18), we get

$$(\nabla_T^2 + K^2)G = \sum_{-\infty}^{\infty} \sum_{-\infty}^{\infty} [K^2 - \frac{16\pi^2}{9a^2} \, [m^2 + mn + n^2] \, A_{mn} \, T_1(x,y) \qquad (2.44)$$

Since (2.44) and (2.42) are equal for all values of x and y, we have by comparison

$$A_{mn} = \frac{8j\,\omega\mu d \, T_1(x_o, y_o)}{16\sqrt{3}\pi^2(m^2 + mn + n^2) - 9\sqrt{3}a^2 K^2} \qquad (2.45)$$

Substituting (2.45) in (2.43), one obtains

$$G(x,y/x_o,y_o) = 8j\omega\mu d \sum_{m=-\infty}^{\infty} \sum_{n=-\infty}^{\infty} \frac{T_1(x_o,y_o) \ T_1(x,y)}{16\sqrt{3}\pi^2(m^2+n^2+mn)-9\sqrt{3}a^2K^2}$$

$$(2.46)$$

which is the required Green's function for the 30°-60° right-angled triangle shown in Fig. 2.6(a).

2.4.2 Green's function for 30°-60° right-angled triangle when all the three sides of the triangle are electric walls

The 30°-60° right-angled triangle with shorted boundary is shown in the Fig. 2.7(a) and the images of the line source at (x_o,y_o) with respect to the three sides of the triangle which are all electric walls (shorted walls) are shown in the Fig. 2.7(b). The number of images inside the basic cell is 24 as in the previous case, but, the signs of the images are different and the periodicity of the pattern is same as in the previous case. Adding the terms in Fourier series expressions for each of the 24 line sources in the basic cell, the resulting expression equivalent to the right-hand side of (2.18) can be expressed as

$$-\frac{8j\omega\mu d}{3\sqrt{3}a^2} \sum_{m=-\infty}^{\infty} \sum_{n=-\infty}^{\infty} \sin(\frac{2\pi m x}{\sqrt{3}a}) \sin[\frac{2\pi(m+2n)y}{3a}] \{ \sin(\frac{2\pi m x_o}{\sqrt{3}a}) \cdot$$

$$\sin[\frac{2\pi(m+2n)y_o}{3a}] -(-1)^n \sin[\frac{2\pi(m+n)x_o}{\sqrt{3}a}] \sin[\frac{2\pi(m-n)y_o}{3a}] -$$

$$(-1)^{m+n} \sin(\frac{2\pi n x_o}{\sqrt{3}a}) \sin[\frac{2\pi y_o(2m+n)}{3a}] \} \qquad (2.47)$$
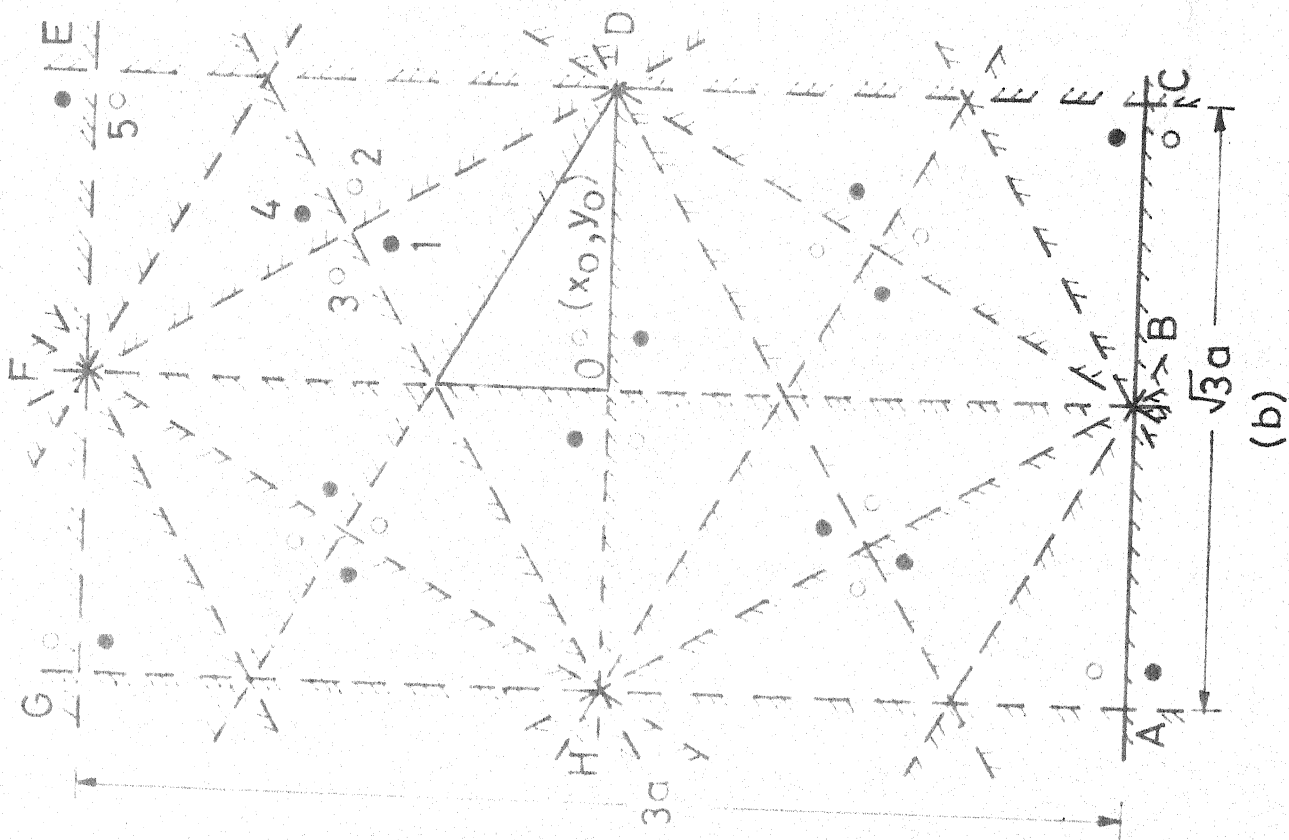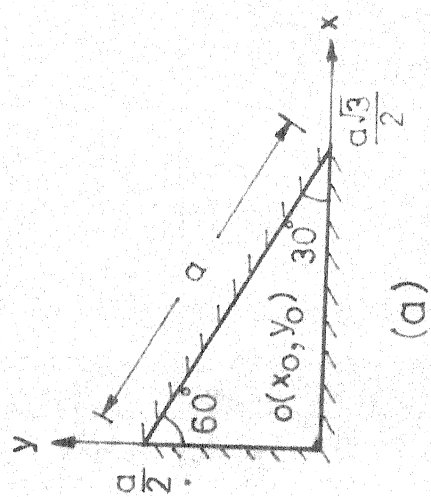
Fig. 2·7(a) A 30°-60° right-angled triangle with all the three sides as electric walls (b) location of images

Substituting $1 = -(m+n)$, this reduces to

$$- \frac{8j\omega\mu d}{3\sqrt{3}a^2} \sum\sum (-1)^m \sin(\frac{2\pi mx}{\sqrt{3}a}) \sin[\frac{2\pi(n-1)y}{3a}] T_2(x_0,y_0) \qquad (2.48)$$

where $T_2(x,y)$ is defined as

$$T_2(x,y) = -(-1)^1 \sin(\frac{2\pi 1x}{\sqrt{3}a}) \sin[\frac{2\pi(m-n)y}{3a}] + (-1)^m \sin(\frac{2\pi mx}{\sqrt{3}a}) \cdot$$

$$\sin[\frac{2\pi(n-1)y}{3a}] - (-1)^n \sin(\frac{2\pi nx}{\sqrt{3}a}) \sin[\frac{2\pi(1-m)y}{3a}] \qquad (2.49)$$

with the condition that the integers 1,m and n satisfy

$$1 + m + n = 0$$

It can be seen that

$$- \sum\sum (-1)^1 \sin(\frac{2\pi 1x}{\sqrt{3}a}) \sin[\frac{2\pi(m-n)y}{3a}] T_2(x_0,y_0) = \sum\sum (-1)^m \sin(\frac{2\pi mx}{\sqrt{3}a}) \cdot$$

$$\sin[\frac{2\pi(n-1)y}{3a}] T_2(x_0,y_0) = - \sum\sum (-1)^n \sin(\frac{2\pi nx}{\sqrt{3}a})$$

$$\sin[\frac{2\pi(1-m)y}{3a}] T_2(x_0,y_0) \qquad (2.50)$$

Using (2.50), expression (2.48) can be rewritten as

$$- \frac{8j\omega\mu d}{9\sqrt{3}a^2} \sum\sum T_2(x_0,y_0) T_2(x,y) \qquad (2.51)$$

$T_2(x,y)$ is the potential function of the triangle shown in Fig. 2.7(a). The Green's function G can now be written in terms of these potential functions $T_2(x,y)$ as

$$G = \sum_{m=-\infty}^{\infty} \sum_{n=-\infty}^{\infty} A_{mn} T_2(x,y) \qquad (2.52)$$

Substituting (2.52) in the left-hand side of (2.18), we get

$$(\nabla_T^2+K^2)G = \sum_{m=-\infty}^{\infty} \sum_{n=-\infty}^{\infty} [K^2 - \frac{16\pi^2}{9a^2}(m^2+mn+n^2)]A_{mn} \, T_2(x,y)$$

(2.53)

Since (2.53) and (2.51) are equal for all values of x and y, we have by comparison

$$A_{mn} = \frac{8j\,\omega\mu d \, T_2(x_o,y_o)}{16\sqrt{3}\pi^2(m^2+mn+n^2)-9\sqrt{3}a^2K^2}$$

(2.54)

Substituting (2.54) in (2.52) we have

$$G(x,y/x_o,y_o) = 8j\,\omega\mu d \sum_{m=-\infty}^{\infty} \sum_{n=-\infty}^{\infty} \frac{T_2(x_o,y_o) \, T_2(x,y)}{16\sqrt{3}\pi^2(m^2+mn+n^2)-9\sqrt{3}a^2K^2}$$

(2.55)

which is the required Green's function for the 30°-60° right-angled triangle with shorted boundary.

2.4.3 Green's function for 30°-60° right-angled triangle when the side of the triangle opposite to 60° is magnetic wall and the other two sides are electric walls

The images of the line source at (x_o,y_o) with respect to the three sides of the triangle shown in Fig. 2.8(a) are depicted in the Fig. 2.8(b). As in the previous cases the number of total images inside a basic cell is 24 distributed one each in 24 triangular regions of the basic cell, and the periodicity is 3a along y-axis and $\sqrt{3}$a along x-axis. The nature of the images is different than that of the previous cases. The expression obtained by adding the terms
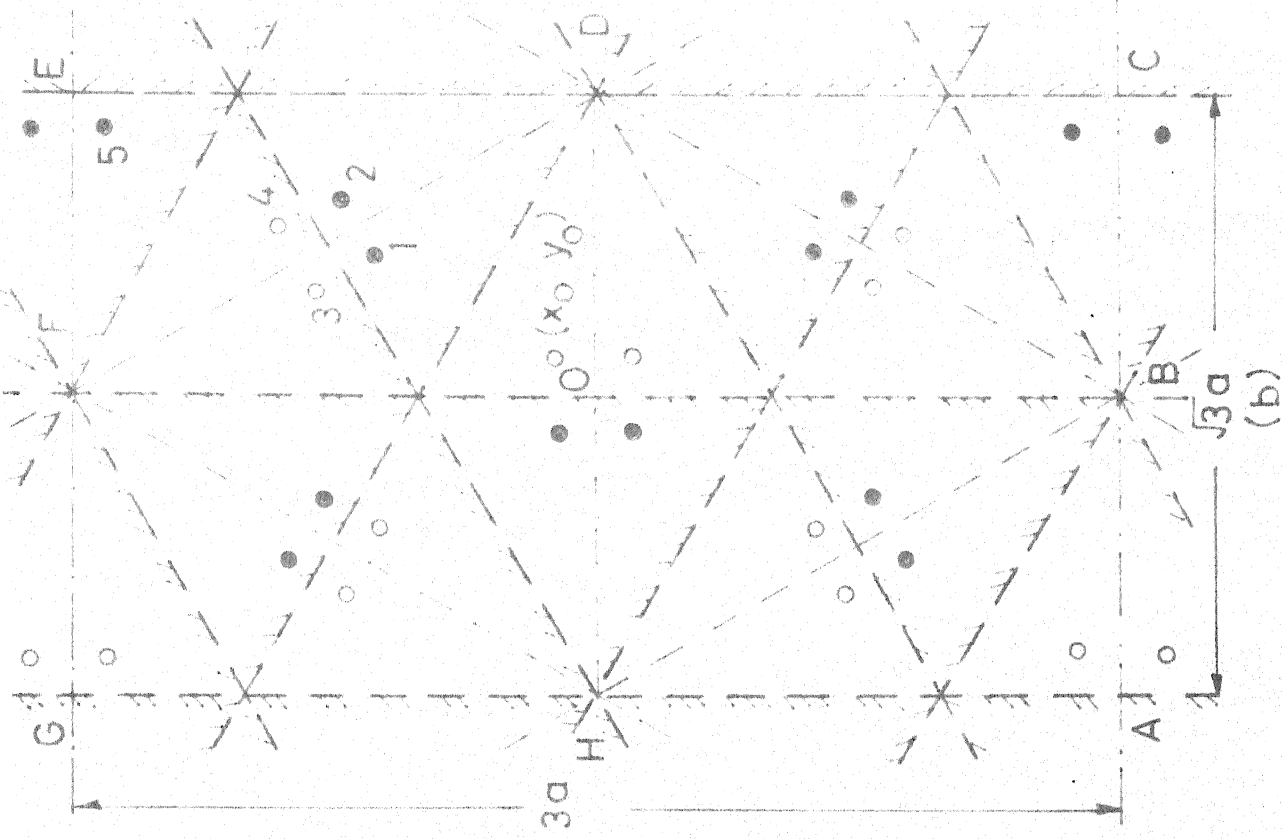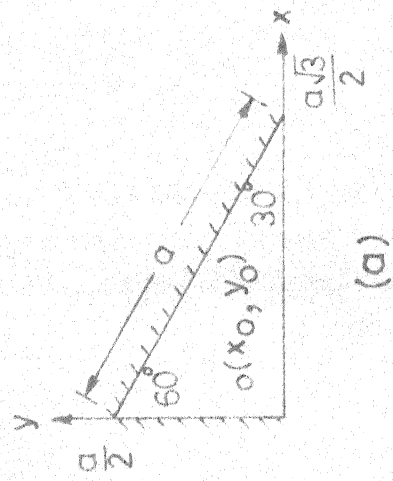
Fig.2·8(a) A 30°-60° right-angled triangle with the sides opposite to 30° and 90° as electric walls (b) location of images

in Fourier series expressions for each of the 24 line sources in the basic cell is equivalent to the right-hand side of (2.18) and is written as

$$- \frac{8j\,\omega\mu d}{3\sqrt{3}a^2} \sum_{m=-\infty}^{\infty} \sum_{n=-\infty}^{\infty} \sin(\frac{2\pi m x}{\sqrt{3}a}) \cos[\frac{2\pi(m+2n)y}{3a}] \{ \sin(\frac{2m\pi x_o}{\sqrt{3}a}) \cdot$$

$$\cos[\frac{2\pi(m+2n)y_o}{3a}] - (-1)^n \sin[\frac{2\pi(m+n)x_o}{\sqrt{3}a}]\cos[\frac{2\pi(m-n)y_o}{3a}] + (-1)^{m+n} \cdot$$

$$\sin(\frac{2\pi n x_o}{\sqrt{3}a}) \cos[\frac{2\pi(2m+n)y_o}{3a}] \} \qquad (2.56)$$

Now substituting $l = -(m+n)$, this reduces to

$$- \frac{8j\,\omega\mu d}{3\sqrt{3}a^2} \sum \sum (-1)^m \sin(\frac{2\pi m x}{\sqrt{3}a}) \cos[\frac{2\pi(n-1)y}{3a}] T_3(x_o, y_o) \qquad (2.57)$$

where $T_3(x,y)$ is defined as

$$T_3(x,y) = -(-1)^l \sin(\frac{2\pi l x}{\sqrt{3}a}) \cos[\frac{2\pi y(m-n)}{\sqrt{3}a}] + (-1)^m \sin(\frac{2\pi m x}{\sqrt{3}a}) \cdot$$

$$\cos[\frac{2\pi(n-1)y}{3a}] + (-1)^n \sin(\frac{2\pi n x}{\sqrt{3}a}) \cos[\frac{2\pi(1-m)y}{3a}] \qquad (2.58)$$

with the condition that the integers l, m and n satisfy

$$l + m + n = 0$$

It can be seen that

$$- \sum \sum (-1)^l \sin(\frac{2\pi l x}{\sqrt{3}a}) \cos[\frac{2\pi(m-n)y}{3a}] T_3(x_o, y_o)$$

$$= \sum \sum (-1)^m \sin(\frac{2\pi m x}{\sqrt{3}a}) \cos[\frac{2\pi(n-1)y}{3a}] T_3(x_o, y_o)$$

$$= \sum \sum (-1)^n \sin(\frac{2\pi n x}{\sqrt{3}a}) \cos[\frac{2\pi(1-m)y}{3a}] \cdot T_3(x_o, y_o). \qquad (2.59)$$

Using (2.59), expression (2.57) can now be rewritten as

$$- \frac{8j\omega\mu d}{9\sqrt{3}a^2} \sum\sum T_3(x_o,y_o)\, T_3(x,y) \tag{2.60}$$

It can be verified that the function $T_3(x,y)$ satisfies the boundary conditions $\frac{\partial G}{\partial n} = 0$ for magnetic walls, and $G = 0$ for electric walls for the triangle shown in Fig. 2.8(a).

The Green's function G can now be written in terms $T_3(x,y)$ as

$$G = \sum_{m=-\infty}^{\infty} \sum_{n=-\infty}^{\infty} A_{mn}\, T_3(x,y) \tag{2.61}$$

Substituting (2.61) in the left-hand side of (2.18), we get

$$(\nabla_T^2 + K^2)G = \sum\sum \left[K^2 - \frac{16\pi^2}{9a^2}(m^2+mn+n^2)\right] A_{mn}\, T_3(x,y) \tag{2.62}$$

Since (2.62) and (2.60) are equal for all values of x and y, we have by comparison

$$A_{mn} = \frac{8j\omega\mu d\, T_3(x_o,y_o)}{16\sqrt{3}\pi^2(m^2+mn+n^2)-9\sqrt{3}a^2K^2} \tag{2.63}$$

Substituting (2.63) in (2.61) we have

$$G(x,y/x_o,y_o) = 8j\omega\mu d \sum_{-\infty}^{\infty} \sum_{-\infty}^{\infty} \frac{T_3(x_o,y_o)\, T_3(x,y)}{16\sqrt{3}\pi^2(m^2+mn+n^2)-9\sqrt{3}a^2K^2} \tag{2.64}$$

which is the required Green's function for the geometry shown in Fig. 2.8(a).

2.5 GREEN'S FUNCTION FOR EQUILATERAL TRIANGLE WHEN ALL THE THREE SIDES ARE ELECTRIC WALLS

The Green's function for an equilateral triangle shown in Fig. 2.9(a) can be obtained by using the principle of odd-mode and even-mode symmetry. The odd-mode and even-mode parts for the triangle considered are shown in Figs. 2.9(b) and 2.9(c). The Green's functions for these odd-mode and even-mode sections (i.e. 30°-60° right-angle triangle with all electric walls, and 30°-60° right-angle triangle with the side opposite to 60° as magnetic wall and other two sides as electric walls) have been developed in the Sections (2.4.2) and (2.4.3) respectively. On adding (2.55) and (2.64), one gets

$$G(x,y/x_o,y_o) = \frac{8j\,\omega\mu d}{[16\sqrt{3}\pi(m^2+mn+n^2)-9\sqrt{3}a^2K^2]} \cdot$$

$$\sum_{m=-\infty}^{\infty}\sum_{n=-\infty}^{\infty} [T_2(x_o,y_o)\,T_2(x,y) \qquad (2.65)$$

$$+\,T_3(x_o,y_o)\,T_3(x,y)]$$

where $T_3(x,y)$ and $T_2(x,y)$ are defined in (2.49) and (2.58) respectively.

2.6 GREEN'S FUNCTIONS FOR CIRCULAR SECTORS WITH MIXED BOUNDARIES

The circular sectors are used in microstrip bends and their characterizations are needed to analyze these bends

(a)

(b)

(c)
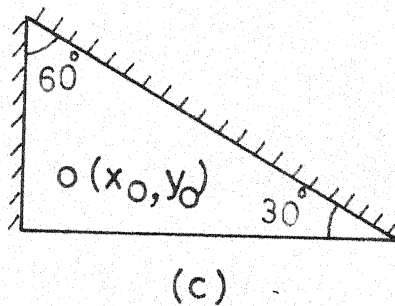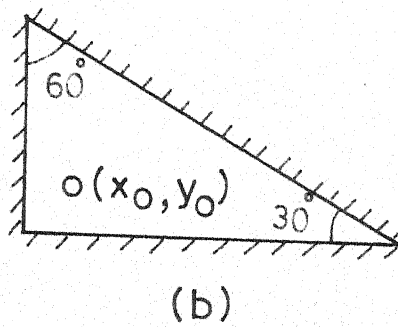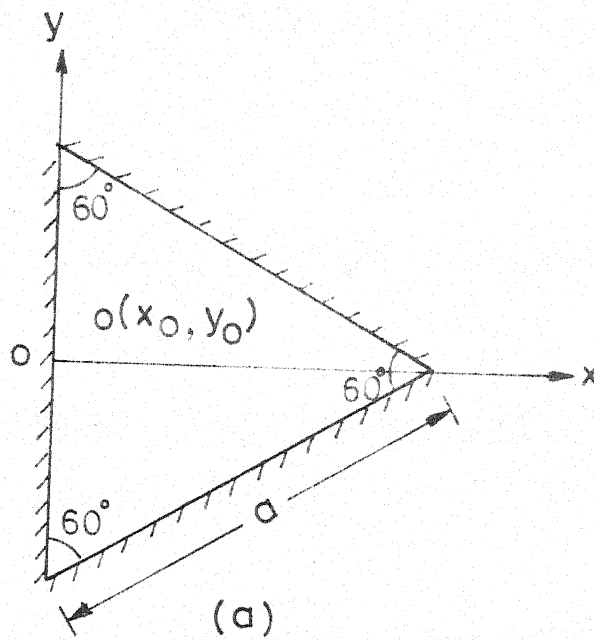
Fig. 2.9 (a) An equilateral triangular segment with shorted boundary (b) its odd-mode section (c) its even-mode section

accurately. The sectoral configurations are also used in microstrip antennas. The sectoral antennas with mixed boundaries can be used in arrays to reduce the mutual coupling (due to surface waves in larger thickness substrates) between the adjacent elements. The various possible mixed boundary sectoral segments are shown in the Fig. 2.10.

The Green's functions for the sectoral segments are obtained by expansion in a series of eigen functions explained in Section 2.3.2. The Green's function for the sector (all magnetic walls) shown in Fig. 2.10(a) is given as [6]

$$G(\underline{r}/\underline{r}_i) = \frac{2dl}{j\omega\epsilon\pi a^2} + 2jl\,\omega\,\mu d\sum_{m=0}^{\infty}\sum_{n=1}^{\infty} \cdot$$

$$\frac{\sigma J_v(K_{vn}\,\rho_i)J_v(K_{vn}\,\rho)\cos(v\varphi_i)\cos(v\varphi)}{\pi(a^2-v^2/K_{vn}^2)(K_{vn}^2-K^2)J_v^2(K_{vn}a)} \tag{2.66}$$

where $l = \dfrac{\pi}{\varphi_o}$; $v = \dfrac{m\pi}{\varphi_o}$, and $K_{vn} = \dfrac{P_{vn}}{a}$, where

P_{vn} is the nth root of the derivative of the Bessel function of the first kind and order v. $\sigma = 1$ for $v=0$ and 2 for $v > 0$.

2.6.1 Green's function for sector with straight edges shorted

For the circular sector shown in Fig. 2.10(b), the angular eigen functions which satisfy the boundary condition $V = 0$ at $\varphi = 0$ and $\varphi = \varphi_o$ are given as

$$\varphi_m = A_m \sin v\varphi, \quad v = \frac{m\pi}{\varphi_o} . \tag{2.67}$$
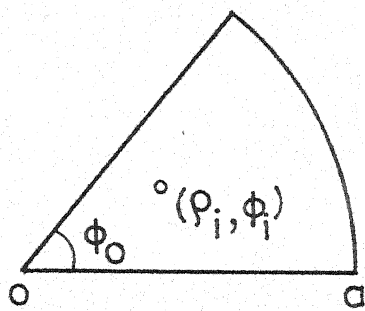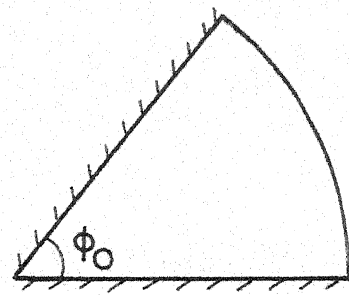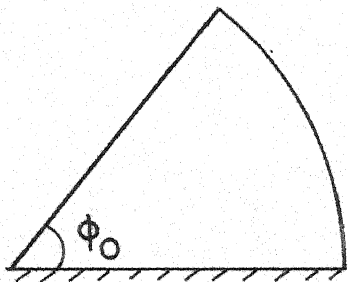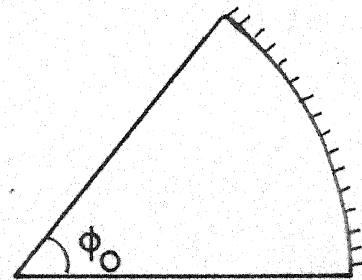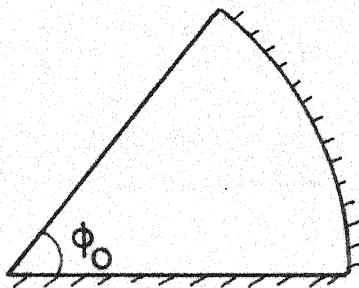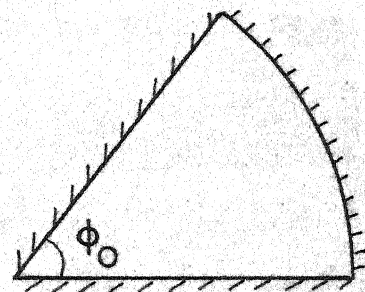
Fig. 2.10 Circular sectors

Since

$$\int_0^{\varphi_0} \sin^2 \frac{m\pi\varphi}{\varphi_0} \, d\varphi = \begin{cases} \dfrac{\varphi_0}{2} &, \quad \text{for } m \neq 0 \\ \\ 0 & \quad \text{for } m = 0 \end{cases} \qquad (2.68)$$

the normalized eigen functions are

$$\varphi_m = \sqrt{\frac{2}{\varphi_0}} \ \sin v\varphi \qquad\qquad (2.69)$$

The radial eigen functions which satisfy the boundary condi-
tion $\frac{\partial V}{\partial n} = 0$ at $\rho = a$ are given as

$$R_n = B_n \ J_v(K_{vn} \ \rho) \qquad\qquad (2.70)$$

where

$$K_{vn} = \frac{P_{vn}}{a} \quad, \quad P_{vn} \text{ is the nth zero of the derivative of}$$
$$\text{the Bessel function of the first kind and}$$
$$\text{order } v.$$

The radial eigen functions must now be normalized over the
interval $0 \leqslant \rho \leqslant a$ by setting

$$B_n = \frac{1}{[\ \int_0^a \rho \ J_v^2 (K_{vn} \ \rho \ ) d\rho]^{\frac{1}{2}}} \qquad\qquad (2.71)$$

The following formulas are used for normalizing the eigen
function.

$$\int_0^a x \{J_n(x)\}^2 \, dx = \tfrac{1}{2}a^2 \{J_n^2(a)+J_{n+1}^2(a)\} - naJ_n(a)J_{n+1}(a)$$

$$(2.72a)$$

$$2J_n'(x) = J_{n-1}(x) - J_{n+1}(x) \qquad\qquad (2.72b)$$

$$\frac{2n}{x}J_n(x) = J_{n-1}(x) + J_{n+1}(x) \qquad\qquad (2.72c)$$

The B_n is obtained as

$$B_n = \frac{1}{\left[\tfrac{1}{2}J_v^2(K_{vn}a)\left[a^2 - \dfrac{v^2}{K_{vn}^2}\right]\right]^{\frac{1}{2}}} \qquad\qquad (2.73)$$

Then, using (2.34) the Green's function can be written as

$$G(\underline{r}/\underline{r_i}) = \frac{4j\,\omega\mu d}{\varphi_0} \sum_{m=1}^{\infty} \sum_{n=1}^{\infty} \frac{J_v(K_{vn}\,\rho)J_v(K_{vn}\,\rho_i)\sin(v\varphi)\sin(v\varphi_i)}{(K_{vn}^2 - K^2)(a^2 - \dfrac{v^2}{K_{vn}^2})J_v^2(K_{vn}a)}$$

$$(2.74)$$

2.6.2 Green's function for sector with one straight edge shorted

For the circular sector shown in the Fig. 2.10(c), the angular eigen functions which satisfy the boundary condition $V = 0$ at $\varphi = 0$, and $\dfrac{\partial V}{\partial n} = 0$ at $\varphi = \varphi_0$ are given as

$$\varphi_m = A_m \sin v\varphi, \qquad v = \frac{(m+\tfrac{1}{2})\pi}{\varphi_0} \qquad\qquad (2.75)$$

Since $\displaystyle\int_0^{\varphi_0} \sin^2\left[\frac{(m+\tfrac{1}{2})}{\varphi_0}\pi\right]\varphi \, d\varphi = \frac{\varphi_0}{2}$, for all values of m

$$(2.76)$$

the normalized eigen function can be written as

$$\varphi_m = \sqrt{\frac{2}{\varphi_0}} \sin v\varphi \qquad (2.77)$$

The radial eigen functions are same as that of the previous section. The Green's function can be written as

$$G(\underline{r}/\underline{r_i}) = \frac{4j\,\omega\mu d}{\varphi_0} \sum_{m=0}^{\infty} \sum_{m=1}^{\infty} \frac{J_v(K_{vn}\,\rho)J_v(K_{vn}\rho_i)\sin(v\varphi)\sin(v\varphi_i)}{(K_{vn}^2-K^2)(a^2-\frac{v^2}{K_{vn}^2})\,J_v^2(K_{vn}a)}$$

$$(2.78)$$

where

$$v = \frac{(m+\frac{1}{2})\pi}{\varphi_0}$$

2.6.3 Green's function for sector with the circular periphery shorted

The angular eigen functions which satisfy $\frac{\partial V}{\partial n} = 0$ at $\varphi = 0$ and φ_0 for the sector shown in the Fig. 2.10(d) are

$$\varphi_m = A_m \cos(v\varphi), \quad A_m = \sqrt{\frac{2}{\varphi_0}} \quad \text{for } m \neq 0,$$

$$= \frac{1}{\sqrt{\varphi_0}} \quad \text{for } m = 0 \qquad (2.79)$$

The radial eigen functions which satisfy $V = 0$ at $\rho = a$ are given as

$$R_n = B_n \, J_v(K'_{vn}\,\rho) \qquad (2.80)$$

where $K'_{vn} = \frac{p'_{vn}}{a}$, p'_{vn} is the nth zero of the Bessel function of the first kind and order v. The above eigen functions are normalized by setting

$$B_n = \frac{1}{[\int_0^a \rho J_v^2(K'_{vn}\rho)d\rho]^{\frac{1}{2}}} \qquad (2.81)$$

Using (2.34), B_n is obtained as

$$B_n = \frac{\sqrt{2}}{aJ_{v+1}(K'_{vn}a)} \qquad (2.82)$$

Then, using (2.34) the Green's function can be written as

$$G(\underline{r}/\underline{r_i}) = \frac{4j\,\omega\mu d}{\sigma\varphi_o a^2} \sum_{m=o}^{\infty} \sum_{n=1}^{\infty} \frac{J_v(K'_{vn}\rho)J_v(K'_{vn}\rho_i)\cos(v\varphi)\cos(v\varphi_i)}{(K_{vn}^2-K^2)\,J_{v+1}^2(K'_{vn}a)}$$

$$(2.83)$$

where

$$\sigma = \begin{cases} 2, & \text{for } m = 0 \\ 1, & \text{otherwise} \end{cases} \quad \text{and} \quad v = \frac{m\pi}{\varphi_o}$$

2.6.4 Green's function for sector with one radial wall and circular wall shorted

The normalized angular eigen functions for the sector shown in Fig. 2.10(e) are same as that of the sector discussed in the Section 2.6.2 and are given as

$$\varphi_m = \sqrt{\frac{2}{\varphi_o}} \sin v\varphi \qquad (2.84)$$

where

$$v = \frac{(m+\frac{1}{2})\pi}{\varphi_o}$$

The normalized radial eigen functions are same as that of the sector discussed in the Section 2.6.3 and are given as

$$R_n = \frac{\sqrt{2}}{aJ_{v+1}(K'_{vn}a)} \quad J_v(K'_{vn}\rho) \tag{2.85}$$

The Green's function using (2.34), can be written as

$$G(\underline{r}/\underline{r}_i) = \frac{4j\omega\mu d}{\varphi_o a^2} \sum_{m=0}^{\infty} \sum_{n=1}^{\infty} \frac{J_v(K'_{vn}\rho)J_v(K'_{vn}\rho_i)\sin(v\varphi)\sin(v\varphi_i)}{(K'^2_{vn}-K^2)\, J^2_{v+1}(K'_{vn}a)} \tag{2.86}$$

2.6.5 Green's function for sector with shorted boundary

The normalized angular eigen functions for the sector shown in Fig. 2.10(f) which satisfy the boundary conditions $V = 0$ at $\varphi = 0$, φ_o and at $\rho = a$

$$\varphi_m = \sqrt{\frac{2}{\varphi_o}} \sin v\varphi \tag{2.87}$$

The normalized radial eigen functions which satisfy $V = 0$ at $\rho = a$ are

$$R_n = \frac{\sqrt{2}}{aJ_{v+1}(K'_{vn}a)} \quad J_v(K'_{vn}\rho) \tag{2.88}$$

where $K'_{vn} = \dfrac{p'_{vn}}{a}$, p'_{vn} is the nth zero of the Bessel function of the first kind and order v.

Then, using (2.34), the Green's function for the sector with all electric walls is obtained as

$$G(\underline{r}/\underline{r}_i) = \frac{4j\omega\mu d}{\varphi_o a^2} \sum_{m=1}^{\infty} \sum_{n=1}^{\infty} \frac{J_v(K'_{vn}\rho)J_v(K'_{vn}\rho_i)\sin(v\varphi)\sin(v\varphi_i)}{(K'^2_{vn}-K^2)\, J^2_{v+1}(K'_{vn}a)} \tag{2.89}$$

2.7 DISCUSSION

Green's functions have been developed for mixed boundary 30°-60° right-angled triangles and circular sectors using the method of images and the method of expansion in series of eigen functions respectively. The Green's function has also been developed for shorted boundary equilateral triangle using the method of images.

In reducing the right-hand side of (2.18) to a periodic function, one of the factors obtained, viz., $T_1(x,y)$ in (2.42), $T_2(x,y)$ in (2.51) and $T_3(x,y)$ in (2.60), is the eigen function which satisfies the boundary conditions. Thus, this part of the procedure of the method of images may be used in evaluation of eigen functions in similar cases.

The Green's functions of the sectoral segments have been used for the analysis of sectoral microstrip antennas in Chapter Three.

CHAPTER THREE

MIXED BOUNDARY SEMICIRCULAR AND OPEN BOUNDARY 120°-SECTORAL MICROSTRIP ANTENNAS

Extensive work on open boundary rectangular, circular and semicircular microstrip antennas has been reported in the literature [17], [20], [21]. Various methods (already discussed in the Section 1.2.2) are available for analysing these antennas. The present investigation employs Green's function approach for analysing mixed boundary semicircular microstrip antennas and open boundary 120°-sectoral microstrip antenna. The coupling between mixed boundary microstrip antennas is expected to be less than the coupling between open boundary microstrip antennas. Therefore, the experimental study of coupling between two mixed boundary antennas has been considered. The details of the experimental investigations carried out on the coupling between two semicircular antennas with circular peripheries shorted, is given in this chapter. For the purpose of comparison coupling between open boundary semicircular antennas has also been done.

All the antennas are fabricated on copper cladded 1/8" thick polystyrene substrate of relative permittivity (ε_r) equal to 2.55.

3.1 GREEN'S FUNCTION APPROACH

3.1.1 Analysis using Green's function method

In this method, the given antenna structure is analyzed
in terms of a planar model with appropriate boundaries (i.e.
magnetic wall boundaries for open edges, electric wall
boundaries for shorted edges). The analysis procedure is
illustrated in Fig. 3.1. An open boundary semicircular
antenna is used for illustration purpose. The physical
magnetic wall boundary is extended outward to take into
account the effect of fringing fields around the magnetic
wall (open) edges.

The magnetic wall periphery of the planar circuit is
divided into smaller sections of finite widths, such that,
the field variation along each such section is negligibly
small and each section is considered as a port of the
multiport network. Byt knowing the Green's function of the
planar component, the impedance matrix $\underline{Z}$ of the multiport network
can be calculated from (2.27). The $\underline{Z}$ found as above is
the impedance matrix of the planar circuit acting as
resonator, i.e., an infinite impedance wall is assumed to be
connected at the open (or magnetic wall) boundaries. But,
in the case of planar elements acting as antennas, the open
boundaries of the components should be terminated by the
respective radiation resistances, i.e. the ports taken along
the magnetic (open) boundaries should be terminated by the
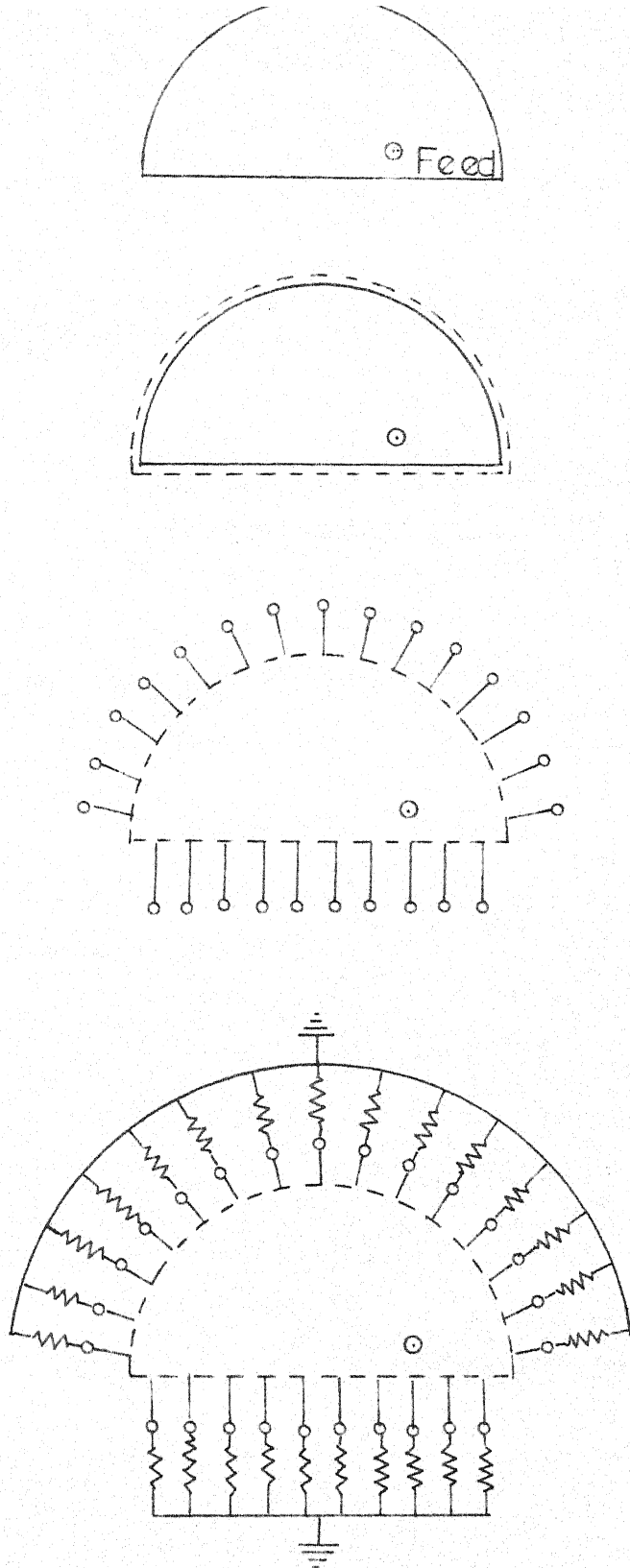
Antenna configuration

Planar model after extending the physical boundary

Equivalent multiport network

Loading by radiation resistance

Fig. 3·1 Procedure to analyze microstrip antennas by Green's function approach

resistances. The values of the radiation resistances which
terminate the ports are calculated as follows : (i) the
radiation resistance for each of the magnetic walls is
calculated, (ii) this radiation resistance is distributed
among all the ports taken along that magnetic wall, the
values being proportional to the port widths, and the
resistances thus obtained are assumed to be connected
at the mid-points of the respective ports. An expression
for finding the Z-matrix or the input impedance at any
feed point location of the multiport network thus obtained
(i.e. the Z-matrix of the microstrip circuit acting as
antenna) has been developed in the literature [22] and is
discussed in the following section.

3.1.2 Evaluation of input impedance

The network model of an open-boundary semicircular
antenna is shown in Fig. 3.2. The port numbers of this
network model are labelled in this figure. Let 'p' be the
number of ports taken inside/or along the edges of the
planar element at which the input impedances are to be found.
These p-ports are called as external ports. Let 'q' be the
total number of ports taken along the open edges of the
planar element. An equal number of 'r' ports are taken.
These ports are terminated by the resistances, which are
calculated as explained in the previous section. The ports
'q' and 'r' are interconnected such that
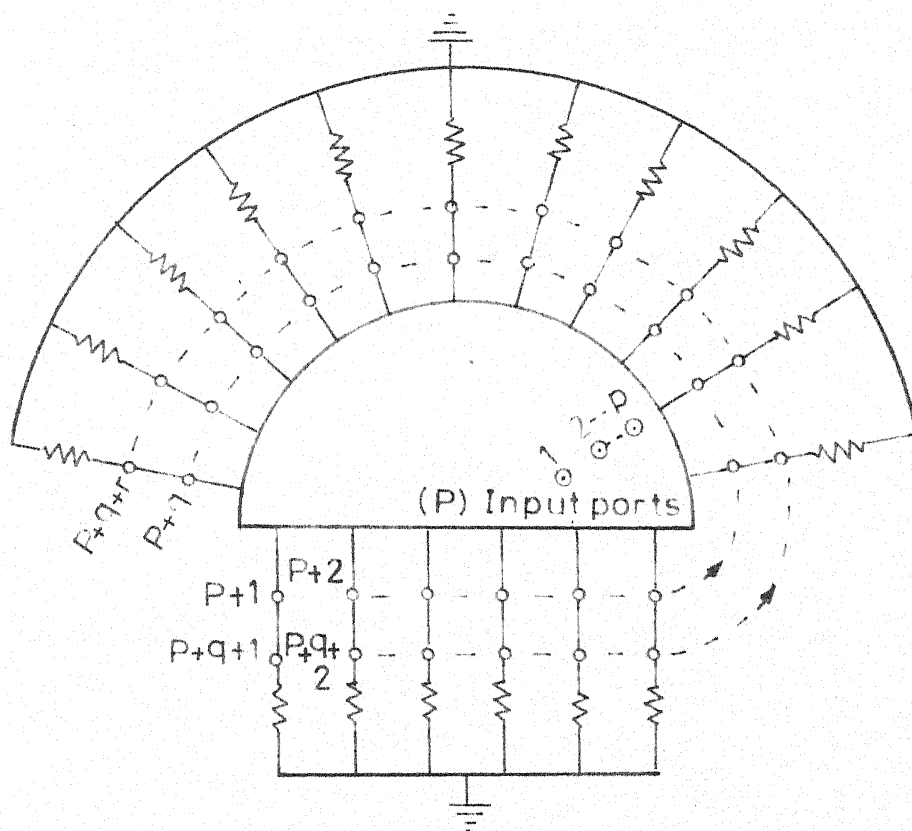
Fig. 3·2 Multiport network model of the antenna shown in Fig. 3·1

$$\underline{V}_q = \underline{V}_r \tag{3.1}$$

and

$$\underline{i}_q + \underline{i}_r = \underline{0}$$

The Z-matrix of the above network model can now be written as

$$\begin{bmatrix} \underline{V}_p \\ \underline{V}_q \\ \underline{V}_r \end{bmatrix} = \begin{bmatrix} \underline{Z}_{pp} & \underline{Z}_{pq} & \underline{Z}_{pr} \\ \underline{Z}_{qp} & \underline{Z}_{qq} & \underline{Z}_{qr} \\ \underline{Z}_{rp} & \underline{Z}_{rq} & \underline{Z}_{rr} \end{bmatrix} \begin{bmatrix} \underline{i}_p \\ \underline{i}_q \\ \underline{i}_r \end{bmatrix} \tag{3.2}$$

Substituting (3.1) into (3.2) and eliminating $\underline{V}_p$, $\underline{V}_q$ and $\underline{i}_r$,

$$(\underline{Z}_{qq} - \underline{Z}_{qr} - \underline{Z}_{rq} + \underline{Z}_{rr})\underline{i}_q = (\underline{Z}_{rp} - \underline{Z}_{qp})\underline{i}_p \tag{3.3}$$

or

$$\underline{i}_q = (\underline{Z}_{qq} - \underline{Z}_{qr} - \underline{Z}_{rq} + \underline{Z}_{rr})^{-1} (\underline{Z}_{rp} - \underline{Z}_{qp})\underline{i}_p \tag{3.4}$$

Substituting (3.4) into the first equation of (3.2) and using $\underline{i}_r = -\underline{i}_q$, the $\underline{Z}$-matrix of the overall network is obtained as

$$\underline{Z}_p = \underline{Z}_{pp} + (\underline{Z}_{pq} - \underline{Z}_{pr})(\underline{Z}_{qq} - \underline{Z}_{qr} - \underline{Z}_{rq} + \underline{Z}_{rr})^{-1} (\underline{Z}_{rp} - \underline{Z}_{qp}) \tag{3.5}$$

The relation between $\underline{V}_q$ and $\underline{i}_p$, obtained by substituting (3.4) into the second equation of (3.2), is given as

$$\underline{V}_q = [\underline{Z}_{qp} + (\underline{Z}_{qq} - \underline{Z}_{qr})(\underline{Z}_{qq} - \underline{Z}_{qr} - \underline{Z}_{rq} + \underline{Z}_{rr})^{-1} (\underline{Z}_{rp} - \underline{Z}_{qp})]\underline{i}_p$$
$$\tag{3.6}$$

The diagonal elements of $\underline{Z}_p$ give the input impedances at 'p' ports of the planar antenna. The unknowns on the right hand side of the equation (3.5) are calculated as follows : $\underline{Z}_{pp}$, $\underline{Z}_{pq}$, $\underline{Z}_{qp}$ and $\underline{Z}_{qq}$ are calculated using (2.27). When the losses in the conducting plane and in the dielectric substrate are ignored, the elements of the above 4 matrices are purely reactive. But, these are computed assuming them as real to save the computer time. In $\underline{Z}_{rr}$, only the diagonal elements are non-zero and these are equal to the resistance values terminated at the respective ports. $\underline{Z}_{pr}$, $\underline{Z}_{qr}$, $\underline{Z}_{rq}$ and $\underline{Z}_{rp}$ are null matrices.

The method discussed above can also be applied to analyze the irregular shaped antennas, whose Green's functions are not known and which can be considered as combination of simple shapes. This is known as <u>segmentation</u> method.

3.1.3 <u>Radiation pattern calculations</u>

The far fields due to the radiation from the surrounding slots (open boundaries) of a planar antenna can be calculated by considering these slots as the magnetic current sheets.

If the dielectric material is isotropic, homogeneous and lossless, and the conductivities of the microstrip conductor and the ground plane are infinite, the surface magnetic currents can be written in terms of tangential electric field $(\bar{E})$ as

$$\overline{M} = -\hat{n} \times \overline{E} \tag{3.7}$$

where $\hat{n}$ is a unit vector normal to the surface.

The electric and magnetic fields at any point $p(r, \theta, \varphi)$ outside the antenna may then be written as

$$\overline{E}(r) = -\frac{1}{\varepsilon} \nabla \times \overline{F} \tag{3.8}$$

$$\overline{H}(r) = -j\omega\overline{F} \tag{3.9}$$

where ε is the permittivity, ω is the angular frequency and $\overline{F}$ is the vector electric potential given by

$$\overline{F} = \frac{\varepsilon}{4\pi} \iint_S \overline{M}(r') \frac{e^{-jk_0|\overline{r}-\overline{r}'|}}{|\overline{r}-\overline{r}'|} ds' \tag{3.10}$$

where k_0 is a free space wave number and $\overline{M}(r')$ is the surface magnetic current density at a point r' from the origin as shown in Fig. 3.3(a). For simplicity, the time dependence $e^{j\omega t}$ of all fields and currents has been dropped. The only significant field components in the far field are those transverse to the direction of propagation. The field $\overline{E}$ can be written in term of $\overline{H}$ as

$$\overline{E}(r) = \eta_0 \overline{H}(r) \tag{3.11}$$

where η_0 is the free space impedance (120π ohms). Since $r \gg r'$, the field $\overline{H}(r)$ can be written as

s

r_0

P(Field point)

r'

r

ψ

Origin

(a)

z

P(r, θ, ϕ)

r

r_0

θ

y

a

ϕ'

$\rho\, d\rho\, d\phi'$

ϕ

X

(b)

$(r \sin\theta,\ 90°,\ \phi)$
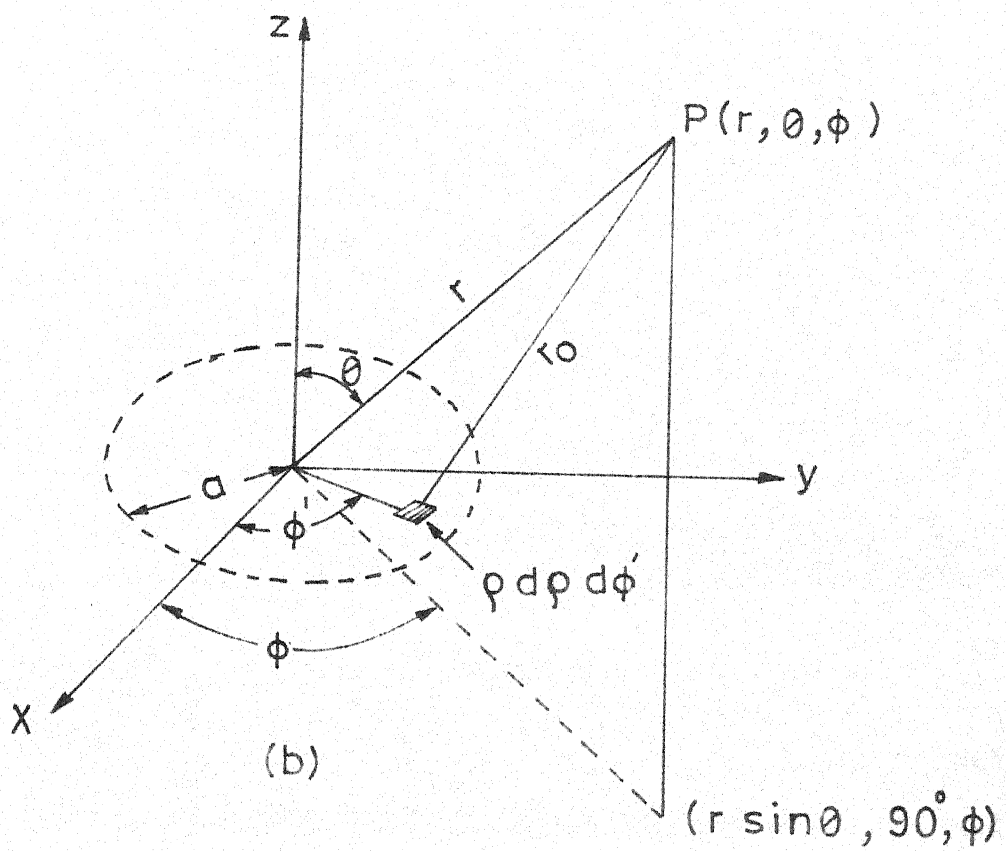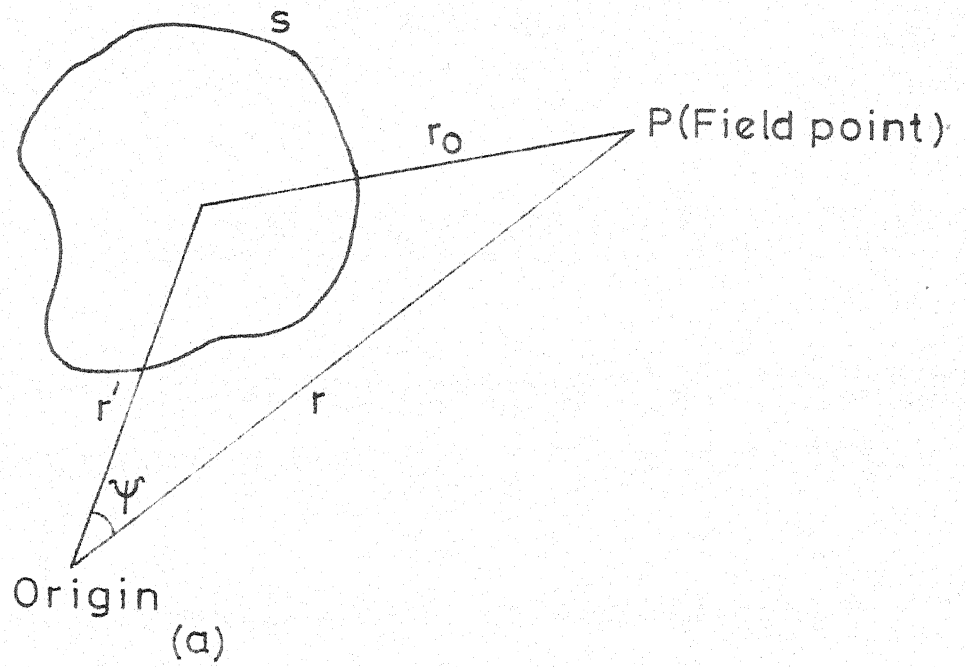
Fig. 3.3 Co-ordinate system

$$\overline{H}(r) = - \frac{j\omega\varepsilon}{4\pi} \frac{\varepsilon}{r} e^{-jk_o r} \iint_s \overline{M}(r') e^{jk_o r'\cos\psi} ds'$$

(3.12)

where ψ is the angle between the r and r' directions.

3.1.4 Far field of a circular source

Consider a planar circular circuit with coordinate systems as shown in Fig. 3.3(b). The far-zone vector electric potential is

$$\overline{F} = \frac{\varepsilon e^{-jk_o r}}{4\pi r} \int_0^{2\pi} \int_0^d \overline{M}(\rho,\varphi') e^{jk_o \rho \sin\theta \cos(\varphi'-\varphi)} a \, d\varphi' dz$$

(3.13)

where a is the radius of the circle, d is the height of the substrate, (r,θ,φ) are the spherical coordinates and (ρ,φ',Z) is the cylindrical coordinates. Since $\overline{M} = -\hat{n}\times\overline{E}$, where $\hat{n}$ is a unit vector normal to the magnetic current sheet (in ρ direction) and E has only E_z component (which is assumed to be constant along Z direction), the expression (3.13) can be rewritten as

$$\overline{F} = \frac{\varepsilon}{4\pi} \frac{e^{-jk_o r}}{r} \, ad \int_0^{2\pi} \overline{M}_{\varphi'}(\rho,\varphi') e^{jk_o \rho \sin\theta \cos(\varphi'-\varphi)} d\varphi'$$

(3.14)

For any vector $\overline{T}$, the transformation from the cylindrical to the spherical coordinates may be obtained from the matrix:

$$
\begin{bmatrix} T_r \\ T_\Theta \\ T_\varphi \end{bmatrix} = \begin{bmatrix} \sin\Theta \cos(\varphi'-\varphi) & -\sin\Theta \sin(\varphi'-\varphi) & \cos\Theta \\ \cos\Theta \cos(\varphi'-\varphi) & -\cos\Theta \sin(\varphi'-\varphi) & \sin\Theta \\ \sin(\varphi'-\varphi) & \cos(\varphi'-\varphi) & 0 \end{bmatrix} \begin{bmatrix} T_\rho \\ T_{\varphi'} \\ T_z \end{bmatrix} \quad (3.15)
$$

Therefore, using (3.14) and (3.15), the components for the magnetic field may be written as

$$
H_\Theta = -j\,\omega F_\Theta \tag{3.16}
$$

$$
H_\varphi = -j\,\omega F_\varphi \tag{3.17}
$$

where

$$
F_\Theta = \frac{\varepsilon}{4\pi}\,\frac{e^{-jk_o r}}{r}\,da(-\cos\Theta\,\sin(\varphi'-\varphi))\int_0^{2\pi} \overline{M}_{\varphi'}(\rho,\varphi')\,\cdot
$$
$$
e^{jk_o \rho \sin\Theta \cos(\varphi'-\varphi)}\,d\varphi' \tag{3.18}
$$

and

$$
F_\varphi = \frac{\varepsilon}{4\pi}\,\frac{e^{-jk_o r}}{r}\,da\,\cos(\varphi'-\varphi)\int_0^{2\pi} \overline{M}_{\varphi'}(\rho,\varphi')\,\cdot
$$
$$
e^{jk_o \rho \sin\Theta \cos(\varphi'-\varphi)}\,d\varphi' \tag{3.19}
$$

Then, the electric field components are calculated as follows :

$$
E_\Theta = \eta_o H_\varphi \tag{3.20}
$$

$$
E_\varphi = \eta_o H_\Theta \tag{3.21}
$$

where η_o is the free space impedance.

3.2   SEMICIRCULAR MICROSTRIP ANTENNA WITH STRAIGHT EDGE AS ELECTRIC WALL

3.2.1   Theoretical considerations

The semicircular microstrip antenna with straight edge as electric wall is shown in Fig. 3.4(a). It can be modelled as a cylindrical cavity, bounded on its top, bottom and straight edge by electric walls and circular periphery by a magnetic wall. The eigen functions which satisfy the boundary condition $\frac{\partial V}{\partial n} = 0$ on the circular periphery, $V = 0$ on the straight edge can be written as

$$\psi_{mn} = J_m(K_{mn} \, \rho) \, \sin(m \, \varphi) \qquad (3.22)$$

where $K_{mn} = \frac{P_{mn}}{a}$, P_{mn} is the nth zero of the derivative of the Bessel function of the first kind, of order m. At $\rho = a$, $J_m(K_{mn} \, \rho)$ is maximum. Some of the roots of

$$J_m(K_{mn} \, a) = 0 \qquad (3.23)$$

are given in Table I.

Table   I

mode (m,n)	(0,1)	(1,1)	(2,1)	(0,2)	(3,1)
Root (K_{mn} a)	0	1.84118	3.05424	3.83171	4.20119

(a)

(b)

(c)

p-ports

$R = 14 \times R_r$

a_e
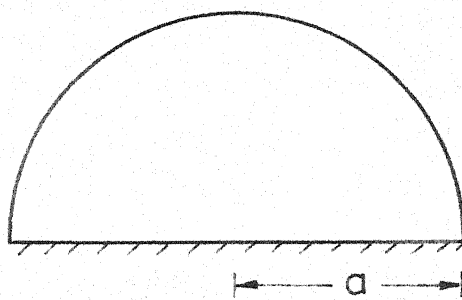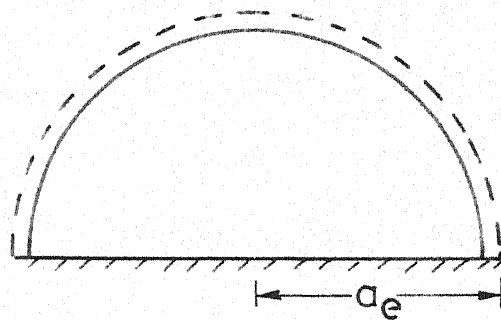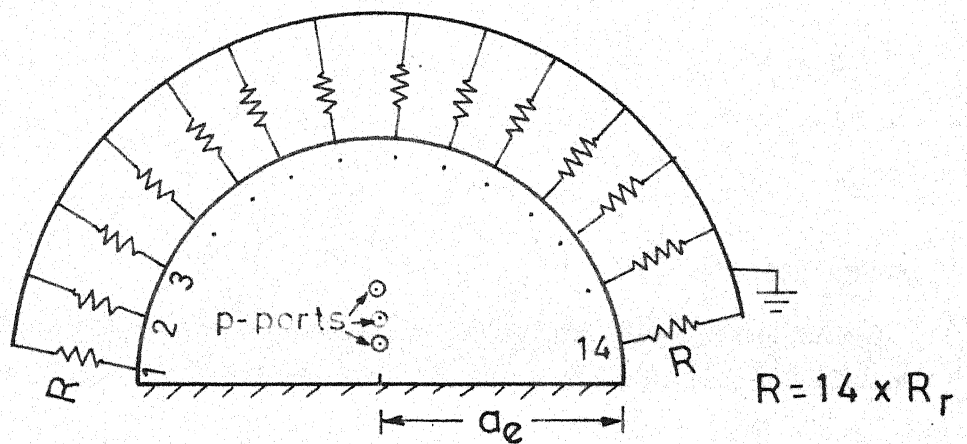
Fig. 3·4 (a) Semicircular antenna with straight edge shorted, (b) its planar model, (c) its equivalent multiport network

The smallest root is 1.84118. This corresponds to (1,1) mode. The Green's function for the semicircular planar circuit with straight edge as the electric wall shown in Fig. 3.4(a) can be obtained by substituting $\varphi_0 = \pi$, $v = \dfrac{m\pi}{\varphi_0} = m$ in (2.74) and multiplying it by 2(for a microstrip circuit, the impedance is two times that of a stripline circuit) and is written as

$$G(\ r/r_i) = 2 \cdot \frac{4j\omega\mu d}{\pi} \sum_{m=1}^{\infty} \sum_{n=1}^{\infty} \frac{J_m(K_{mn}\rho)J_m(K_{mn}\rho_i)\sin(m\varphi)\sin(m\varphi_i)}{(K_{mn}^2 - K^2)(a^2 - \frac{m^2}{K_{mn}^2})J_m^2(K_{mn}a)}$$

(3.24)

The resonant frequency is obtained by equating $(K_{mn}^2 - K^2)$ to zero, i.e.

$$K_{mn}^2 = K^2$$

(3.25)

Substituting $K_{mn} = \dfrac{P_{mn}}{a}$ and $K^2 = \omega^2\mu\varepsilon$ in (3.25), we get

$$f_r = \frac{P_{mn} \times 3 \times 10^{18}}{2\pi a_e\sqrt{\varepsilon_r}}$$

(3.26)

An effective radius a_e has been introduced [11] in the above equation to account for the fringing fields along the open edge :

$$a_e = a[1 + \frac{2d}{\pi a\varepsilon_r}(\ln(\frac{\pi a}{2d}) + 1.7726)]^{\frac{1}{2}}$$

(3.27)

For a given resonant frequency, the radius of the semi-circular antenna is the smallest for $P_{mn} = 1.84118$, i.e. for

(1,1) mode. Therefore, (1,1) mode is called as the dominant
mode.

3.2.2 Optimization of feed-point

The effective radius a_c for a frequency of 1 GHz (and
$p_{mn} = 1.84118$, $\varepsilon_r = 2.55$) calculated from (3.26) is 5.5 cms.
The planar model of the antenna (after extending the physical
boundary outwards) is shown in Fig. 3.4(b). The actual
radius a is calculated from (3.27) and is equal to 5.31 cms.
Since the Green's function method is employed to analyze the
antenna, the circular periphery of the antenna circuit shown
in Fig. 3.4(b) is divided into smaller sections of finite
widths. The widths of these sections are taken such that,
the field remains almost constant along each section and
these are considered as ports. A few feed-ports are taken.
The impedance matrix of the multiport network (planar circuit
acting as resonator) thus obtained is derived using (2.27)
and (3.24) and is written as

$$Z_{ij} = \sum_{m=1}^{\infty} \sum_{n=1}^{\infty} \frac{4j\,\omega\mu d\left[\dfrac{\sin(\frac{mW_i}{2a})}{(\frac{mW_i}{2a})}\right]\left[\dfrac{\sin(\frac{mW_j}{2a})}{(\frac{mW_j}{2a})}\right]\sin(m\theta_i)\,\sin(m\theta_j)}{\pi(K_{mn}^2-K^2)(a^2-m^2/K_{mn}^2)}$$

$$(3.28)$$

The need of external matching networks for matching the
input impedance of the antenna to the connecting cables is

avoided by locating a 50 Ohms point on the antenna using
the Green's function method discussed in Section 3.1.2.
This is done as follows : Fourteen q-ports are taken along
the circular edge of the antenna. An equal number of r-ports
are taken. These are terminated by resistances to account
for the radiated power. The formula for calculating the
radiation resistance of the circular edge of the antenna is
given in [11] and is written as

$$R_r = \frac{2 \times 960}{(ak_o)^2 I_1} \qquad (3.29)$$

where

$$I_1 = \int_0^\pi \{[J_{m+1}(k_o a \sin\theta) - J_{m-1}(k_o a \sin\theta)]^2 +$$

$$\cos^2\theta [J_{m+1}(k_o a \sin\theta) + J_{m-1}(k_o a \sin\theta)]^2 \} \sin\theta \ d\theta$$

$$\qquad (3.30)$$

$$k_o = \omega \sqrt{\mu_o \varepsilon_o}$$

$m = 1$ for the fundamental mode. Thus the resistances which
terminate the r-ports are given by multiplying R_r by 14, the
total number of ports. The equivalent multiport network is
shown in Fig. 3.4(c).

The voltage distributions for (1,1) mode and other
first few modes are shown in Fig. 3.5. It is seen that
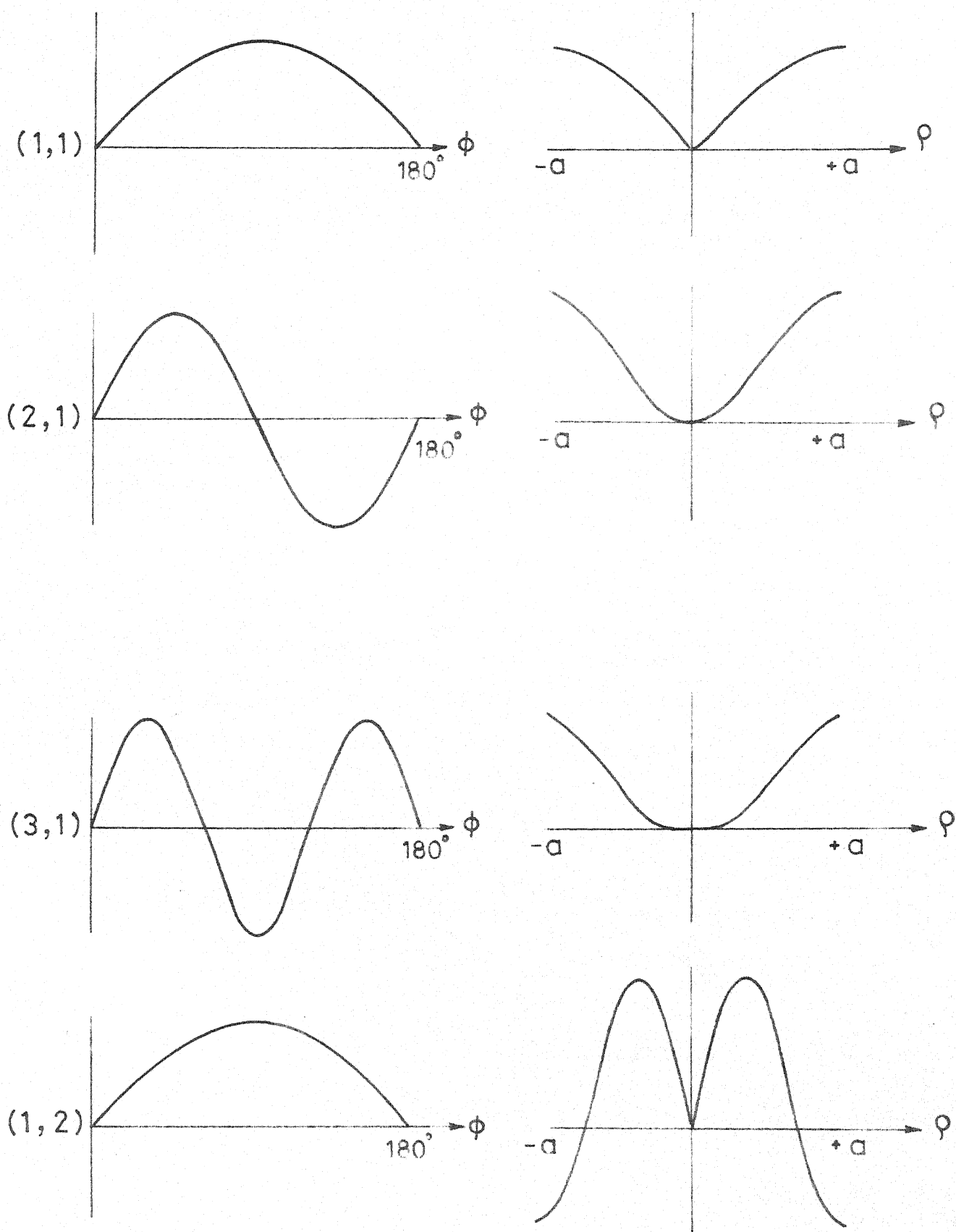the voltage for (1,1) mode is zero at the centre and maximum

Fig.3·5 Voltage distribution for different resonent modes of semicircular microstrip antenna with straight edge shorted

at ρ = a. Hence, the resistance will be very high at the edge and zero at the centre. Since the radiation resistance is of the order of 900 Ohms, it is expected that the 50 Ohms point is somewhere near the centre. The feed-point is considered along φ = 90°, so that the even-modes (i.e. (o,n), (2,n), ...,) are not excited, thus minimising the effect of higher-order modes. In the analysis, 20 higher-order odd modes which are close to the fundamental mode are considered. The formula for calculating the roots of these modes is given in Appendix A. Three external ports (p = 3) are taken. The input impedances at these ports are calculated using (3.5), (3.28) and (3.29). The width of these p-ports are taken equal to the diameter (0.12 cm) of the inner conductor of the co-axial connectors. The 50 Ohms feed-point is obtained at ρ_i = 5.8 mm.

3.2.3 Input impedance

At resonance, the input impedance at the feed-point (ρ_i = 5.8 mm) is 50 Ohms. The theoretical and experimental input impedance loci for 50 Ohms feed-point are given in the Figs. 3.6(a) and (b) respectively. The experimental resonant frequency is 999.5 MHz, which is 0.5 MHz less than the theoretical frequency. This may be attributed to the following reasons : i) The expression (3.27), which is used to find the effective radius is not very correct, and the error involved may be upto 2.5 percent, ii) The conductor, and dielectric
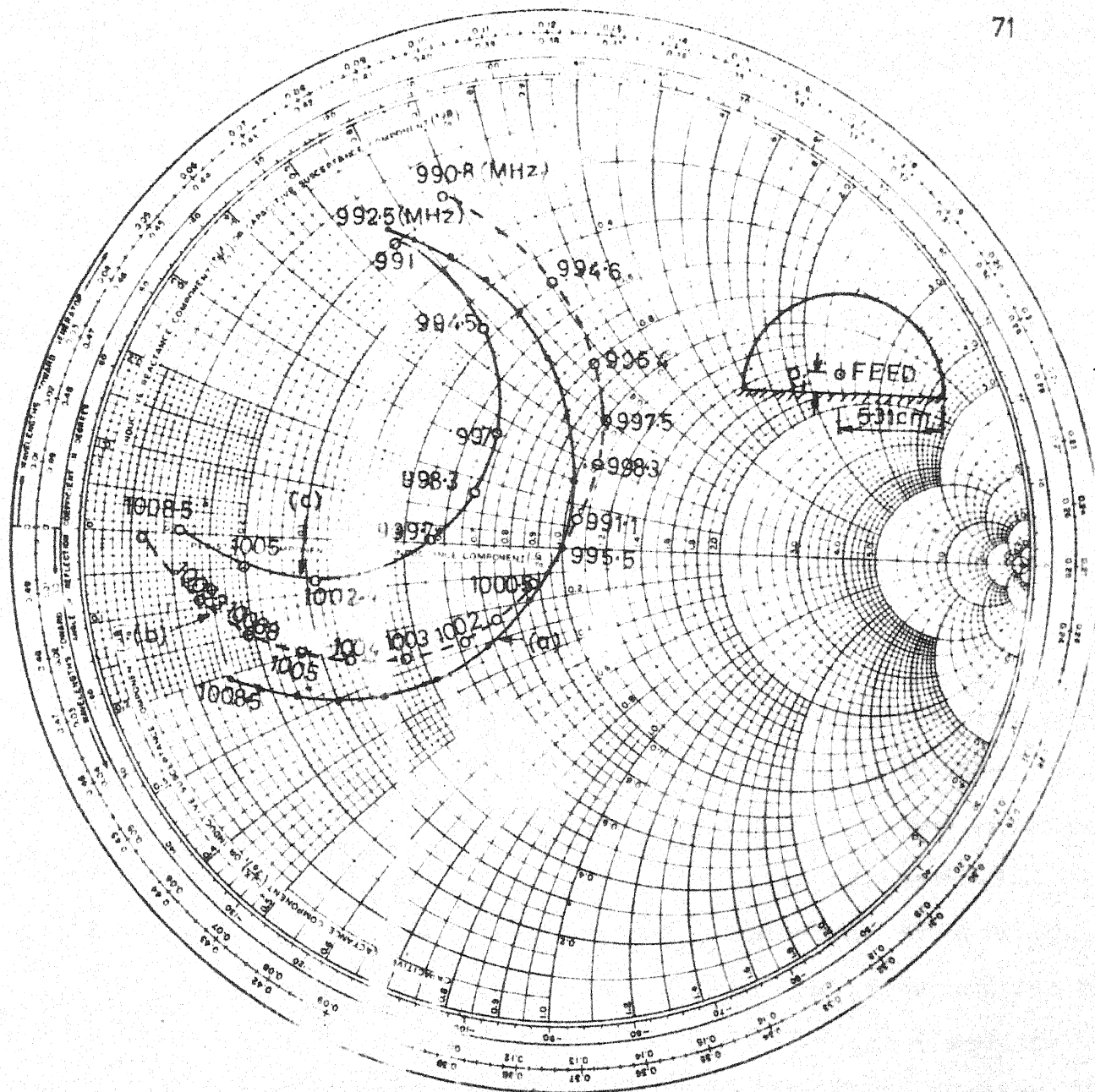
Fig. 3.6 Input impedance characteristics of semicircular
microstrip antenna with straight edge as electric
wall (a) Theoretical curve for δ_1 = 5.8 mm (Each
point on this curve represents an increase in
frequency of 10 MHz from previous point) (b) Experi-
mental curve for δ_1 = 5.8 mm (c) Experimental
curve for δ_1 = 5.1 mm

losses are not considered in the analysis. The input impedance versus frequency plot is a circle. The discrepancy between the theoretical and experimental impedance loci (Figs. 3.6(a) and (b)) may be due to the inaccuracy of the **meters**, and series inductance reactance associated with the connecting probe. The input impedance increases if the feed-point is shifted upwards and decreases if the feedpoint is shifted downwards. This may be observed from Fig. 3.6(c) which is the impedance locus for the feed-point taken at $\rho_i = 5.1$ mm.

3.2.4 Bandwidth

Depending on the system objectives, the bandwidth of an antenna is limited either by its radiation or input VSWR characteristics. In case of microstrip antennas, the resonant behaviour causes the bandwidth to be limited by input VSWR, and it may be defined as the frequency range for which VSWR remains less than two. The input VSWR at any frequency can be calculated by knowing the input impedance at that frequency and the characteristic impedance (50 Ohms). The variation of input VSWR with frequency is shown in the Fig. 3.7. The theoretical bandwidth is 5.1 MHz. The experimental bandwidth is 5.15 MHz. There is a close agreement between the theoretical and experimental bandwidths. The bandwidth is of the order of 0.5 percent of the resonant frequency.
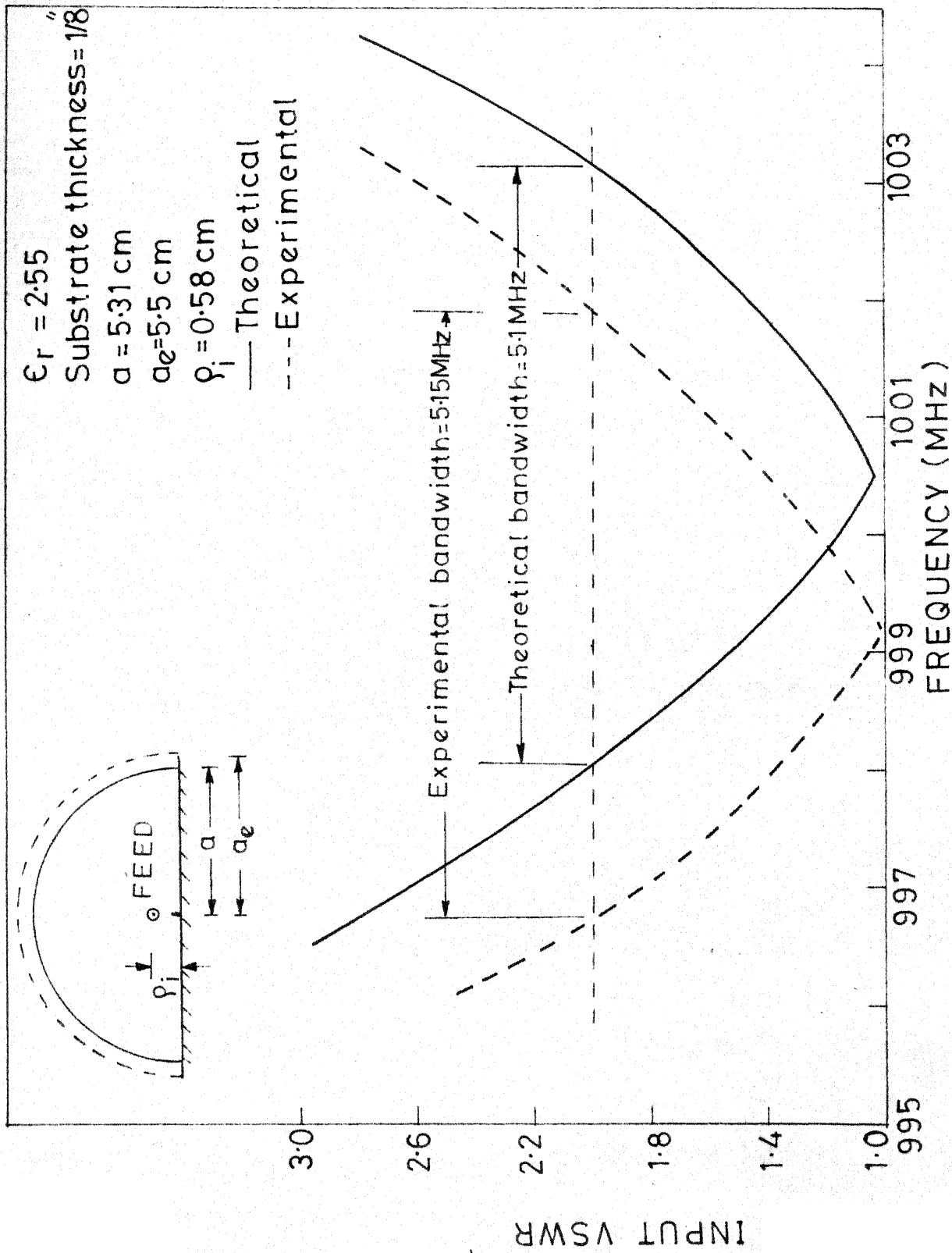
Fig.3.7 Variation of input VSWR with frequency

The bandwidth of a circular disk antenna at 1 GHz centre frequency is of the order 0.9 percent [11]. The reduction in the bandwidth may be explained as follows : The radiation resistance of the semicircular antenna with straight edge shorted is more than that of the circular disc, and hence the Q-factor is more. Since the bandwidth is inversely proportional to the Q-factor, the bandwidth of the semicircular antenna with straight edge shorted is less than that of the circular disk antenna.

3.2.5 Radiation characteristics

The radiation pattern of the antenna shown in Fig. 3.4(a) is calculated in $\varphi = 0$ and $\varphi = 90^\circ$ planes using the procedure described in the Sections 3.1.3 and 3.1.4. It is noted that only E_φ component of the radiation field is present in $\varphi = 0^\circ$ plane, and only E_θ component is present in $\varphi = 90^\circ$ plane. These are plotted in Figs. 3.8(a) and (b) respectively. The 3 dB beamwidth in $\varphi = 0^\circ$ plane is approximately 92°.

The measured radiation patterns in both $\varphi = 0^\circ$ and $\varphi = 90^\circ$ are given in the Figs. 3.8(a) and (b) (dashed lines) respectively. There is a discrepancy between the theoretical and experimental patterns near $\theta = 90^\circ$. This is due to finite ground plane of the antenna (in the analysis, it is considered to be very large, ideally infinite) and excitation of surface waves. The experimental 3-dB beamwidths in $\varphi = 0^\circ$ and $\varphi = 90^\circ$ planes are 110° and 135° respectively.
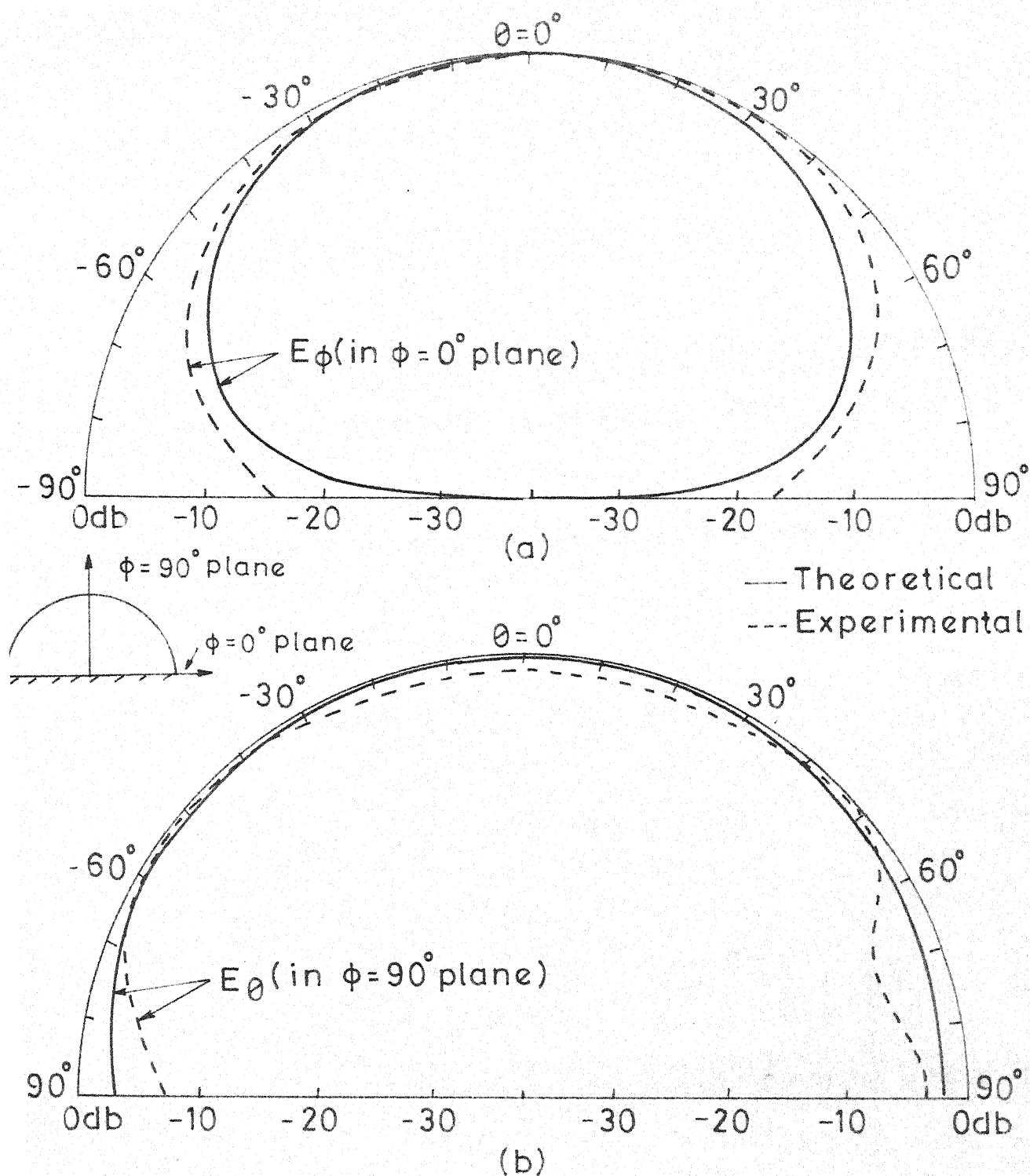
Fig. 3·8 Theoretical and experimental radiation patterns (a) E_ϕ in $\phi = 0°$ plane (b) E_θ in $\phi = 90°$ plane of the antenna shown in Fig. 3·4 (a)

3.3 OPEN BOUNDARY SEMICIRCULAR MICROSTRIP ANTENNA

Even though an open boundary microstrip antenna has been analyzed for its radiation characteristics and input impedance [11],[21] the general formulas for finding the bandwidth and the feed-point are not available. For comparison purpose, the experimental study (of bandwidth and feed-point) of this antenna has been done. Also, an idea of location of 50 ohms feed-point is necessary to study the coupling between two open boundary semicircular microstrip antennas for different spacings.

3.3.1 Theoretical considerations

The eigen functions which satisfy the boundary condition $\frac{\partial V}{\partial n} = 0$ on the circular periphery and straight edge can be written as

$$\psi_{mn} = J_m(K_{mn} \rho) \cos(m\varphi) \tag{3.31}$$

(K_{mn} is defined in Section 3.2.1).

The Green's function obtained from (2.66) by substituting $\varphi_0 = \pi$, $v = m$ and multiplying (2.66) by 2 is

$$G(r/r_i) = \frac{4d}{j\omega\varepsilon\pi a^2} + \frac{4j\omega\mu d}{\pi} \sum_{m=0}^{\infty} \sum_{n=1}^{\infty} \cdot$$

$$\frac{\sigma J_m(K_{mn} \rho_i) J_m(K_{mn} \rho)\cos(m\varphi)\cos(m\varphi_i)}{(a^2 - \frac{m^2}{K_{mn}^2})(K_{mn}^2 - K^2) J_m^2(K_{mn}a)} \tag{3.32}$$

where a is the radius of the antenna and

$$\sigma = \begin{cases} 1, & \text{if } m = 0 \\ 2, & \text{if } m > 0 \end{cases}$$

Since the radial eigen functions are same as that discussed in Section 3.2, (1,1) mode is the dominant mode for the open boundary semicircular antenna.

3.3.2 Optimization of feed-point

The effective radius for a frequency of 3.154 GHz (and p_{mn} = 1.84118, ε_r = 2.55) calculated from (3.26) is 1.745 cms. The actual radius a calculated from (3.27) is 1.6 cms.

The 50 ohms feed-point is somewhere near the centre for the dominant mode. This is clear from the Fig. 3.5. The feed-point cannot be taken along $\varphi = 90^\circ$ for the excitation of the dominant mode. This is clear from (3.32). The feed-point is taken along $\varphi = 0^\circ$. By doing experimental iterations, the exact 50 ohms feed-point is obtained and it is at a distance of 0.29 cms from the centre.

3.3.3 Bandwidth

The (experimental) variation of input VSWR with frequency is is plotted in Fig. 3.9. The bandwidth obtained is 99 MHz, which is 3.13 percent of the experimental resonant frequency (3159 MHz). The bandwidth of an open boundary circular micro-strip antenna for the same centre frequency is approximately
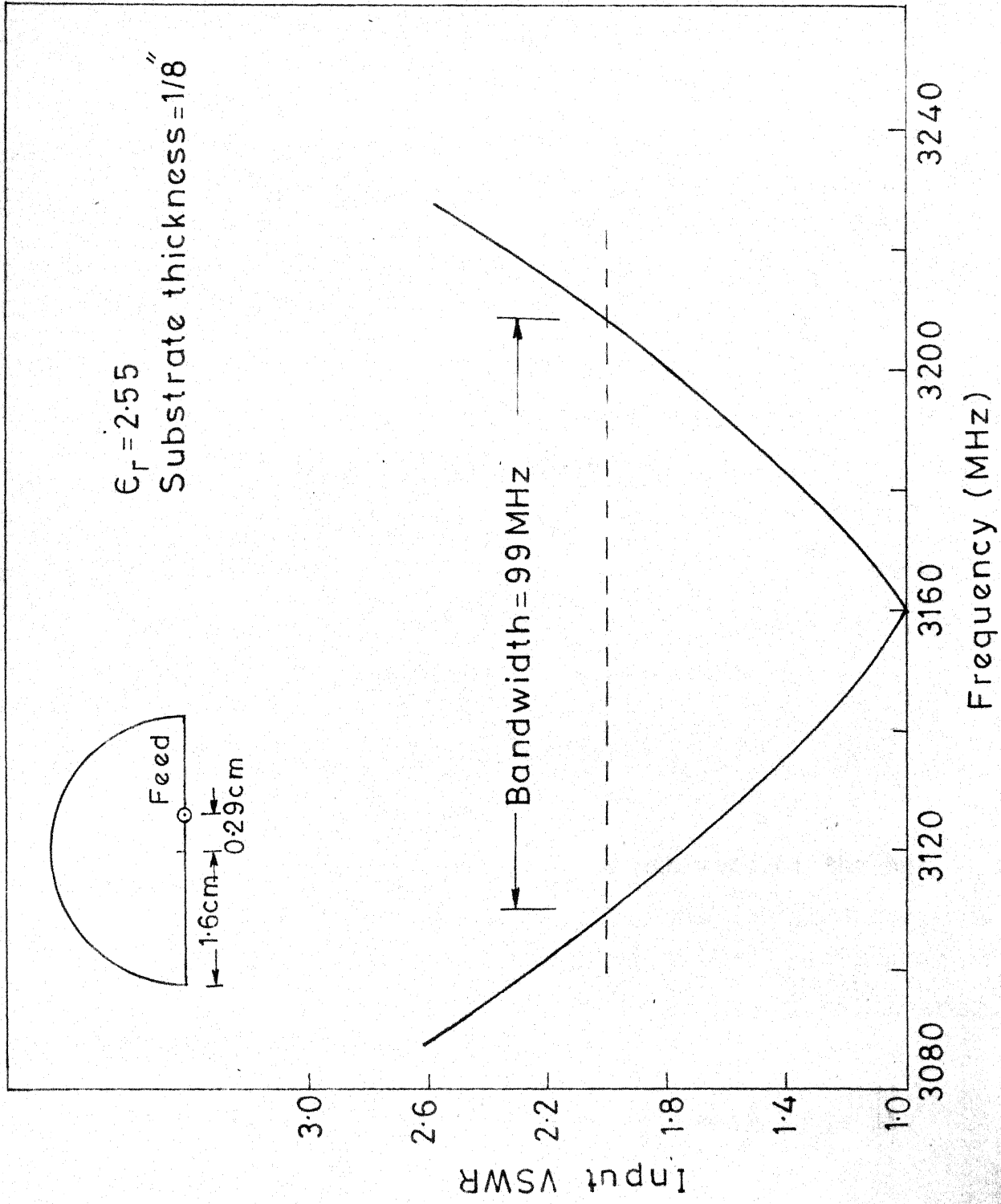
Fig.3.9 Experimental variation of input VSWR with frequency for open boundary semicircular microstrip antenna

3 percent. The ratio of the lengths of the radiating edges of open boundary circular microstrip antenna and open boundary semicircular microstrip antenna is 1.22. All these facts show that the straight edges radiate more as compared to the circular edges.

3.4 SEMICIRCULAR MICROSTRIP ANTENNA WITH CIRCULAR PERIPHERY SHORTED

3.4.1 Theoretical considerations

The semicircular antenna with circular periphery shorted is shown in Fig. 3.10(a). It can be modelled as a cylindrical cavity, bounded on its top, bottom and the circular periphery by electric walls and its straight edge by a magnetic wall. The eigen functions which satisfy the boundary conditions $\frac{\partial V}{\partial n} = 0$ at $\varphi = 0^{\circ}$ and $\varphi = 180^{\circ}$, and $V = 0$ on the circular periphery can be written as

$$\psi_{mn} = J_m(K'_{mn}\,\rho)\,\cos(m\varphi) \tag{3.38}$$
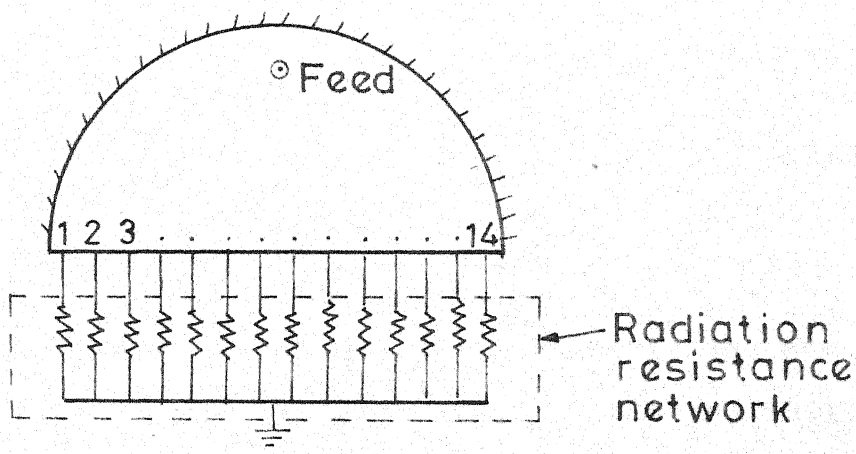
where
$$K'_{mn} = \frac{P'_{mn}}{a}\,,\quad P'_{mn}$$ is the nth zero of the Bessel function of the first kind, of order m and a is the radius of the antenna. At $\rho = a$,

$$J_m(K'_{mn}\,\rho.) = 0$$

Some of the roots of (3.32) are given in Table II.
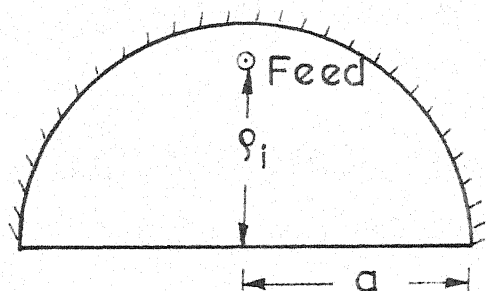
(a)

(b)

Fig.3·10 (a) Semicircular antenna with circular periphery shorted (b) its equivalent multiport network

Table II

mode (m,n)	(0,1)	(1,1)	(2,1)	(0,2)	(3,1)
Root $(K'_{mn} a)$	2.405	3.832	5.135	5.52	6.379

The smallest root is 2.405, which corresponds to (0,1) mode. The resonant frequency for any mode can be calculated from

$$f_r = \frac{P'_{mn} \times c}{2\pi a \sqrt{\varepsilon_r}} \qquad (3.35)$$

where c is the velocity of light in free space.

For a given resonant frequency, the radius is the smallest for $P'_{mn} = 2.405$, i.e. for (0,1) mode. Therefore, (0,1) is the dominant mode for the antenna configuration shown in the Fig. 3.10(a). The Green's function obtained from (2.83) is

$$G(r/r_i) = \frac{8j \omega \mu d}{\sigma \pi a^2} \sum_{m=0}^{\infty} \sum_{n=1}^{\infty} \frac{J_m(K'_{mn} \rho) J_m(K'_{mn} \rho_i) \cos(m\varphi) \cos(m\varphi_i)}{(K'^2_{mn} - K^2) J^2_{m+1}(K'_{mn} a)}$$

$$(3.36)$$

where $\sigma = \begin{cases} 2, & \text{for } m = 0 \\ 1, & \text{otherwise.} \end{cases}$

The impedance matrix $\underline{Z}_{ij}$ for the equivalent multiport
network model of the planar circuit shown in the Fig.
3.10(a), can be calculated from (2.27). (It does not
take into account the radiation, conductor and dielectric
losses).

3.4.2 Optimization of feed-point

The Green's function approach discussed in Section 3.1
is used for analysis. The total number of ports taken along
the straight edge of the antenna is 14 i.e., q = 14 (by
taking more number of ports, the accuracy can be increased,
but the computation time increases). The resistances to be
terminated at these 14 ports to account for the radiated
power are calculated using the formula

$$R = 14 \times R_r \qquad\qquad (3.37)$$

where R_r is the radiation resistance of the straight edge
of antenna which is calculated using the radiation resistance
formula of a rectangular antenna [24]. The equivalent network
model is shown in Fig. 3.10(b). 50 Ohms coaxial cables are
used for measurements. The use of any external impedance
matching network is avoided by locating a 50 Ohms feed-point
on the antenna. The selection of feed-point is explained
below.

The voltage distribution for the dominant mode (i.e.
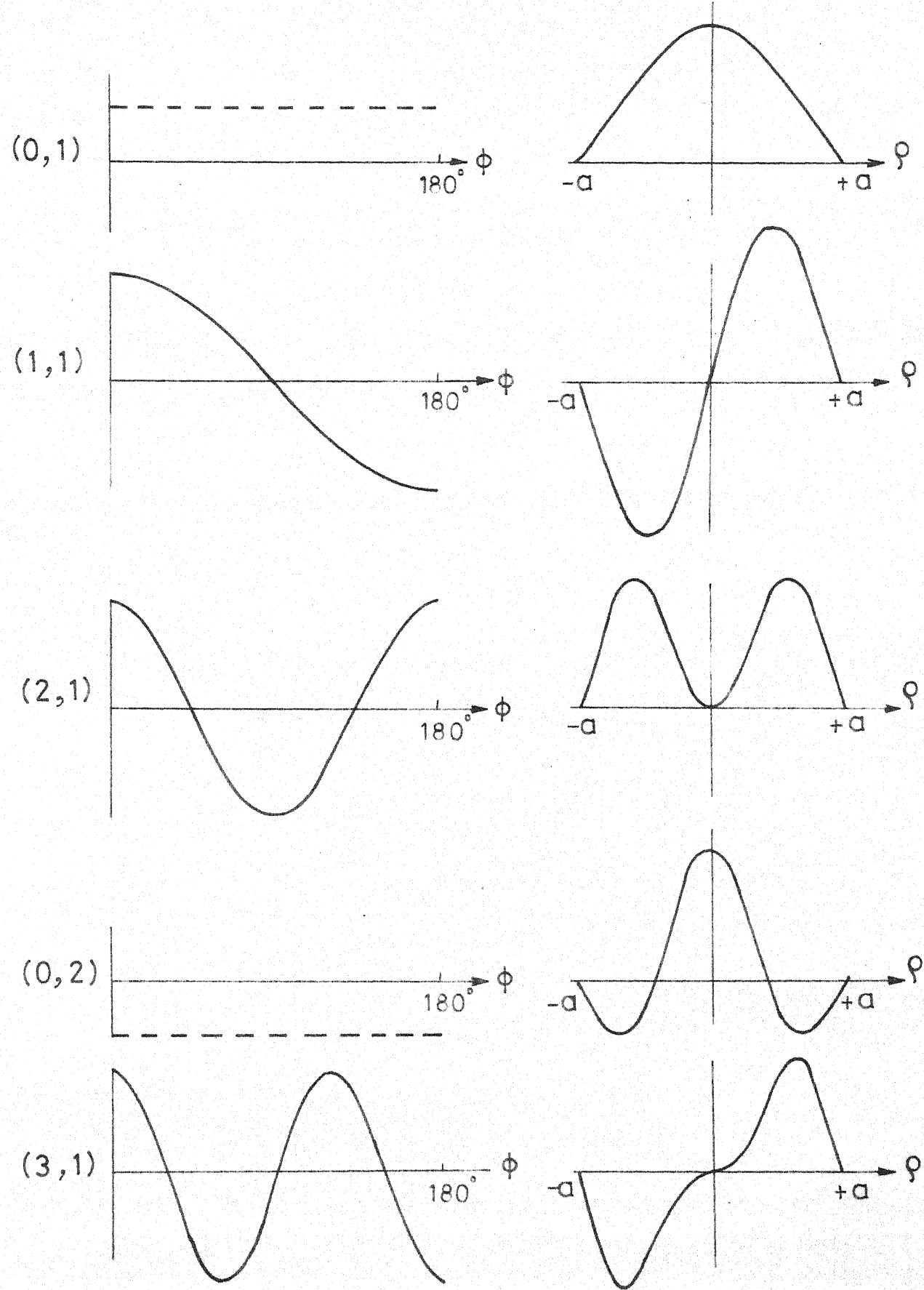(0,1) and other few modes is shown in Fig. 3.11. The voltage

(0,1)

(1,1)

(2,1)

(0,2)

(3,1)

Fig. 3·11   Voltage distribution for different resonant modes of semicircular microstrip antenna with circular periphery shorted

is maximum at the centre and zero at $\rho = a$. Hence, it is clear that, the 50 Ohms point is near the shorted circular pheriphery. The voltage distribution (for constant ρ) along φ is constant. Hence, the input impedance at any point along $\varphi = 0$ to $\varphi = \pi$ (for constant ρ) will not change. But, by selecting the feed-point along $\varphi = 90^{\circ}$, the effect due to odd-modes is avoided (because the modes $(1,n)$, $(3,n)$, $(5,n)$, ..., $n = 1,2,3,4$, ... are not excited. This is clear from (3.36)). The contribution due to the higher order modes will be less and hence only 20 even modes which are close to the fundamental mode are considered in the Green's function expression. The roots P'_{mn} are calculated using the formula given in Appendix A.

Three p-ports are taken along $\varphi = 90^{\circ}$. There are 14 ports along the straight edge of the antenna. The impedance matrix for this 17-port network model is calculated using (2.27). This gives $\underline{Z}_{pp}$, $\underline{Z}_{pq}$, $\underline{Z}_{qp}$ and $\underline{Z}_{qq}$, which are the unknowns in the input impedance equation (3.5). The other unknown, $\underline{Z}_{rr}$, is calculated from (3.37). Then, (3.5) is used to find the input impedances at the feed-ports. The parameters optimized to get the 50 Ohms point (where the VSWR = 1) are ρ_i (the distance from the centre to the feed-point along $\varphi = 90^{\circ}$) and the frequency.

The antenna is designed for a frequency of 3 GHz.
The radius calculated from (3.35) is 2.405 cms. The
50 Ohms feed-point is obtained at ρ_i = 1.955cms.

3.4.3 Input impedance

The input impedance and input VSWR at ρ_i = 1.955 are
calculated for different frequencies, above and below the
resonant frequency. These are shown in Figs. 3.12 and
3.13 respectively. The corresponding measured values are
also plotted in these figures. The discrepancy between the
theoretical and experimental input impedance loci shown in
Fig. 3.12 may be attributed to the reasons discussed in the
Section 3.2.3. The measured resonant frequency is 2932 MHz.
The difference between the theoretical and experimental
resonant frequencies may be due to the following reasons :
i) improper shorting of the circular periphery of the
antenna, and ii) because of the fringing fields along the
straight edge of the antenna, there will be some extension
of the physical boundary outwards and hence the antenna
configuration,as a whole, will not be a semicircle. The
accurate formulas are not available to find the extension.

3.4.4 Bandwidth

The theoretical and experimental bandwidths obtained
are 71.67 and 68.2 MHz respectively. One expects the
experimental bandwidth to be more than the theoretical
bandwidth because the conductor and dielectric losses are
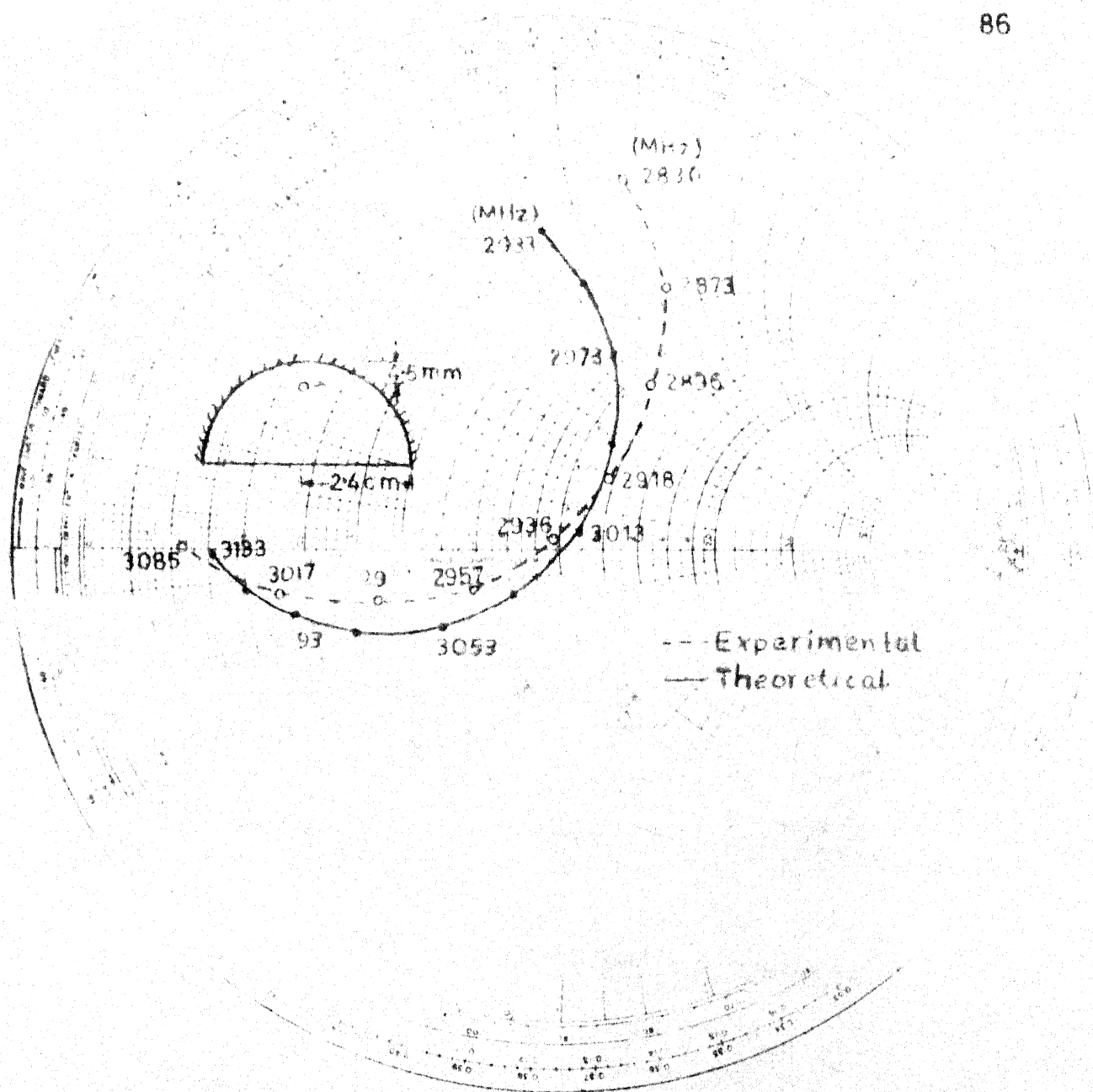
Fig. 3·12 Input impedance characteristic of semicircular microstrip antenna with circular periphery shorted

Substrate thickness = 1/8"
$\epsilon_r = 2.55$

4.5mm ─ ° Feed

├─ 2.4 cm ─┤

3.0 ─

- - - Theoretical
──── Experimental

2.6 ─

Input VSWR

2.2 ─

VSWR = 2 line

1.8 ─

Experimental band width
= 68.2 MHz

1.4 ─

Theoretical
band width
= 71.67 MHz

1.0 ─

0.985   0.99   0.995   1.0   1.005   1.01   1.015

Normalized frequency
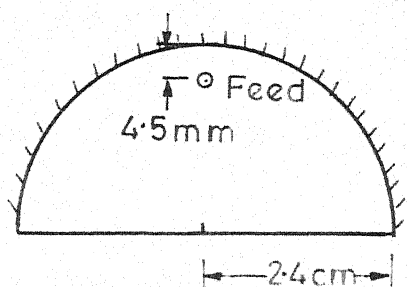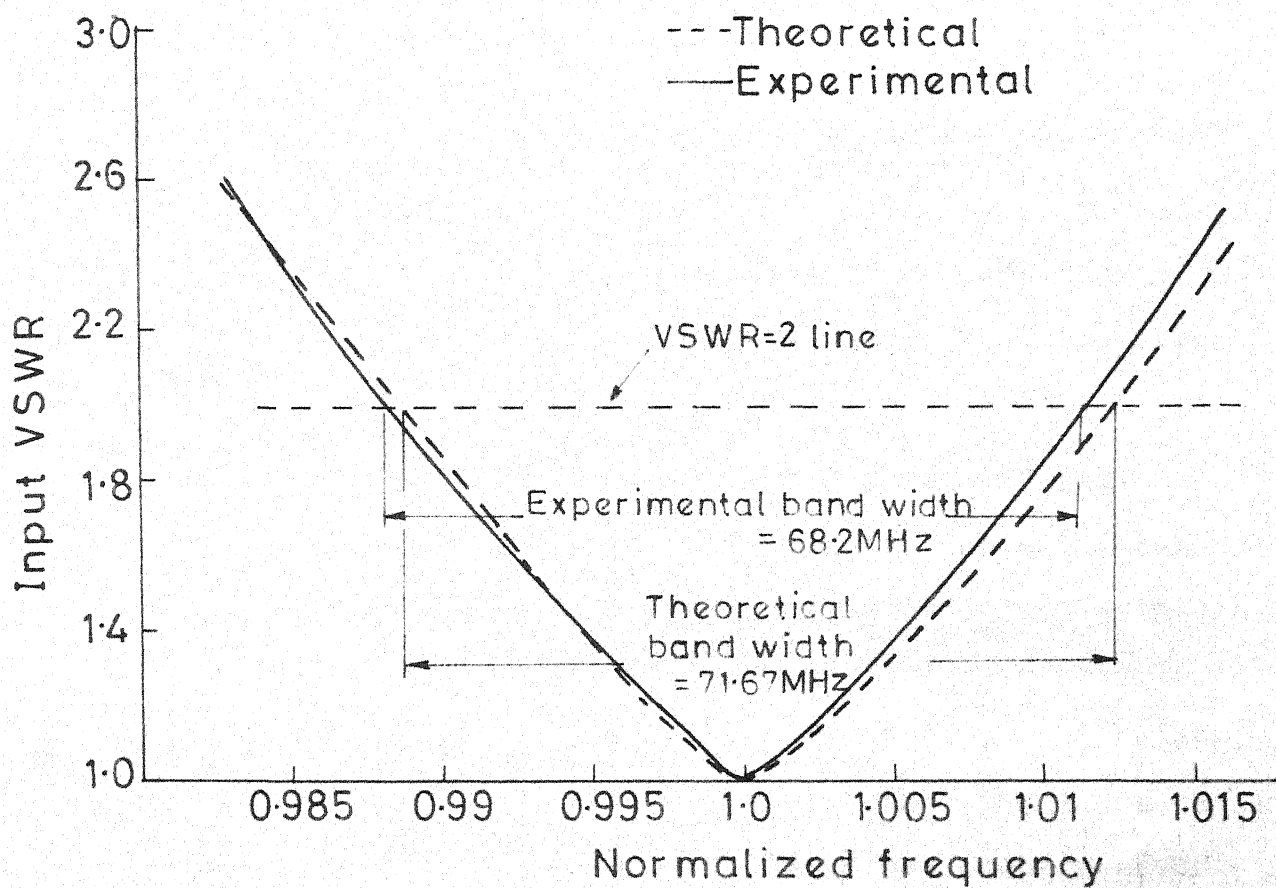
Theoretical resonant frequency = 3018 MHz
Measured resonant frequency = 2932 MHz

Fig. 3.13 Variation of input VSWR with frequen

ignored in the analysis. This shows that the radiation
resistance formula used for finding the radiation resistance
from the straight edge of the antenna is not very correct.
The experimental bandwidth is 2.2 percent (centre frequency =
2932 MHz). The bandwidth of the circular disk antenna
is 2.5 percent [11] (centre frequency = 3 GHz). This shows
that the radiation from the straight edge is more than
that of the circular edge.

3.4.5 Radiation pattern

The radiation patterns in $\varphi = 0^O$ and $\varphi = 90^O$ planes
are calculated using the procedure described in the
Sections 3.1.3 and 3.1.4. Only E_φ component is present in
$\varphi = 0^O$ plane, and only E_θ component is present in $\varphi = 90^O$
plane. These are plotted in Figs. 3.14(a) and (b) respecti-
vely. The 3-dB beamwidth in $\varphi = 0^O$ plane is 66°.

The measured radiation patterns in $\varphi = 0^O$ and $\varphi = 90^O$
planes are also plotted in Figs. 3.14(a) and (b) (dashed
lines) respectively. The experimental 3-dB beamwidths in
$\varphi = 0^O$ and $\varphi = 90^O$ planes are 62° and 98° respectively.
For E_θ component of the radiation field in $\varphi = 90^O$ plane,
the experimental values are much less than the theoretical
values for $\theta > 60^O$. Such discrepancy has been observed
by other investigat ors also [22]. This decrease in the
value of E_θ may be due to i) the excitation of surface waves,
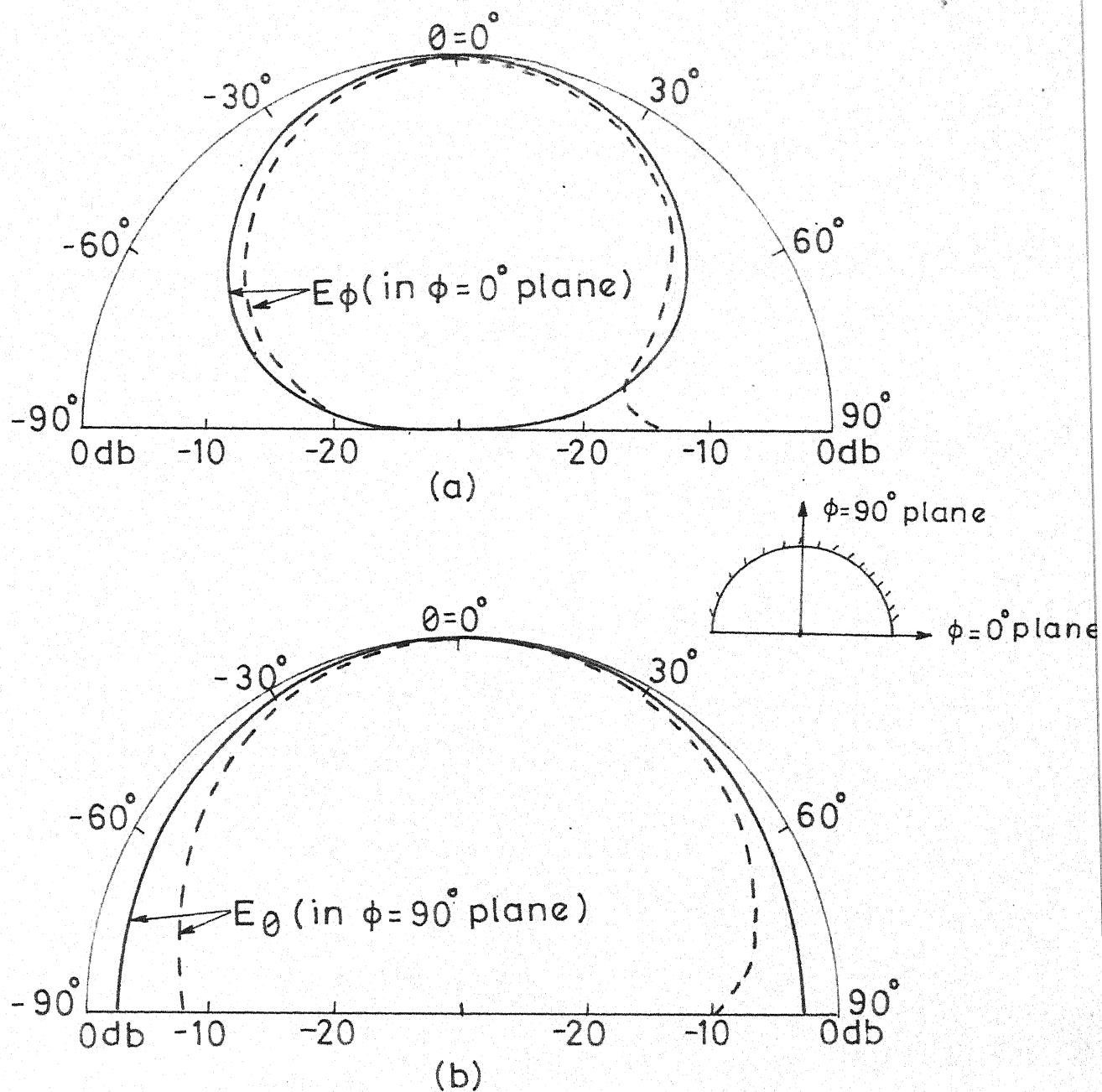which cause a flow of power along the substrate surface and

Fig. 3.14 Theoretical (———) and experimental (- - -)
radiation patterns of the antenna
shown in Fig. 3.10 (a)

(a) E_ϕ in $\phi = 0°$ plane

(b) E_θ in $\phi = 90°$ plane

ii) the presence of finite ground plane. The discrepancy between the theoretical and experimental radiation patterns of E_φ (in $\varphi = 0^\circ$ plane) near $\theta = 90^\circ$ may be also due to the reasons explained above.

3.5 120°-SECTORAL OPEN BOUNDARY MICROSTRIP ANTENNA

3.5.1 Theoretical considerations

The 120°-sectoral antenna shown in Fig. 3.15 (a) can be modelled as a cylindrical cavity, bounded on its top and bottom by electric walls and its straight edges and circular edge by magnetic walls. The Green's function for this configuration obtained from (2.66) is

$$G(\underline{r}/\underline{r_i}) = \frac{4j\omega\mu d}{\varphi_0} \sum_{m=o}^{\infty} \sum_{n=1}^{\infty} \frac{\sigma J_v(K_{vn}\rho_i) J_v(K_{vn}\rho) \cos(v\varphi_i)\cos(v\varphi)}{[(K_{vn}a)^2 - v^2][1 - \frac{K^2}{K_{vn}^2}] J_v^2(K_{vn} a)} +$$

$$- \frac{6d}{j\omega\epsilon\pi a^2} \tag{3.38}$$

where $\varphi_0 = 120^\circ$, $v = \frac{3}{2} m$ and $K_{vn} = \frac{p_{vn}}{a}$, p_{vn} is the nth root of the derivative of the Bessel function of the first kind and order v, and

$$\sigma = \begin{cases} 1, & \text{for } m = 0 \\ 2, & \text{for } m > 0 \end{cases} \tag{3.39}$$

The first term in (3.38) is due to the d.c. capacitance between the ground plane and the top conductor patch.
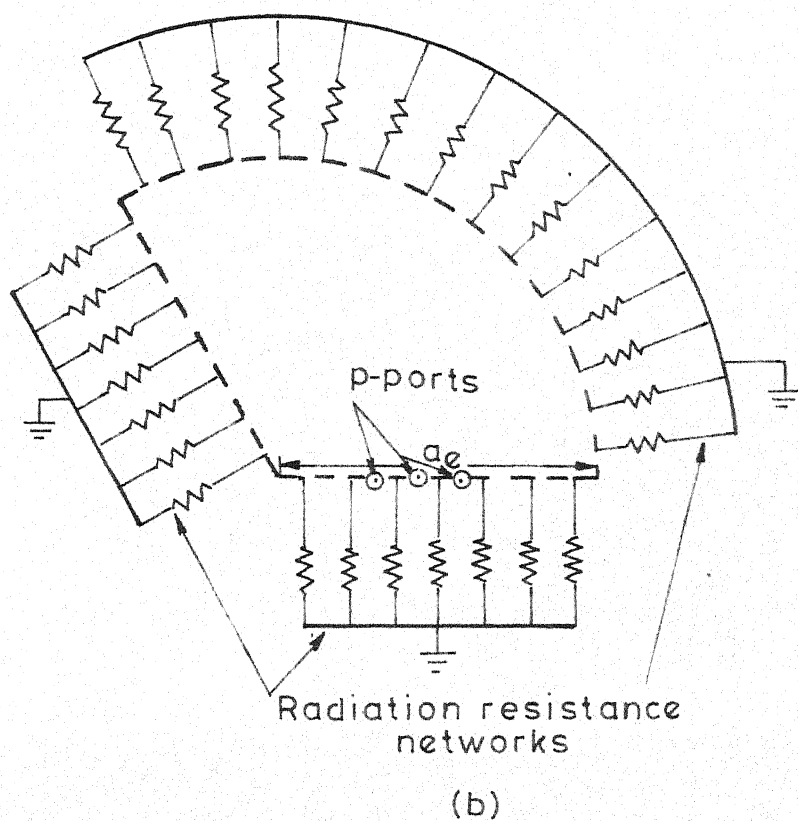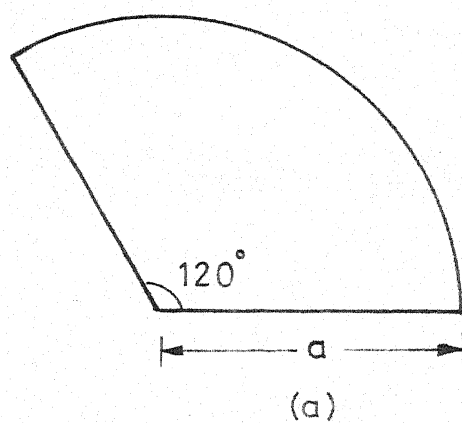
(a)

(b)

Fig. 3·15 (a) Open boundary 120°-sectoral antenna

(b) its equivalent multiport network

It is clear from above that for odd values of m, v is real i.e. the radial eigen functions are the Bessel functions of the first kind and real orders. The first few roots of

$$J_v(K_{vn} \; a) = 0 \qquad\qquad (3.40)$$

are given below.

n	v = 0	v = 3/2	v = 3	v = 9/2	v = 6
1	0	2.461	4.339	6.109	7.856
2	3.83164	6.029	8.017	9.914	11.759
3	7.0156	9.26	11.346	13.34	15.272
4	10.173	12.445	14.585	16.642	18.638

The smallest root is 2.461. The radius of the sector is the smallest for this root. Hence the mode (3/2,1) is called as the dominant mode. The Bessel functions $J_{3/2}$, $J_{5/2}$, $J_{7/2}$, $J_{9/2}$, ... can be calculated from the following formulas.

$$J_{\frac{1}{2}}(x) = \sqrt{\frac{2}{\pi x}} \; \sin x \qquad\qquad (3.41)$$

$$J_{-\frac{1}{2}}(x) = \sqrt{\frac{2}{\pi x}} \; \cos x \qquad\qquad (3.42)$$

$$\frac{2m}{x} J_m(x) = J_{m-1}(x) + J_{m+1}(x) \qquad\qquad (3.43)$$

From (2.27) and (3.38), the impedance matrix of the planar circuit shown in Fig. 3.15(a) (acting as resonator) follows as

i) for ports i,j on the circular periphery

$$Z_{ij} = \sum_{m=0,n=1}^{\infty}\sum^{\infty} \sigma \frac{2j\,\omega\mu d}{\varphi_0} \left[\frac{\sin(\frac{vW_i}{2a})}{(\frac{vW_i}{2a})} \cdot \frac{\sin(\frac{vW_j}{2a})}{(\frac{vW_j}{2a})}\right] \cdot$$

$$\frac{\cos(v\theta_i)\,\cos(v\theta_j)}{[(K_{vn}a)^2 - v^2)](1 - \frac{K^2}{K_{vn}^2})} + \frac{1}{j\,\omega\,C_0} \qquad (3.44)$$

The term inside the square bracket represents the effect of port width and can be approximated as 1 when $\frac{vW_i}{2a} \ll 1$ and $\frac{vW_j}{2a} \ll 1$ hold good. C_0 represents the electrostatic capacitance between the conductor patch and the ground plane.

ii) for ports i,j on the straight edge

$$Z_{ij} = \sum_{m=0}^{\infty}\sum_{n=1}^{\infty} \sigma \cdot \frac{2j\,\omega\mu d\,\cos(v\theta_i)\,\cos v(\theta_j)}{\varphi_0[(K_{vn}a)^2 - v^2][1 - \frac{K^2}{K_{vn}^2}]J_v^2(K_{vn}a)} \cdot$$

$$\frac{1}{W_i} \int_{R_i - \frac{W_i}{2}}^{R_i + \frac{W_i}{2}} J_v(K_{vn}\rho)d\rho \cdot$$

$$\frac{1}{W_j} \int_{R_j - \frac{W_j}{2}}^{R_j + \frac{W_j}{2}} J_v(K_{vn}\rho')d\rho' \qquad (3.45)$$

where R_i and R_j are the ρ -coordinates of the ports i and j.

iii) for ports i,j on the circular periphery and straight edge respectively.

$$Z_{ij} = \sum_{m=0}^{\infty} \sum_{n=1}^{\infty} \sigma \frac{2j\omega\mu d}{\varphi_o} \frac{\sin(v\frac{W_i}{2a})}{(\frac{v W_i}{2a})} \cos(v\theta_i) \cdot$$

$$\frac{1}{(a^2 K_{vn}^2 - v^2)(1 - \frac{K^2}{K_{vn}^2}) J_v(K_{vn}a)} \frac{1}{W_j} \int_{R_j - \frac{W_j}{2}}^{R_j + \frac{W_j}{2}} J_v(K_{vn}\rho') d\rho'$$

$$+ \frac{1}{j\omega C_o} \tag{3.46}$$

3.5.2 Optimization of feed-point

The Green's function method discussed in the Section 3.1 is used for analysis. 14 ports are taken along the circular periphery and 7 ports are taken on each of the two straight edges. The radiation resistances of the straight edges are calculated using the formulas of rectangular patch antennas. Since the formula for finding the radiation resistance of the circular edge of the 120°-sector antenna is not available, a trial value of 1200 Ohms (which is approximately 3 times the radiation resistance of the open boundary circular antenna) is taken. By doing experimental iterations, the exact 50 Ohms feed-point is found.

The voltage distribution for the dominant mode and other few modes is shown in the Fig. 3.16. The voltage is zero at
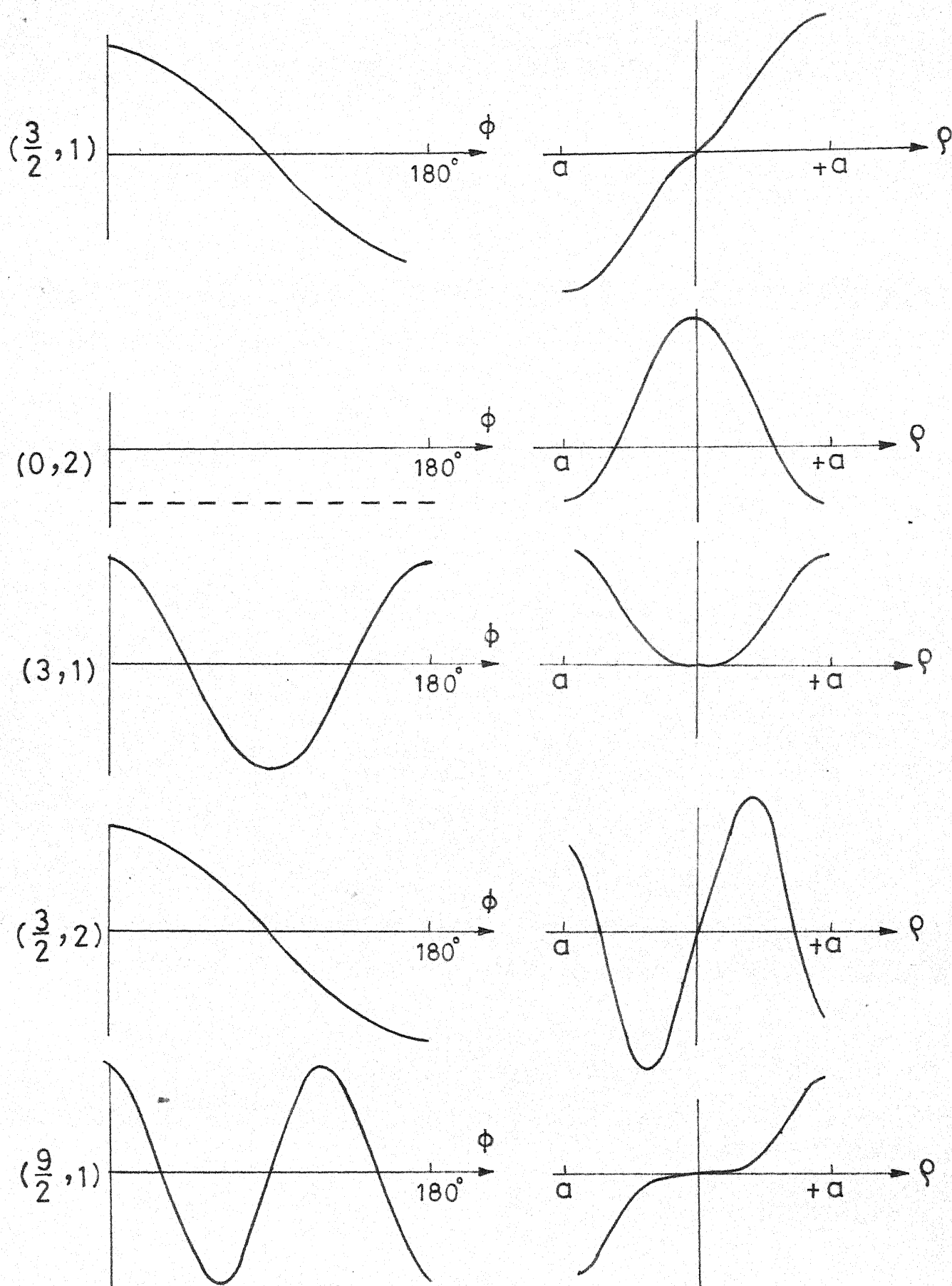
$(\frac{3}{2},1)$

$(0,2)$

$(3,1)$

$(\frac{3}{2},2)$

$(\frac{9}{2},1)$

Fig.3·16 Voltage distribution for different
resonant modes of 120°-sector microstrip

the centre and maximum at $\rho = a$. For the resonant mode considered, the feed-point cannot be taken along ($\varphi = 60^o$) the centre line of the sector (This is clear from (3.38)). The feed-point is taken along $\varphi = 0^o$. 3 p-ports are taken along this axis for optimization of the 50 Ohms feed-point The input impedances at these ports are calculated using (3.5), (3.44) - (3.46).

The resonant frequency (for the dominant mode) for effective radius 'a_e' equal to 2.348 cms, calculated from (3.35) is 3.133 GHz. The actual radius of the sector obtained from (3.27) is 2.19 cms. The feed-point obtained is at a distance of 0.7 cms from the centre. The measured frequency is 3.181 GHz, which is 48 MHz more than the theoretical value. This may be due to the following reasons : i) The formulas used to find the extension on the straight edges are the extension formulas for the straight edges of a rectangle. These may not predict the extensions accurately, because the geometry of the planar element is different, ii) The formula for finding the extension in case of circular planar elements is used to find the extension on the circular periphery. This formula may not hold good accurately for a sector.

3.5.3 Bandwidth and input impedance

The variation of VSWR with frequency (experimental) is shown in Fig. 3.17. The bandwidth obtained is 115 MHz, which is 3.6 percent of the centre frequency [3181 MHz]. The input impedance locus is shown in   Fig. 3.18. This curve is not passing through the 50 ohms point and it is shifted slightly towards right side of the Smith chart. Therefore, the correct bandwidth is slightly less than 115 MHz.

The bandwidth of a circular antenna at the above centre frequency given in [11] is approximately 3 percent. This shows that the bandwidth of 120°-sectoral antenna is slightly more than that of a circular antenna.
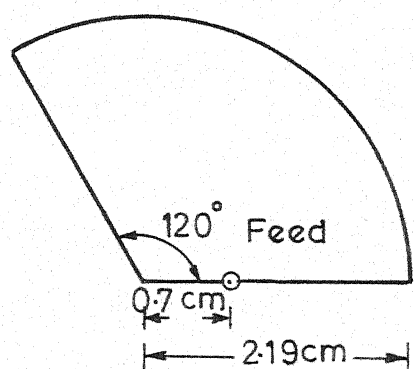
3.5.4 Radiation pattern

The measured values of E_{θ} and E_{φ} in $\varphi = 0^{o}$ and 90° planes are plotted in Figs. 3.19 and 3.20. It is noted that both E_{θ} and E_{φ} components are present in each plane.

3.6   EXPERIMENTAL STUDY OF MUTUAL COUPLING IN TWO-ELEMENT ARRAYS

3.6.1 Introduction

Microstrip antenna arrays have found wide applications in recent years. The main advantages are : relative ease of construction, light weight, low cost, and either conformability to the mounting surface or, at least, on extremely thin

$\epsilon_r = 2.55$

Substrate thickness $= 1/8''$
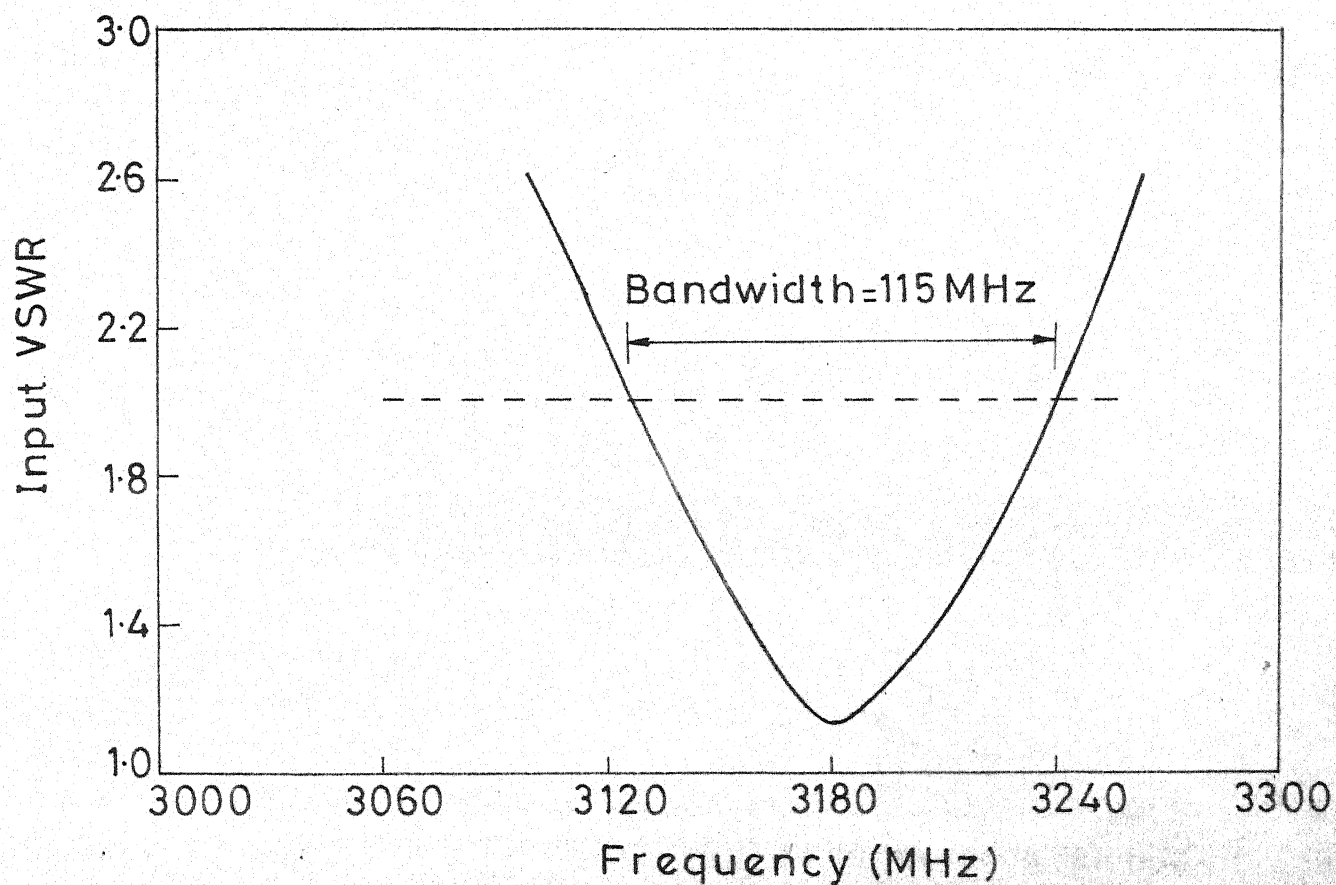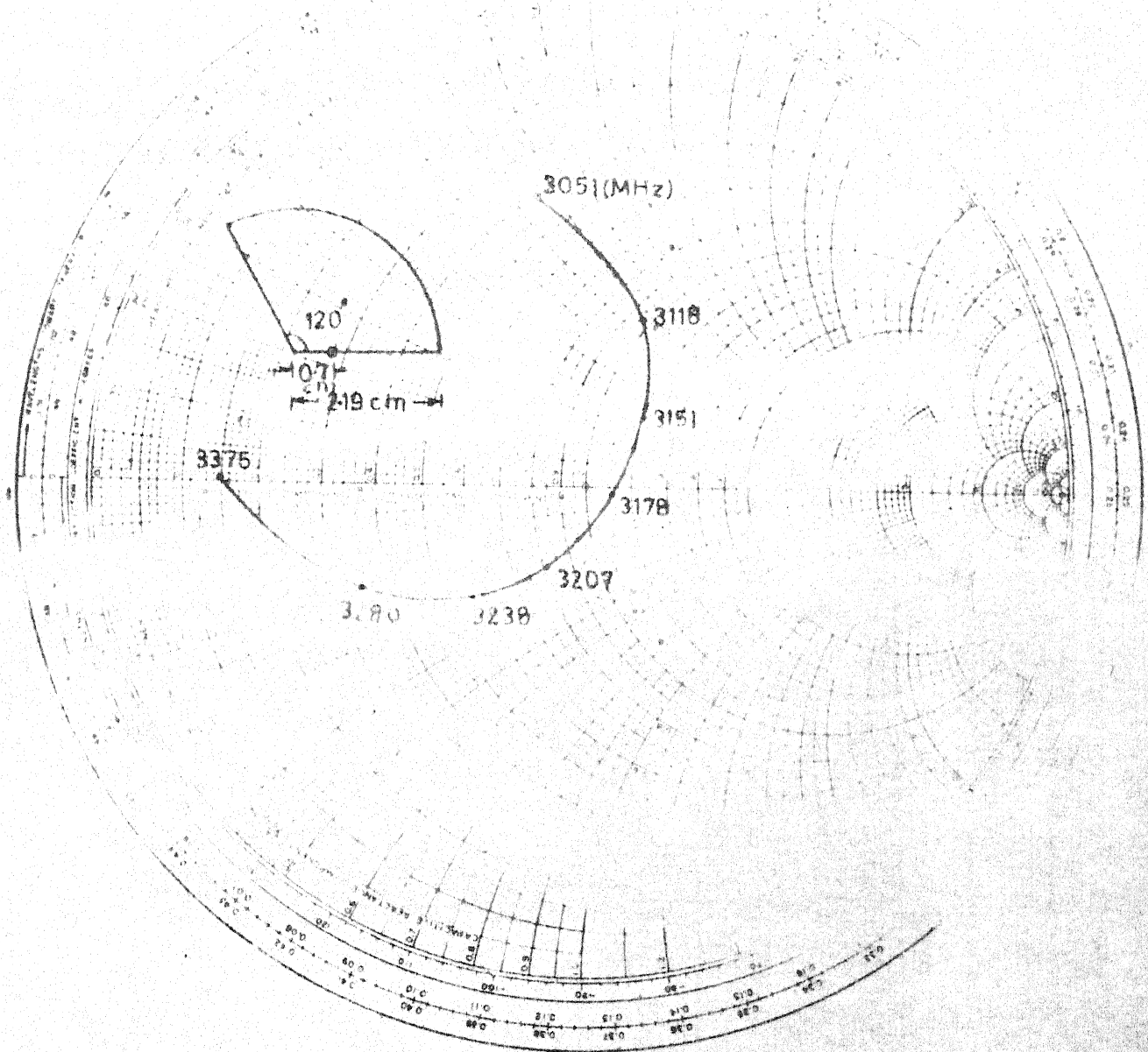
Fig.3.17 Variation of input VSWR with frequency

Fig. 3·18 Experimental input impedance locus for open
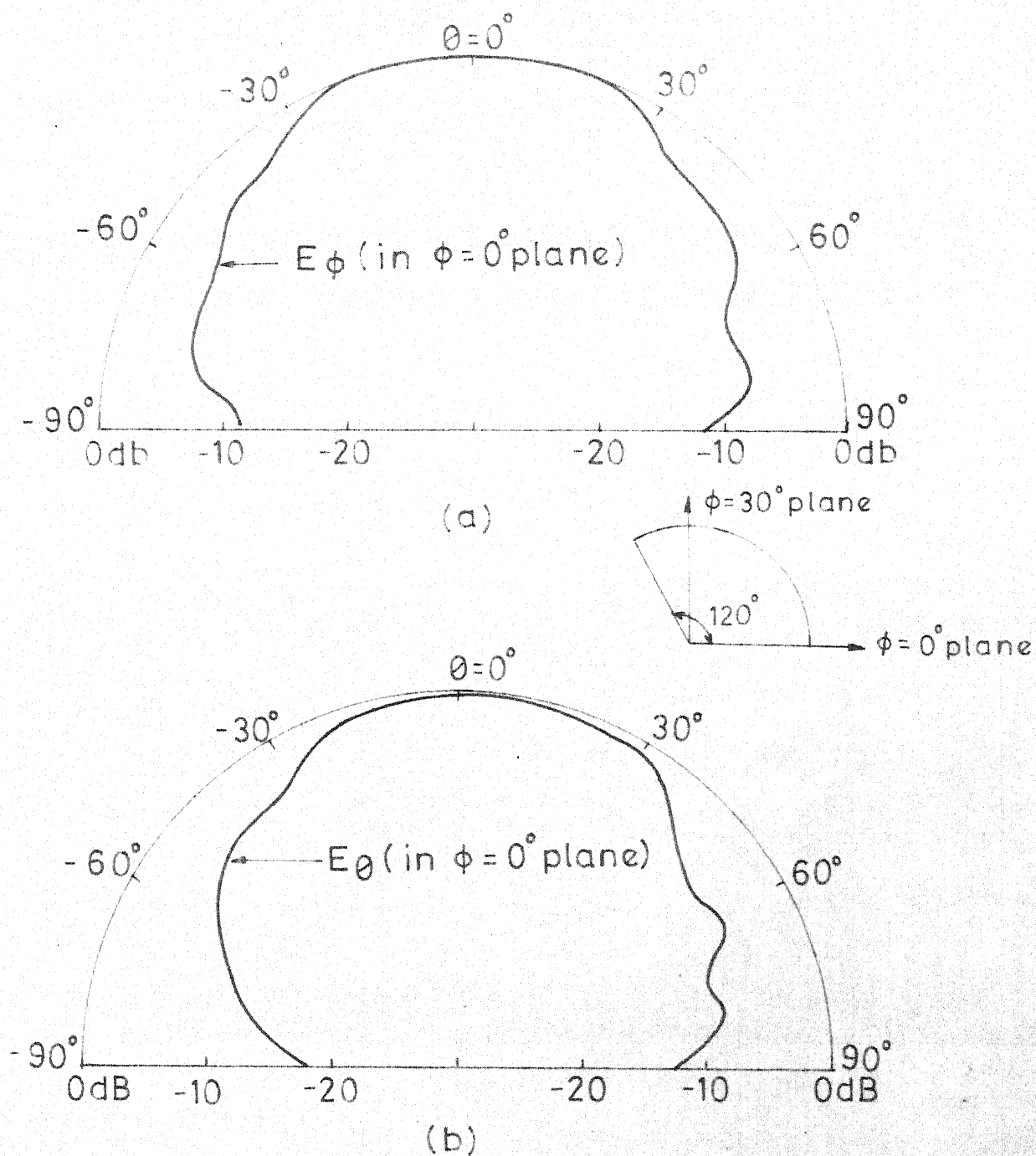boundary 120°-sectoral microstrip antenna

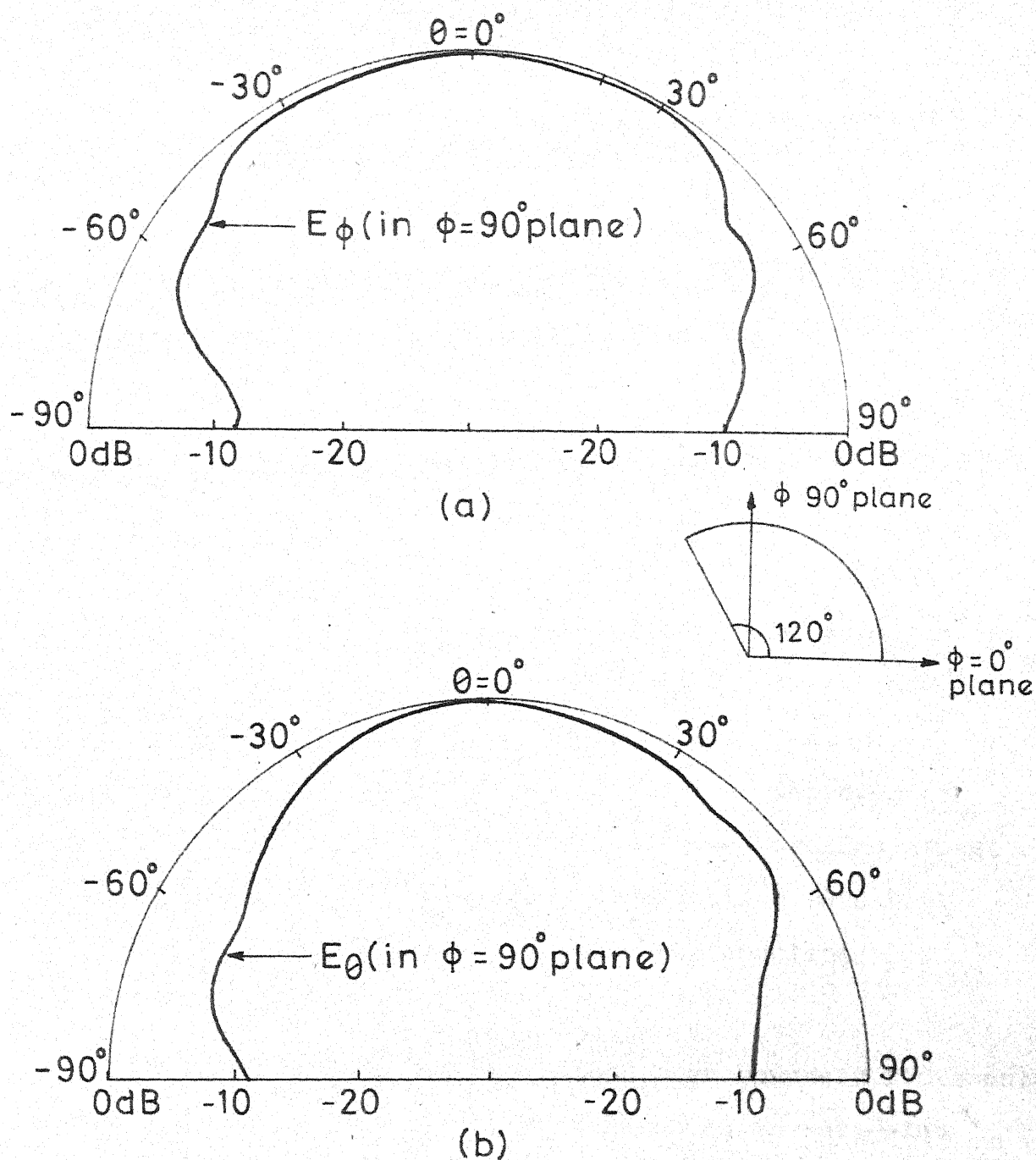Fig.3·19 Experimental radiation patterns of 120°-sectoral antenna in φ=0° plane (a) Eφ (b)Eθ

Fig. 3·20 Experimental radiation patterns of 120°-sectoral antenna in φ=90° plane (a) Eφ (b) Eθ

protrusion   from the surface. High gain and desired
patterns can be obtained using these arrays. They are
limited in that they tend to radiate efficiently only
over a narrow band of frequencies and they cannot operate
at high power levels of waveguide, coaxial line, or
even strip line.

When a well matched individual element is placed in
an array environment, its terminal properties will change
as a result of mutual coupling effects. These coupling
effects may produce increased side lobe levels,main beam
squint, filled or shifted nulls, granting lobes and array
blindness at some scan angles. However, it is also
possible for mutual coupling to produce an improvement
in side lobe levels for those cases where coupling causes
a further tapering of the array distribution function.
Therefore, it is necessary to study the coupling
between the   elements of an array.

Mutual coupling between L-band open boundary rectangular
and circular microstrip antennas has been investigated
experimentally by a series of measurements of the S-
parameters [20],[23]. Typical values of $|S_{12}|^2$ obtained
are -15 dB to -50 dB for spacing in the range of 0.1 λ to
1.75 λ (thickness of the substrate = 0.1575 cms). The
mutual coupling level decreases monotonically with
increasing separation between elements for both rectangular

and circular microstrip antennas. For rectangular
microstrip antennas, E-plane coupling [radiating
edges coupled] is more than that of the H-plane (non-
radiating edges coupled) coupling for all spacings. For
circular microstrip antennas, upto a spacing of approximately
$0.25\ \lambda$, H-plane coupling is more than that of the E-plane
coupling, while for spacing more than $0.25\ \lambda$, E-plane
coupling is more than that of H-plane coupling. Mutual
coupling depends upon the spacing between the elements,
lengths of the radiating edges and thickness of the sub-
strate. Since the total length of the radiating edges
is less in a mixed boundary antenna, the coupling between
two mixed boundary antennas is expected to be less than
the coupling between two open boundary antennas.

3.6.2 Mutual coupling between two open boundary and two mixed boundary semicircular antennas

3.6.2.1 Experimental technique

The mutual coupling levels (S_{12} or S_{21}) are measured
with a network analyzer system for two two-element arrays
of semicircular antennas (with circular peripheries shorted)
shown in Fig. 3.21(a) and open boundary semicircular antennas
shown in Fig. 3.21(b). The isolated elements are designed
to operate with an approximate 50 Ohms driving point impe-
dance. The S_{ij} ($i \neq j$) are measured as the transmission
coefficients between the ports when a 50 Ohms source is
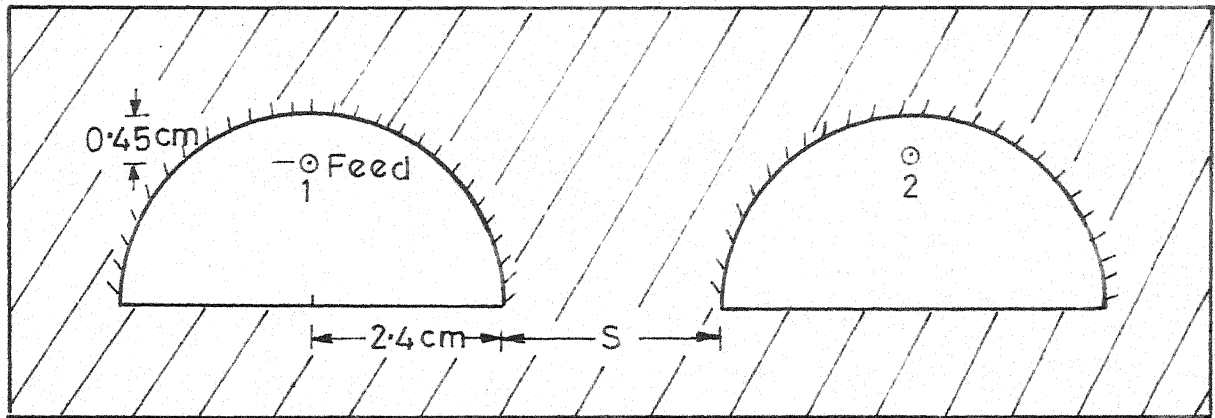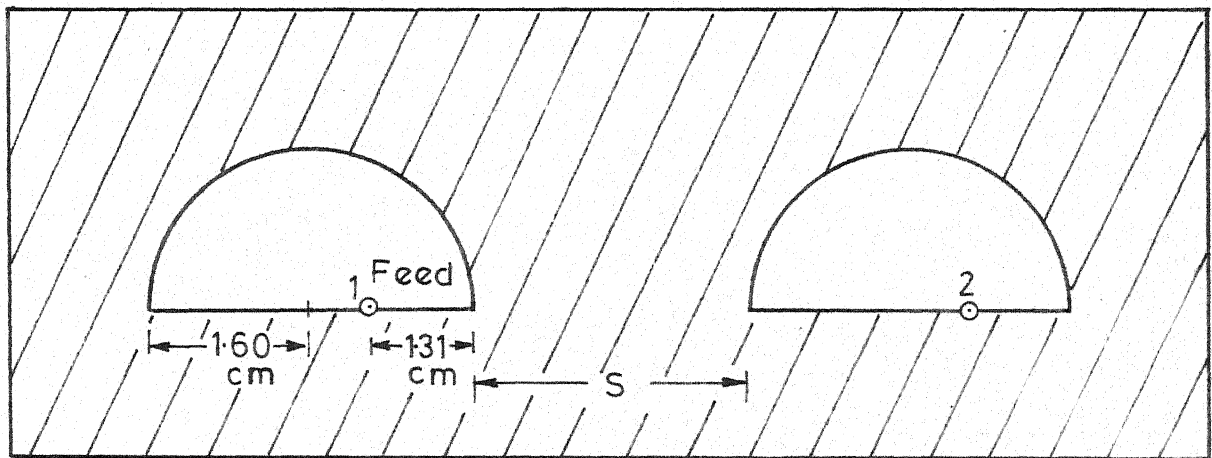
Fig. 3·21 Coupling measurement configurations

    (a) for semicircular antennas with circular
        peripheries shorted

    (b) for open boundary semicircular antennas

connected at the jth port and a 50 ohms detector is
connected at the ith port. The S_{ii} are measured as the
reflection coefficients seen at the ith port with jth
port terminated in a 50 Ohms load. Because the input
impedance of both the antenna elements is same, S_{ii} is
equal to S_{jj} and S_{ij} is equal to S_{ji}.

3.6.2.2 Results

The antennas are fabricated on copper cladded 1/8"
thick polysterene substrate of ε_r equal to 2.55. The
results of the measurements of $|S_{12}|^2$ for spacing S equal
to 0.31 λ_o and 0.44 λ_o (f_o = 2950 MHz for semicircular
antenna with circular periphery shorted and f_o is equal
to 3159 MHz for open boundary semicircular antenna) are
given in Table III.

Table III

Spacing S	Coupling (in dB)	
	Semicircular antenna with circular periphery shorted	Open boundary semicircular antenna
0.31 λ_o	−25.3	−20.4
0.44 λ_o	−28.5	−25.0

It is seen that the coupling between two mixed boundary semicircular antennas is 4.9 dB and 3 dB down (for the spacings considered) than that of open boundary antennas.

The input impedance locus for the element 1 (or S_{11}) of the array (for $S = 0.31 \lambda_o$) configuration shown in Fig. 3.21(a) is given in Fig. 3.22(a). The input impedance locus for the element 1 when it is not coupled to the 2nd element is shown in Fig. 3.22(b). It is noted that, due to coupling, the impedance locus is shifted towards the right side of the Smith chart. The corresponding impedance loci when the elements of the array are open boundary semi-circular antennas are given in Figs. 3.23(a) and (b). It is seen that, the impedance locus is shifted towards the left side of the Smith chart due to coupling.

The discussions of the antennas presented in this chapter are given in the next chapter.
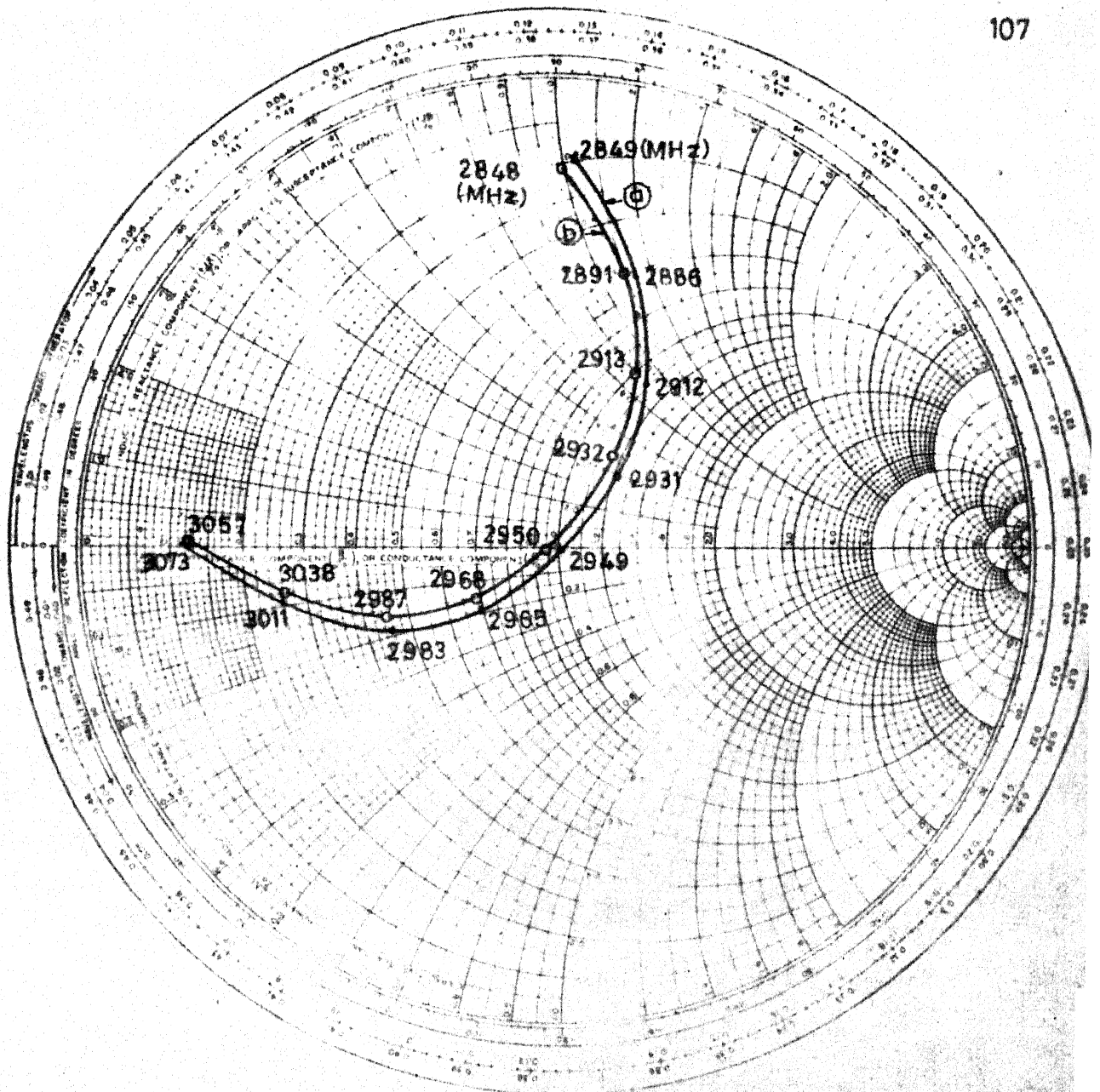
Fig. 322 (a) S_{11} for coupled (S = 3.15 cm or $0.31\lambda_0$, f = 2.950 GHz)
semicircular microstrip antennas (with circular
peripheries shorted) shown in Fig. 321(a), (b) input
impedance locus for an individual semicircular
microstrip antenna with circular periphery
shorted

Fig. 3·23 (a) S_{22} for coupled (S = 2·9 cm or 0·306λ_0, f_d3·15·9 GHz)
Open boundary semicircular microstrip antennas
shown in Fig.3·21(b),(b) input impedance locus for
an individual open boundary semicircular
microstrip antenna

CHAPTER FOUR

CONCLUDING REMARKS

This chapter contains a summary of the results reported in this thesis and suggestions for further investigations.

4.1 SALIENT RESULTS

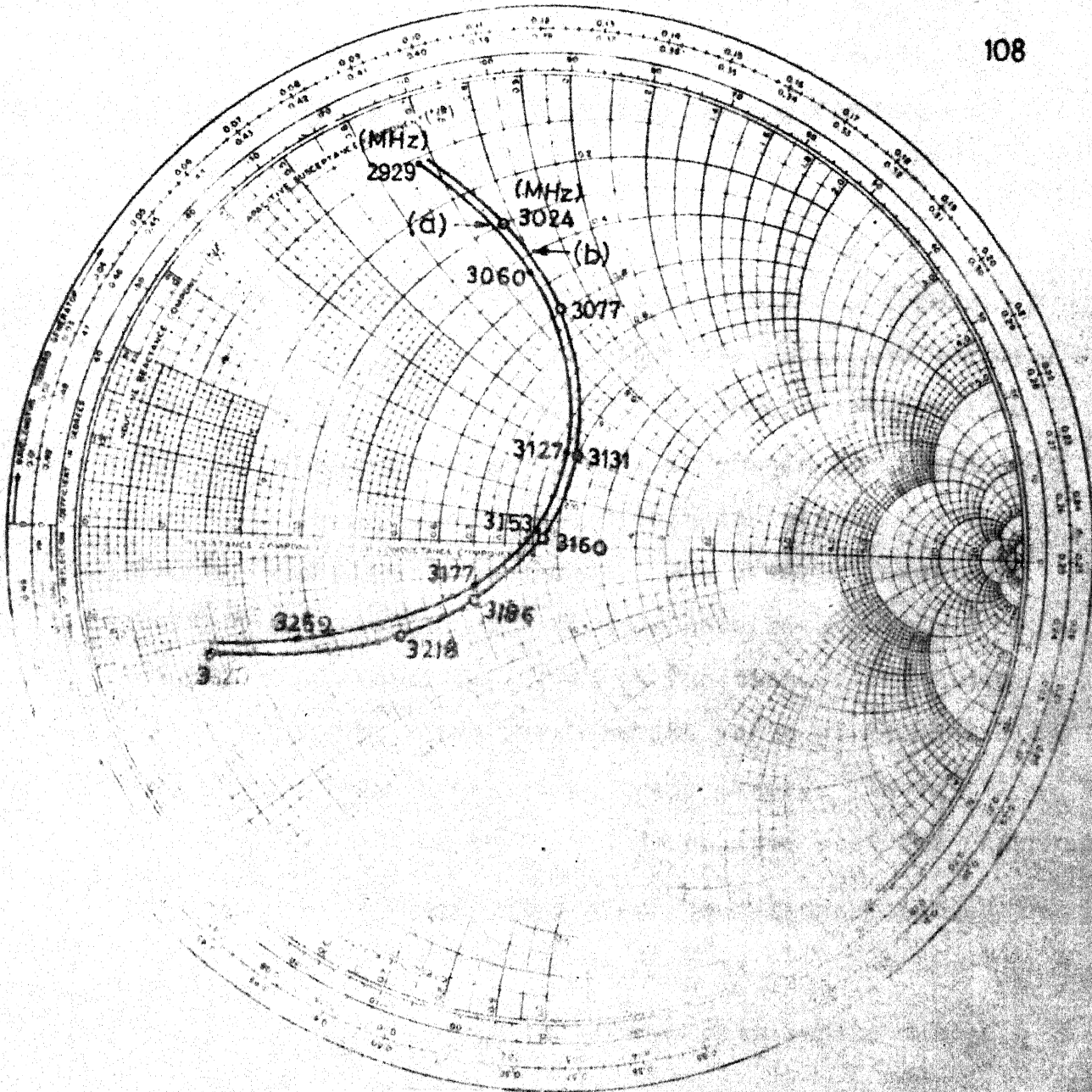In this thesis Green's functions for all possible mixed boundary 30°-60° right-angled triangular and sectoral segments have been developed. For triangular shapes, the method of images has been employed to obtain the eigenfunctions of the Helmholtz equation which are then used to derive the Green's functions. The Green's functions for mixed boundary circular sectors have been obtained by expanding these in series of eigen functions. The eigen values K'^2_{vn} and K^2_{vn} are given by the zeros of the Bessel's functions and their derivatives respectively. These Green's functions have been used to analyze sectoral antennas.

Various microstrip antenna configurations reported in this thesis are :

i)   semicircular microstrip antenna with straight edge shorted,

ii) open boundary semicircular antenna,

iii) semicircular antenna with circular periphery shorted

iv) open boundary 120°-sectoral antenna.

The above antennas have been analyzed using Green's function approach.

i)   Semicircular antenna with straight edge shorted

The bandwidth obtained is 0.5 percent (centre frequency = 1 GHz) . The 3-dB beamwidths (experimental) obtained in $\varphi = 0^O$ and 90° planes are 110° and 135° respectively. These beamwidths are more as compared to the beamwidths of a circular antenna (80° and 100° respectively). The physical area is one-half of that of the circular antenna.

ii) Open boundary semicircular antenna

This antenna has been studied experimentally. The bandwidth obtained is 3.13 percent (centre frequency = 3159 MHz), which is more than that of the open boundary circular antenna (2.5 percent). The physical area is 4.02 cm^2.

iii) Semicircular antenna with circular periphery shorted

In this case, the bandwidth obtained is 2.2 percent (centre frequency = 2932 MHz). The physical area is 9.047 cm^2. The beamwidths obtained in $\varphi = 0^O$ and 90° planes are 62° and 98° respectively.

iv) Open boundary 120°-sectoral antenna

The bandwidth and radiation characteristics are studied experimentally. The bandwidth obtained is 3.6 percent. The physical area is 5.02 cm^2.

The mutual coupling in two-element arrays of open boundary semicircular antennas and semicircular antennas with circular peripheries shorted has been studied experimentally. The coupling levels obtained in case of mixed boundary semicircular antennas are less as compared to that of open boundary semicircular antennas.

4.2 SUGGESTIONS FOR FURTHER WORK

The shorted boundary equilateral triangular and shorted boundary sectoral segments (whose Green's functions are derived in this thesis) can be used as high-Q resonators (since the radiated power is zero, Q-factor is very high).

The mixed boundary **semi-circular antennas can** be used in arrays to reduce mutual coupling.

Since it is found that the straight edges radiate more than that of circular edges, the open boundary sectoral antennas with sectoral angles less than 120° can be studied. The physical areas of these antennas will be less as compared to open boundary semicircular and circular antennas. Also, the number of higher-order modes that get excited will be less. For example, in case of 30°-sectoral antenna, the physical area is 2.8 cm^2 (for the dominant mode $(0,2)$) and the modes that get excited for a feed-point along $\varphi = 15^{\circ}$ will be (o,n), $(12,n)$, $(24,n)$ ... The computation time for analyzing these antennas using Green's function approach will be less because of less number of modes.

APPENDIX A

FORMULAS FOR CALCULATION OF THE ZEROS OF BESSEL FUNCTIONS

The formulas for evaluating the roots of Bessel functions and roots of derivative of Bessel functions [25] are given in this Appendix.

The sth root, in order of magnitude, of the equation

$$J_n(x) = 0$$

is

$$x_n^{(s)} = r - \frac{m-1}{8r} - \frac{4(m-1)(7m-31)}{3(8r)^3} - \frac{32(m-1)(83m^2-982m+3779)}{15(8r)^5}$$

$$- \frac{64(m-1)(6949m^3-153855m^2+1585743m-6277237)}{105(8r)^7} - \cdots,$$

where

$$r = \frac{1}{4}\pi(2n+4s-1), \quad m = 4n^2$$

The sth root, in order of magnitude, of the equation

$$J_n'(x) = 0$$

is

$$x_n^{(s)} = t - \frac{m+3}{8t} - \frac{4(7m^2+82m-9)}{3(8t)^3} - \frac{32(83m^3+2075m^2-3039m+3537}{15(8t)^3} -$$

where $t = \frac{1}{4}\pi(2n+4s+1)$, $m = 4n^2$

REFERENCES

[1]   T. Okoshi and T. Miyoshi, 'The planar circuit - An approach to microwave integrated circuitry', IEEE Trans. Microwave Theory Tech., vol. MTT-20, pp 245-252, Apr. 1972.

[2]   T. Okoshi and T. Takeuchi, 'Analysis of planar circuits by segmentation method', Electron. Commun. Japan, vol. 58-B, No.8, pp. 71-79, Aug. 1975.

[3]   T. Okoshi, Y. Uehara and T. Takeuchi, 'The segmentation method - An approach to the analysis of microwave circuits', IEEE Trans. Microwave Theory Tech., vol. MTT-24, pp. 662-668, Oct. 1976.

[4]   T. Okoshi, T. Takeuchi, and J.P. Hsu, 'Planar 3-dB hybrid circuit', Electron Commun. Japan, vol. 58-B, No.8, pp 80-90, Aug. 1975.

[5]   R. Chadha and K.C. Gupta, 'Green's functions for triangular segments in planar microwave circuits', IEEE Trans. Microwave Theory Tech., vol. MTT-28, pp. 1139-1143, Oct. 1980.

[6]   R. Chadha and K.C. Gupta, 'Green's functions for circular sectors, annular rings and annular sectors in planar microwave circuits', IEEE Trans. Microwave Theory Tech., vol. MTT-29, pp 68-71, Jan. 1981.

[7]   P. Silvester, 'Finite element analysis of planar microwave networks', IEEE Trans. Microwave Theory Tech., vol. MTT-21, pp. 104-108, Feb. 1973.

[8]   J. Helszajn and D.S. James, 'Planar triangular resonators with magnetic walls', IEEE Trans. Microwave Theory Tech. vol. MTT-26, pp. 95-100, Feb. 1978.

[9]   J. Helszajn, D.S. James, and W.T. Nisbet, 'Circulators using planar triangular resonators', IEEE Trans. Microwave Theory Tech., vol. MTT-27, pp. 188-193, Feb. 1979.

[10]   K.C. Gupta, R. Garg, and I.J. Bahl, Microstrip Lines and Slotlines, Dedham, MA: Artech House, 1979.

[11]   I.J. Bahl and P. Bhartia, Microstrip antennas, Dedham, MA: Artech House, 1981.

[12] K.R. Carver and J.W. Mink, 'Microstrip antenna technology', IEEE Trans. Antennas Propagat., vol. AP-29, pp 2-24, Jan. 1981.

[13] Y.T. Lo, D. Soloman and W.F. Richards, 'Theory and experiment on microstrip antennas', IEEE Trans. Antennas Propagat., vol.AP-27, pp 137-145, March 1979.

[14] K.R. Carver, 'A modal expansion theory for the microstrip antenna', IEEE AP-S Int. Symp. Digest, pp 101-104, June 1979.

[15] T. Okoshi and T. Miyoshi, 'The planar circuit - an approach to microwave integrated circuitry', IEEE Trans. Microwave Theory Tech., vol. MTT-20, pp 245-252, April 1972.

[16] K.C. Gupta and P.C. Sharma, 'Segmentation and desegmentation techniques for analysis of planar microstrip antennas', IEEE AP-S Int. Symp. Digest, pp 19-22, June 1981.

[17] K.R. Carver and E.L. Coffey, 'Theoretical investigation of the microstrip antenna', New Mexico State Univ., Tech. Rep. PT-00929, Jan. 1979.

[18] J.H. Richmand, 'A wire-grid model for scattering by conducting bodies', IEEE Trans. Antennas Propagat., vol. AP-14, pp 782-786, Nov. 1966.

[19] E.L. Newmann, 'Strip antenna in dielectric slab', ibid., vol. AP-26, pp 647-653, Sept. 1978.

[20] Proc. Workshop on Printed Circuit Antenna Technology, New Mexico State Univ., Oct. 1979.

[21] Y.T. Lo et al., 'Study of microstrip antennas, microstrip phased arrays, and microstrip feed networks', Tech. Rep. RADC-TR-77-406, Univ. of Illinois, Urbana, Oct. 1977.

[22] P.C. Sharma, 'Desegmentation method and its applications to circularly polarized microstrip antennas', Ph.D. Thesis, Department of Electrical Engineering, Indian Institute of Technology, Kanpur, India, April 1982.

[23] R.P. Jedlicka, M.T. Poe, zand K.R. Carver, 'Measured Mutual Coupling Between Microstrip Antennas', IEEE Trans. Antennas and Propagat., vol. AP-29, No.1, pp. 147-149, Jan. 1981.

[24] H. Pues and A. Van de Capelle,'A simple accurate
     formula for the radiation conductance of a rectangular
     microstrip antenna', IEEE AP-S Int. Symp. Digest,
     pp. 23-26, June 1981.

[25] A. Gray and G.B. Mathews, 'A treatise on Bessel
     functions and their application to physics', Dover
     Publications, Inc. New York, 1966.